



DIPLOMARBEIT

Crystal restructuring by nano-scale melting

ausgeführt am

Institut für Theoretische Physik
der Technischen Universität Wien

Institute for Theoretical Physics
Vienna University of Technology

unter der Anleitung von

Associate Prof. Dipl.-Ing. Dr.techn. Christoph Lemell &
O.Univ.-Prof. Dipl.-Phys. Dr.rer.nat. Joachim Burgdörfer

durch

Georg Wachter

Obere Bahngasse 20 / 6, A-1030 Wien

georgwachter@gmail.com

Datum

Unterschrift

Contents

Abstract	9
List of symbols	12
1 Introduction	13
2 A microscopic model for track creation	19
2.1 Overview: analysis of time scales	19
Energy deposition to the target.	20
Electron cascade and energy transfer to the lattice. . .	20
Energy diffusion in the lattice and restructuring. . . .	20
Conclusion	20
2.2 Energy deposition to the target	22
2.2.1 Mechanisms of energy transfer	22
Electron capture and loss	23
Target excitation and ionization	25
2.2.2 Target ionization	27
2.2.2.1 Simplifying the system to a 3-body-problem	27
Equilibrium charge state of the projectile	27

Independent ionizations	27
Independent electrons: single active electron	28
Continuum	30
2.2.2.2 Time-dependent perturbation theory	30
2.2.2.3 CDW-EIS: Continuum distorted wave - eikonal ini- tial state	31
Effective target charge Z_t	34
Implementation	34
Validity	34
2.2.3 Results	35
2.2.3.1 Validity of the approximation - calculating the stop- ping power	35
2.2.3.2 Discussion of singly differential cross sections	38
2.2.3.3 Summary	39
2.3 Energy diffusion in the electronic system & energy transfer to the lattice	41
2.3.1 Introduction	41
2.3.2 Electron transport	44
2.3.2.1 Initial conditions	45
Initial position	45
Initial momentum	45
2.3.2.2 Energy diffusion in the electronic system	45
Elastic collisions	46
Inelastic collisions	46

2.3.2.3	Analysis of mean free paths; energy diffusion to the lattice	48
	Estimate of N_{phonon}	51
2.3.3	Results	53
2.3.3.1	Effect of N_{phonon} on energy distribution	54
	Bounds for track diameters based on energy density distributions	55
2.3.3.2	Dependence of energy distributions on the initial electron energy	56
2.3.3.3	Ion energy dependent radial energy distributions	58
	Impact parameter dependence of the ionization process	59
2.3.4	Conclusion	61
2.4	Energy diffusion in the lattice and restructuring	62
2.4.1	Overview of Molecular Dynamics (MD)	64
2.4.1.1	Choice of physical forces	65
2.4.1.2	Thermostat	67
2.4.1.3	Application of MD to track formation	67
	Equilibration	68
	Heating of a central zone	69
	Time-dependent MD	70
2.4.2	Features and deficiencies of the simulation	70
2.4.3	Results	72
2.4.3.1	$R_{hot}-T_{hot}$ - ($R-T$ -) plane	72
	Conclusion	75
2.4.3.2	Comparison to calculated temperature distributions	75

2.5	Conclusions and outlook	78
3	Nano-hillock formation	81
3.1	Introduction	81
3.2	Experimental evidence - threshold behavior	82
3.3	Energy deposition to the lattice	84
	Basic mechanism	84
	Time scales	85
	Review of theoretical results for the first two steps	85
3.4	Energy diffusion in the lattice and restructuring	88
	Presence of a surface	88
	Shape of the “hot” zone	88
3.4.1	Results	89
3.4.1.1	Snapshots	89
3.4.1.2	Threshold behavior	89
3.4.1.3	Height and width of simulated hillocks	92
3.4.1.4	Target temperature dependence	93
3.4.2	Conclusions and outlook	94
3.5	Comparison between track and hillock formation	95
4	Summary and conclusions	97
	Appendices	101
A	Equilibrium charge state	101
A.1	Introduction	101
A.2	Application to Xe in CaF ₂	104

<i>Contents</i>	7
B Calculation of the wake potential	106
C Time-dependent perturbation theory	108
Scaling behavior	111
D The fluorite lattice structure	113
E Calculation of the pair correlation function	116
F Estimate of thermal diffusivity	118
Bibliography	123
Acknowledgements	141

Abstract

Investigations of the interactions of fast heavy particles and slow highly charged ions (HCI) with insulator targets have shown common features. Above a threshold energy (kinetic energy for fast heavy particles, potential energy for slow HCI), restructuring of the target material was observed leading to track formation in the bulk of the insulator and/or nano-hillock formation at its surface. Recently, a microscopic mechanism for the creation of nano-hillocks by slow HCI has been proposed [1], modelling lattice heating due to electron-phonon interaction and giving temperature distributions in the lattice around 100 fs after the HCI's impact.

Following the same idea, this work investigates the creation of tracks by swift heavy ions in an ionic crystal, CaF_2 . Ionization of the target by swift projectiles is modeled using time-dependent perturbation theory. The electrons excited to the conduction band are propagated and excite phonons thereby heating the target lattice. Melting and restructuring are modeled in a proof-of-principle molecular dynamics (MD) simulation.

The same MD simulation is used to extend the model for nano-hillock formation to the picosecond time scale. Threshold behavior is observed for track as well as hillock formation. Similarities between the processes are investigated and other processes which could be simulated by similar methods are suggested.

List of symbols in the order of appearance

Symbol	Description (page of first mention)
E_p	projectile energy (p. 19)
$S(E_p)$	stopping power (deposited energy per path length) (p. 19)
v_p	projectile velocity (p. 20)
v	electron velocity (p. 24)
E_i	ionization potential (binding energy) of an electron, $E_i > 0$ (p. 24)
Z_p	projectile equilibrium charge state (p. 24)
Z_t	(effective) target charge (p. 30)
E	electron energy (p. 30)
σ_{ion}	total ionization cross section (p. 31)
\vec{q}	momentum transfer to electron (p. 31)
n_i	principal quantum number (p. 34)
λ_{ion}	total ionization mean free path of the projectile (p. 36)
n	total electron number density (p. 36)
λ_i	contribution of shell i to λ_{ion} (p. 36)
$\langle E \rangle_i$	average energy of ejected electron from shell i (p. 36)
$\sigma_{el}(E)$	elastic scattering cross section in electron transport (p. 42)
E_{gap}	energy gap between valence and conduction band (CaF ₂ : $E_{gap} \sim 12$ eV) (p. 42)
$\sigma_{in}(E)$	inelastic scattering cross section in electron transport (p. 43)
ΔE	energy loss of primary electron in inelastic collision (p. 43)
E_{phonon}	optical phonon peak energy (CaF ₂ : $E_{phonon} \sim 58$ meV) (p. 43)
λ	total electron mean free path (p. 45)
λ_{el}	total elastic electron mean free path (p. 46)
λ_{in}	total inelastic electron mean free path (p. 46)
N_{phonon}	effective number of phonons emitted in one quasi-elastic scattering event (p. 50)
R	distance from track axis for tracks, or center of hemisphere for hillocks (p. 53)
$\rho_E(R)$	energy density in distance R from center (p. 54)
T	temperature (p. 54)
E_{melt}	melting energy density (CaF ₂ : $E_{melt} \sim 0.55$ eV/atom) (p. 54)
E_{room}	energy density corresponding to room temperature (300 K) (p. 54)
N	number of atoms in the molecular dynamics (MD) simulation) (p. 64)
T_{bath}	temperature of heat bath (target temperature) (p. 68)
T_{hot}	(final) temperature of the “hot” region in MD simulations (p. 69) (abbreviated as T if no confusion is possible)
R_{hot}	radius of the “hot” region in track and hillock MD simulations (p. 69) (abbreviated as R if no confusion is possible)
$g(r)$	pair correlation function (radial distribution function) (p. 73)

1 Introduction

After irradiation with swift heavy ions a strongly damaged zone can be found in a variety of materials. Around the path of individual projectiles, cylindrical tracks with typical diameters of a few nm are formed. The left panel of fig. 1.1 shows a cross-sectional TEM (transmission electron microscope) image of such tracks. Depending on the target, the tracks consist of amorphous material or contain lattice or electronic defects. Track formation is common in insulators, in particular in ionic crystals. In any case, track formation was observed only if a threshold in the stopping power of the projectile was exceeded.

Track formation and its applications have been studied for several decades, starting with photographic plates used to detect cosmic radiation [2]. Today, this basic technique is still used to measure the heavy ion dose in space dosimetry [3] in combination with thermoluminescent detectors (TLDs). Controlled modification of material properties using irradiation with ion beams has become a widely used technique in applied fields [4–6], e.g. ion beam lithography. Recently, track formation and subsequent etching has been used for the fabrication of capillaries that are used to guide ion beams [7]. Furthermore, tracks can be used to pin the magnetic flux lines in superconductors, increasing the critical temperature, field, and current density [8, 9].

Experimental as well as theoretical work [10–15] seeking to understand the relevant mechanisms abounds. Early theoretical models include the two-temperature model [16, 17]. A descendant is the “thermal spike” model [18–23] which has been successfully applied to experimental findings.

According to this model the energy is transferred from the projectile to the electronic system of the target, which couples to the lattice, leading to melting and restructuring. This mechanism is modeled by two coupled one-dimensional radial heat diffusion equations for the electronic system and the lattice of the target, where the coupling is a free parameter (“electron-phonon coupling constant”). If the temperature of the target lattice in distance r from the track axis rises above the melting temperature, it is considered as “molten”, and supposed to contain defects upon recrystallization. The diameter of the experimental track is given by $r_{exp} = \max\{r\}$. In general, agreement with experiment is good. Limitations include the need for a free parameter and the doubtful validity of macroscopic models (the track radius, $\sim 50 \text{ \AA}$, is only around 50 nearest neighbor distances but is treated as continuum). Furthermore, material dependent parameters (e.g. heat capacity and thermal conductivity) are taken from data tables for moderate ambient conditions but are supposed to be correct under the extreme conditions encountered in the central region of the track (extremely high temperatures and non-equilibrium).

A more qualitative model has been given by Chadderton [15]. The track formation process is interpreted as the interplay between a “heating wave” which flows from the projectile path outwards and an inward-flowing “cooling wave” which heals the crystal.

In this work, we in contrast propose a *microscopic* model for track formation to overcome these deficiencies. The process is divided into three sub-processes

which take place on different time scales so that they can be modeled in sequence: energy deposition from the projectile to the electronic system of the target, energy diffusion from the electronic system into the lattice, and atomic motion. Results of the preceding step are used as input for the subsequent step. Due to the different scenarios in each step, methods from numerous fields are applied, each with different approximations and validity criteria; among them are time-dependent perturbation theory, electron transport including electron-phonon-interaction, dielectric theory, and molecular dynamics. Wherever possible, experimental data is used to provide a realistic description. Comparison to experiment and to theoretical calculations obtained by different means provide tests for the model.

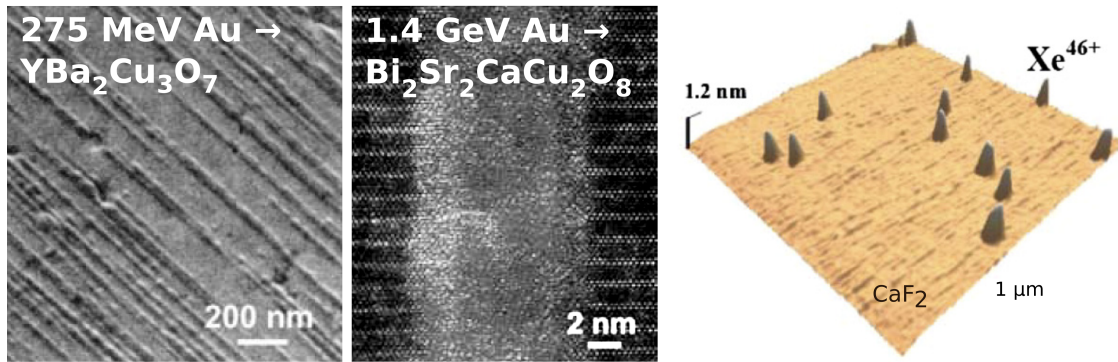


Figure 1.1: Left: Scanning electron microscopy image of ion tracks produced by 275 MeV Au ions under gracing incidence on $\text{YBa}_2\text{Cu}_3\text{O}_7$ grown on MgO substrate [23, 24]. Center: High-resolution electron microscopy image of an amorphous track zone produced along the trajectory of one 1.4 GeV Au ion in crystalline $\text{Bi}_2\text{Sr}_2\text{CaCu}_2\text{O}_8$ [23, 25]. Right: AFM image of CaF_2 after irradiation with slow highly charged ions. Nano-sized hillocks are observed. Fig. taken from [26].

Signatures of a similar mechanism have been found in the interaction of ions with surfaces. While experimentally observed surface modifications in ion-surface interactions include well-ordered patterns like ripples or dots [27–29] we will focus on the recently found “potential hillocks” [26] induced by *slow highly charged* ions

(HCl).

These potential or “nano-” hillocks have been found on several materials, e.g. on dielectric targets (see right panel of fig. 1.1). As for track formation, the hillocks can be linked to the impact of single ions. A threshold *potential* energy (charge state) of the ion is required for hillock creation. Model calculations show that this threshold can be linked to nano-scale melting of the crystal around the ion impact site [1, 26] where the largest part of the ion’s energy is deposited.

In this work, we will try to investigate the link between the two phenomena. We will concentrate on one material, CaF_2 , in which both hillock and track formation have been observed. A theoretical framework for hillock creation has been proposed in [1], centered on energy deposition of the ion’s potential energy to the target electronic system and subsequent lattice heating by electron-phonon coupling. We will extend this model to the picosecond time scale by a molecular dynamics simulation of the restructuring of the heated lattice similar to track formation.

This work is organized as follows: First, we will summarize our model for track formation, outlining the nature of the problem and the different methods needed to calculate the various parts of the model and their approximations (chapter 2). Then, we will briefly summarize the experimental evidence and some theoretical results on hillock formation before proposing an extension to the current theory by the same means which we use for the simulation of tracks. We will outline the differences and the similarities between the two processes, and propose other cases to which the present simulation could be applied (chapter 3). A graphical summary of the proposed model for track and hillock formation including the numerous input sources is given in fig. 1.2.

Atomic units ($m_e = \hbar = e_0 = 1$) are used unless otherwise stated.

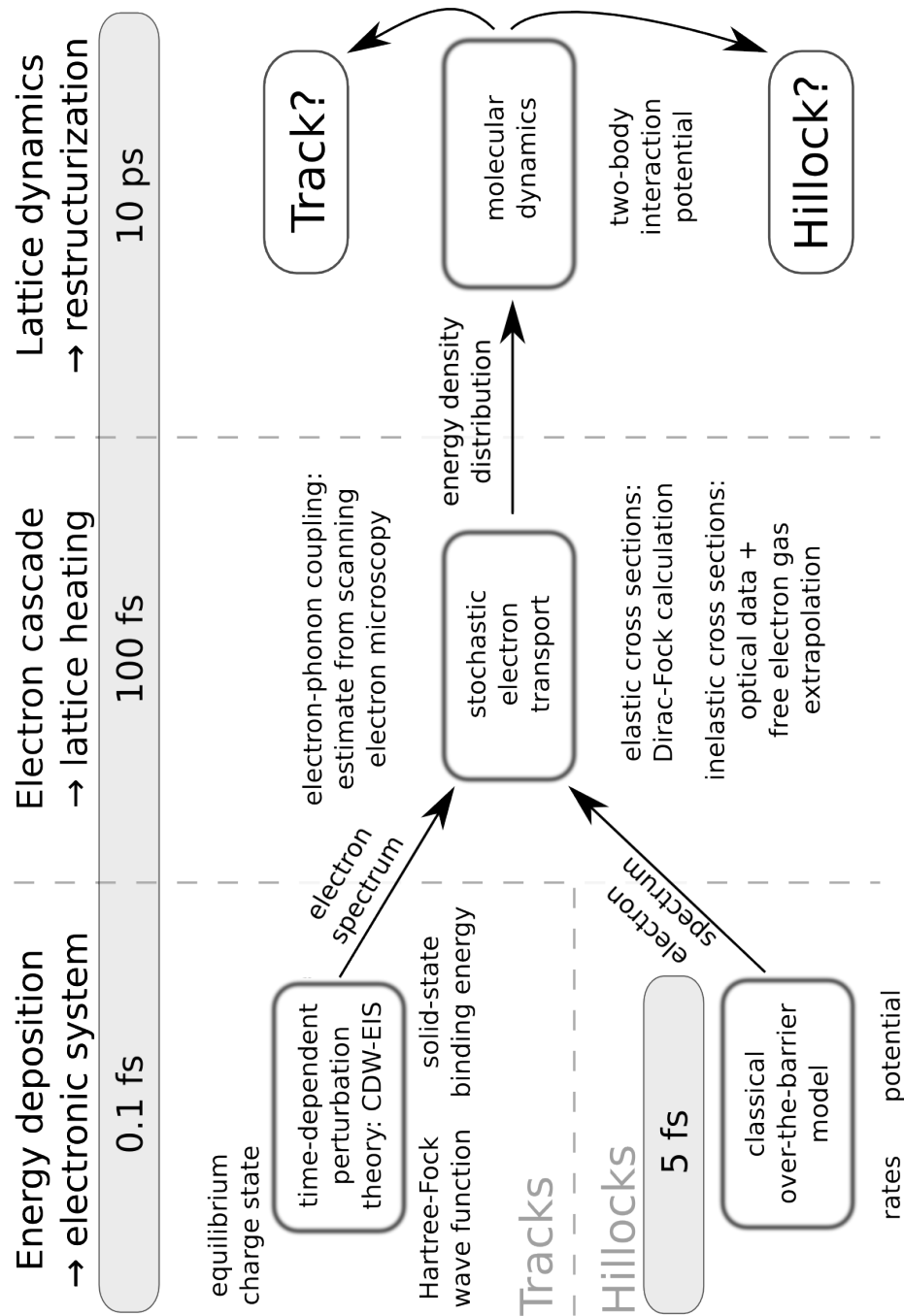


Figure 1.2: Graphical summary of unified model for track and nano-hillock formation including input data.

2 A microscopic model for track creation

In this chapter we will first briefly explain our model and make order-of-magnitude estimates showing that we can divide track creation into three subprocesses (energy deposition into the electronic degree of freedom of the target, energy diffusion in the electronic system and energy deposition to the lattice, and atomic movement and eventually restructuring). Then, we go into detail about the methods and approximations we use to model each subprocess discussing the results at the end of each section.

2.1 Overview: analysis of time scales

The passage of swift heavy ions through some materials, in our case an ionic insulator (CaF_2), creates tracks along the ion's path if the average energy transferred to the medium along a unit path length (stopping power $S(E_p)$ at projectile energy E_p) is above a certain threshold, see fig. 2.1.

In this section, we will propose a microscopic mechanism in which the energy is at first deposited in the electronic degree of freedom of the target, from where it is transferred to the lattice (phononic degree of freedom) which, in turn, leads

to restructuring. To be able to understand this process, let us first look at the different time scales involved.

Energy deposition to the target. The swift heavy ion deposits its energy during the time it passes the target atoms. For projectile velocities v_p of about 3 to 30 a.u. which are required for track formation, a unit cell with a lattice constant of roughly 5 Å is passed in less than 10^{-16} s or 0.1 fs. Electrons of elevated energy are left behind.

Electron cascade and energy transfer to the lattice. Let us consider 10 eV as a characteristic energy for the quasi-free ejected electrons, which amounts to a velocity of ~ 20 Å/fs. During the passing of the projectile (0.1 fs), their motion can therefore be neglected. We estimate a range of the order of 100 Å for the electrons (compare also section 2.3). Assuming continuous slowing down, we find that the electrons reach 99 % of their range within $\lesssim 100$ fs.

Energy diffusion in the lattice and restructuring. In order to derive a characteristic time scale for lattice restructuring, we start with the speed of sound in CaF₂, which is of the order of ~ 3.8 km/s [30] or 0.04 Å/fs. The time it takes a sound wave to propagate from the track axis to the experimental track radius is a lower bound to the time scale for lattice dynamics. Assuming 50 Å for the track radius, we find this lower bound of the characteristic time span to be >1 ps, much longer than the duration of the electron cascade.

Conclusion The above back-of-a-napkin calculation shows that the process of track creation can be divided into three subprocesses which happen in time scales which are orders of magnitude apart. Thus, we can assume that the steps happen

one after another. We can model each of the steps independently, taking the result of one step as input data for the next one. This enables us to model a process stretching over 5 orders of magnitude in time, which would not be feasible otherwise.

2.2 Energy deposition to the target

In this section, we describe our model of the primary energy transfer, from the incident projectile to the electronic system of the target. We review the basic mechanisms of energy transfer that exist and single out the most important one, i.e. ionization. We explain modelling the ionization of bound target electrons by a moving ionic projectile using time-dependent perturbation theory, including the approximations that must be made to render the problem tractable. Finally, we present the results of the simulation and compare them to experimental results.

2.2.1 Mechanisms of energy transfer

A swift charged particle moving in a solid can transfer its energy to the solid by two different mechanisms. The first is elastic collisions between the ion and the target nuclei, called “nuclear stopping”. The second comprises all possible excitations of electronic degrees of freedom and is thus called “electronic stopping”. The program SRIM [31] (“Stopping and range of ions in matter”) accesses a large database of experimental results and uses scaling laws to give estimates for the stopping power of any given particle in any given medium. Fig. 2.1 shows the SRIM estimate for the stopping power of a Xe projectile of different energies E_p . In experiments, a threshold stopping power of $0.5 \text{ keV}/\text{\AA}$ is observed for the formation of tracks (red dashed line in fig. 2.1).

Nuclear stopping does not play a substantial role in the energy regime where the stopping power is larger than the threshold for track formation (c.f. fig.2.1). At the lowest energies that will be treated in this work ($\sim 3 \cdot 10^7 \text{ eV}$), its contribution is only 5 % and vanishes rapidly for higher energies. Therefore, we concentrate on the energy deposition to the electronic system of the target.

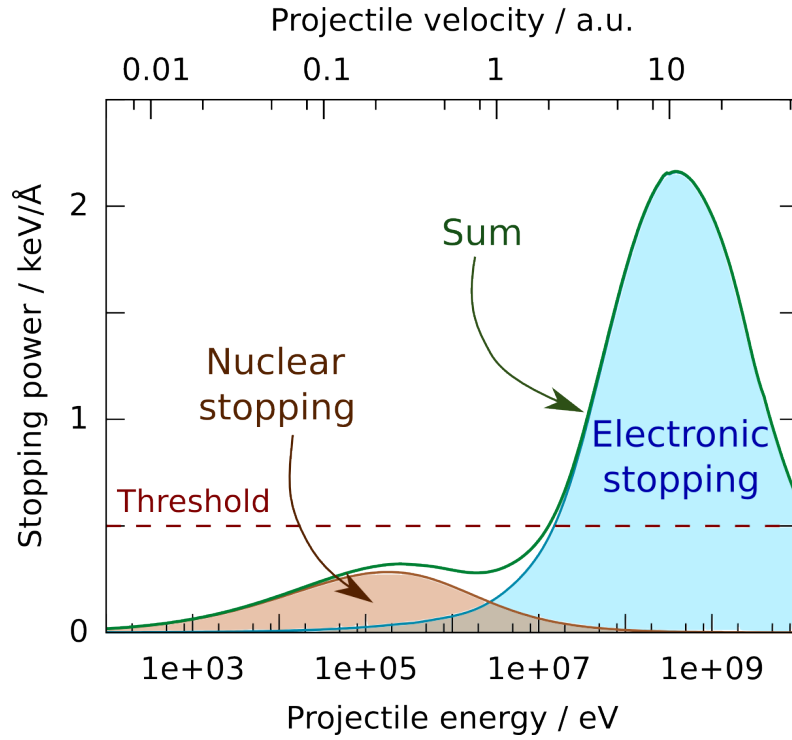


Figure 2.1: Stopping power of Xe in CaF_2 as given by SRIM [31] (random direction of incidence). Contributions from nuclear stopping dominate at low energies. The horizontal dashed line represents the experimental threshold for track formation. Track formation is experimentally observed for stopping powers above $0.5 \text{ keV}/\text{\AA}$, which corresponds to projectile energies from $10^7 - 10^{10} \text{ eV}$ or projectile velocities from 3 to 30 a.u.

Within the realm of electronic excitations, one can further distinguish several types of reactions:

Electron capture and loss The projectile can capture one of the target electrons to a bound projectile state by lowering the potential barrier through the Coulomb potential of the projectile. For high projectile charges and target valence electrons, the electron will usually be captured to an excited projectile state.

On the other hand, the reversed process is possible: The projectile might lose weakly bound electrons to the target. Due to screening of the projectile by the tar-

get electrons and collisions with target cores outer electrons can be stripped off. A good first estimate is found by comparison of orbital and projectile velocities. Only electrons with orbital velocities faster than the projectile velocity are considered to remain bound to the projectile.

For example, consider a projectile energy E_p of 30 MeV, which corresponds to a stopping power slightly above the threshold for track formation (fig. 2.1). The velocity of the Xe projectile ($Z_{Xe} = 54$, $m_{Xe} = 131.293$ amu) is then about $v_p = 3$ a.u. An electron which moves with the same velocity $v = v_p$ around its orbit has a total energy (binding energy) of ~ 120 eV, as can be seen from the Virial theorem¹. In the ground state of xenon [32], the electrons from the 4d, 5s, and 5p shells are bound more loosely than that. Therefore, they are stripped off, leaving the projectile with a net charge of $Z_p = 18$. On the right side of the stopping power graph in fig. 2.1, at about 3.5 GeV, the projectile moves at a speed of around 33 a.u. which corresponds to an electron binding energy of ~ 15 keV. Only the 1s electrons are bound tighter than that, leaving a net charge of $Z_p = 52$.

¹ The Virial theorem states that for a stable system governed by Coulombic forces [33],

$$E_{pot} = -2E_{kin}$$

with E_{pot} the total potential and E_{kin} the total kinetic energy of the system. We consider an electron of total energy E_i below vacuum (binding energy), which is given by the sum of the kinetic and potential energies

$$E_i = E_{kin} + E_{pot}$$

and thus is related to the orbital velocity v and mass m_e of the electron as

$$-E_i = E_{kin} = \frac{m_e v^2}{2} \quad .$$

Solving for v yields

$$\frac{v}{\text{a.u.}} = \sqrt{\frac{-E_i}{1\text{Ry}}} \quad ; \quad 1\text{Ry} = 13.605692\text{eV} \quad .$$

A balance of electron capture and loss will be established, leading to an “equilibrium charge state”. More elaborate calculations as well as experiments have been done to investigate these processes. Here, we use [34], where experiments were analyzed that measure the charge state of different projectiles of different energies after they have passed thin foils of different materials. They give an analytical formula which allows the calculation of equilibrium charge states for a large range of systems, with an error of only about $\pm 0.5(e_0)$. For the cases mentioned above, we calculate a projectile net charge of 16 and 52, respectively, which is quite close to our estimates (18 and 52). Further details on the equilibrium charge, charge state distributions and the formulae used can be found in appendix A. We note that we restrict ourselves to the part of the track where the equilibrium charge state has been reached. We assume that in total electron capture and loss do not contribute much to the stopping power and we have therefore not included them in our simulation.

Target excitation and ionization The projectile interacts with the electrons of the target and transfers some of its kinetic energy to them leaving them in either an excited target state (excitation) or a continuum state (ionization). Since all target states are occupied up to the valence band in the ground state, a vacancy would have to be formed before a target electron from a deeper level could be excited there, making excitation improbable compared to ionization.

On the other hand, the solid-state nature of the target gives rise to additional energy loss channels. For example, excitons can be created. These bound states of target electrons and their holes have energies just below bottom of conduction band. Furthermore, the target is a dielectric and will thus shield the projectile. The induced charge density leads to a wake potential around the projectile which in turn

leads to a retarding electric force on the projectile. The energy lost by the projectile is stored in the electronic system of the medium in the form of electron-hole pairs. The wake potential provides a way to estimate the distance up to which the medium effectively “feels” the presence of the projectile. This response is larger for higher projectile charges (stronger potential) and lower projectile velocities (which give the medium more time to react). Fig. 2.2 shows the wake potential (normalized to a unit charge) in CaF_2 at a projectile velocity of 3 a.u. Details of the calculation are given in appendix B. Consistent with a later estimate based on the stopping power, we find that the influence of the projectile on the medium is small for distances larger than $\sim 10 \text{ \AA}$. We assume that the contribution of excitons and other excitations are small compared to ionization losses.

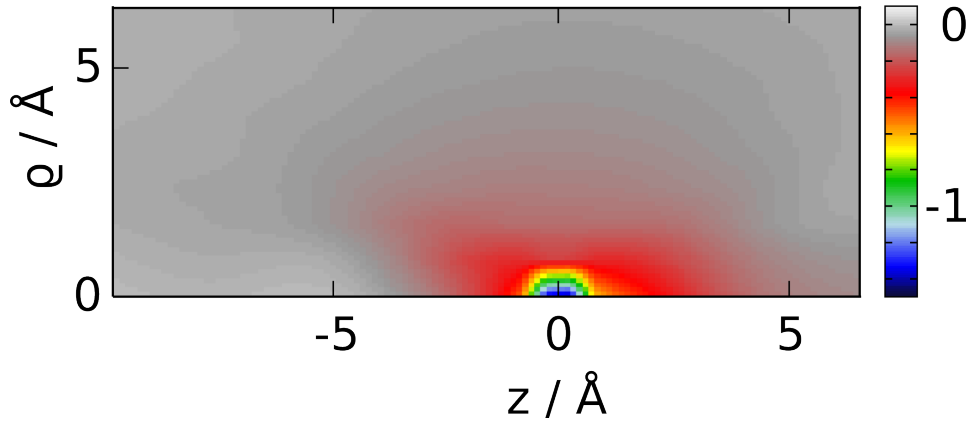


Figure 2.2: “Reduced” wake potential $\phi_{wake,red}$ of a projectile of velocity 3 a.u. (in $+z$ direction) in CaF_2 . $\phi_{wake,red}$ is related to the total potential ϕ as $\phi = Z_p \left(\frac{1}{R} + \phi_{wake,red} \right)$.

2.2.2 Target ionization

2.2.2.1 Simplifying the system to a 3-body-problem

The problem of a charged particle with its bound electrons interacting with the electronic system of a solid consisting of N electrons with N of the order of Avogadro's number ($N_A = 6 \cdot 10^{23}$) requires additional simplification to be tractable.

Equilibrium charge state of the projectile The projectile is assigned an equilibrium charge state Z_p reflecting the balance of electron capture and loss. We determine Z_p according to a fit to experiments on many projectile-target combinations [34], see appendix A. For the following calculations we treat the projectile as a point charge of strength Z_p .

Independent ionizations The next approximation is to treat ionizations as independent events. This enables us to calculate the probability of ionization for one target electron individually and derive the total ionization probability from the spatial density of electrons. For this approximation to be valid, two conditions must be met: First, multiple ionization from one target atom must be treatable by an independent electron approximation. This is justified if correlations can be ignored and if the motion of the projectile can be treated in a classical manner [35]. Experimental evidence shows that these assumptions are met for our case [36–38]. Second, the ionization processes from different target atoms have to be treatable as independent of each other. The approximation is justified if the characteristic distance between target atoms is much larger than the characteristic interaction distance with the projectile. This is not the case here, since the (screened) Coulomb potential of the projectile can ionize atoms several interatomic distances away from

its position. To get an estimate, we analyze the magnitude of the stopping power necessary for track formation (compare fig. 2.1). We assume for simplicity that the projectile loses on average 50 eV in each ionization event (the band gap of CaF_2 is 12 eV, binding energies of core electrons range up to 4 keV; later, we will calculate this value and find ≈ 50 eV). Then, 10 ionization events are required in 1 Å path length to reach the threshold stopping power of 500 eV/Å required for track formation. At the velocities and projectile charges where the cross sections are largest, multiple ionization probabilities are of the order of 20 % of the single ionization probability [39]. For simplicity, we assume one ionization per atom. Then, the projectile has to ionize 50 atoms while it traverses one unit cell (5.46 Å). With 12 atoms per unit cell (c.f. appendix D), we obtain a characteristic distance of ~ 6 Å or 8 unit cells that interact with the projectile. For larger stopping powers, this model gives larger characteristic interaction distances, always of the order of 10 Å, which is clearly larger than the nearest-neighbor distance of about 2 Å. This estimate is also consistent with the calculation of the wake potential presented in fig. 2.2.

Even though the premises of the approximation are not satisfied, a more elaborate approximation that is still tractable is difficult to find. Furthermore, results closely resembling the experiment have been calculated in this approximation (e.g. [40]).

Independent electrons: single active electron We are now left with a point charge impinging on a target atom with up to several tens of electrons. To further simplify the calculation, the single active electron model is employed: we distinguish between the electron that is ionized and the electrons that are left behind. The latter are treated as “frozen”, i.e. they act as spectators of the ionization process, and their state remains unchanged during the ionization. Electron correlations in the ground state, i.e. before the ionization, are considered in the spirit of a

mean field theory leading to an effective potential for the electron to be ionized. The probability for ionization of any electron from a certain state is given by the ionization probability for one electron times the number of electrons in that state.

Multiple ionization plays a role for charge states Z_p and projectile velocities v_p lower than the stopping power maximum; its importance decreases towards higher projectile energies. It is difficult to estimate the contribution of multiple ionization, especially as there are no data for ions in a solid. In atom-ion collisions maximum ratios of single to double ionization of $\sim 20\%$ [39] are obtained for similar collision parameters Z_p and v_p as used in this work. We neglect multiple ionization and show the validity of this approximation later by comparison to other data. It is possible to calculate multiple ionization probabilities in the independent particle model [35, 39, 41] given the ionization probabilities for all electrons as a function of impact parameter. This information could, in principle, be obtained using the time-dependent perturbation theory treatment we propose later in this section [42]. However, it would require rewriting the implementation used in this work.

Further adaptations have to be incorporated into our model to account for the ionicity of the target constituents Ca^{2+} and F^- . Electronic structure calculations [43] show that the electron density can be attributed to the ions according to their nominal charges. Linear combination of atomic orbitals (LCAO) calculations [44] show that the valence band of CaF_2 almost entirely consists of $\text{F}(2p)$ orbitals, with only minor admixtures of Ca levels. More deeply bound levels are only weakly influenced by the crystal potential. We therefore conclude that the atomic orbitals of Ca^{2+} and F^- are good approximations to the true electron wave functions. The binding energy of the electrons of the considered shells is adjusted to match the experimental value [45] (see section 2.2.2.2).

Continuum After ionization, the electrons are transferred to continuum states of the target. From band structure calculations (e.g. [43]) it is known that the dispersion relation of continuum states for electrons in CaF_2 is, to a good approximation, parabolic, i.e. similar to that of free electrons.

2.2.2.2 Time-dependent perturbation theory

We are now left with the following problem: the projectile, a point charge of strength Z_p , impinges with velocity v_p on a target atom of effective charge Z_t (see below) with one active electron. The effect of other electrons is partly taken into account through the initial wave function of the active electron and the effective target charge Z_t . We calculate the probability to find the electron in a continuum state moving with energy $E = \frac{v^2}{2}$ in direction θ with respect to v_p after the passage of the ion (doubly differential ionization cross section). The situation is depicted in fig. 2.3. For simplicity, we consider a fixed impact parameter b [46, 47].

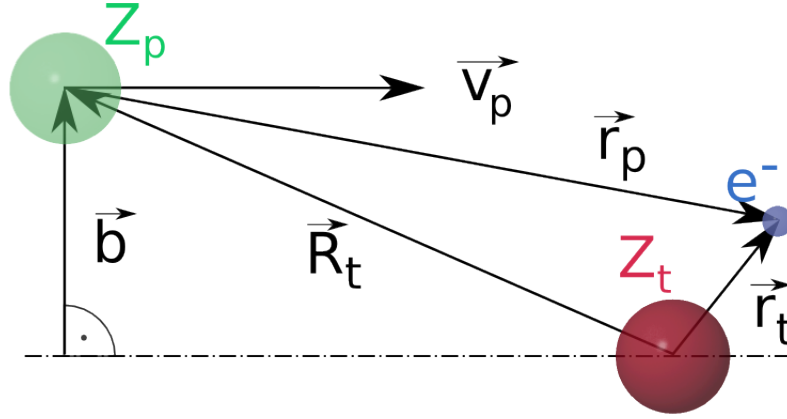


Figure 2.3: Depiction of ionization geometry. The projectile (green) with charge Z_p and velocity \vec{v}_p passes the target with nuclear charge Z_t (red). The minimum distance between them (impact parameter) is $|\vec{b}|$. The relative position vector between projectile and target core is \vec{R}_t . The target has one active electron (blue) with relative position vector \vec{r}_t to the target core. The vector from the projectile to the electron is $\vec{r}_p = \vec{r}_t - \vec{R}_t$, and $\vec{R}_t(t) = \vec{v}_p t + \vec{b}$.

Appendix C gives a brief account of the general method of time-dependent perturbation theory as applied to ion-atom collisions. The doubly differential ionization cross section for the ejection of an electron into the solid angle $d\Omega$ with energy E is given by [48]

$$\frac{d^2\sigma_{ion}}{d\Omega dE} = k_t \frac{1}{4\pi v_p^2} \int_{q_{min}}^{\infty} dq q \int_0^{2\pi} d\phi_q |T_{i,f}|^2 \quad (2.1)$$

where infinite masses for the nuclei are assumed, k_t is the momentum of the electron relative to the target and $T_{i,f}$ is the transition matrix between the initial state $|i\rangle$ and the final state $|f\rangle$. The momentum transfer is given by $\vec{q} = \vec{K}_i - \vec{K}_f$ where \vec{K}_i and \vec{K}_f label the initial and final projectile momenta with respect to the target. ϕ_q is the azimuthal angle of \vec{q} , and the integration limit is $q_{min} = \frac{E+E_i}{v_p}$ with E_i the ionization potential of the initial bound state $|i\rangle$. The different approximations available for the treatment of ionization differ in the choice of the perturbation and the initial and final states.

2.2.2.3 CDW-EIS: Continuum distorted wave - eikonal initial state

The CDW approach was initially developed for charge transfer processes [49, 50] and has later been applied to ionization in its CDW-EIS form [51]. For a detailed introduction that cannot be given here the reader is directed to [52]. An exemplary comparison that shows the improvement of CDW-EIS over simpler approximations as compared to experiments can be found in [53].

The final wave function is a continuum distorted wave of the form (with r_p , r_t and R_t as in fig. 2.3)

$$\xi_f^- = \phi_f^- D^-(Z_p, \vec{k}_p; \vec{r}_p) \quad (2.2)$$

with

$$\begin{aligned}
\phi_f^- &= e^{i\vec{K}_i \cdot \vec{R}_t} \psi_{t,\vec{k}_t}^-(\vec{r}_t) \\
\psi_{t,\vec{k}_t}^-(\vec{r}_t) &= \frac{e^{i\vec{k}_t \cdot \vec{r}_t}}{(2\pi)^{\frac{3}{2}}} D_t^-(\vec{k}_t; \vec{r}_t) \\
D_t^-(\vec{k}_t; \vec{r}_t) &= D^-(Z_t, \vec{k}_t; \vec{r}_t) \\
&= e^{\frac{\pi\alpha_t}{2}} \Gamma(1 + i\alpha_t) {}_1F_1(-i\alpha_t, 1, -i(\vec{k}_t \cdot \vec{r}_t + k_t r_t)) \\
\alpha_t &= \frac{Z_t}{k_t}
\end{aligned}$$

where $\psi_{t,\vec{k}_t}^-(\vec{r}_t)$ is an incoming continuum state of the electron in the field of the target ion with momentum \vec{k}_t , D_t^- and D^- are distortion factors due to the projectile and target, respectively, and ${}_1F_1$ is the confluent hypergeometric function of the first kind. This description has the correct asymptotic behavior in the limit of large internuclear distances for the electronic degree of freedom. It behaves as a continuum state of the two-center combined Coulomb fields of the projectile and the target. Of course, this is only true in the case of atom-ion collisions. In the solid, the field of the projectile and the residual target will eventually be shielded while the wave function of the electron evolves in the crystal potential. Therefore, a plane wave could be a better asymptotic approximation to the wave function of the ejected electron. However, the main features of the wave function are formed while electron, target, and projectile are close to each other, which makes this approximation preferable.

The application of the same idea to the initial state of the electron fails due to normalization issues [54] which lead to a divergence in the T matrix. In the CDW-EIS approximation, the initial state is therefore only distorted by an eikonal phase which is associated with the electron-projectile interaction:

$$\begin{aligned}
\eta_i^+ &= \phi_i^+ E^+(Z_p, \vec{v}_p; \vec{r}_p) \\
&= \phi_i^+ e^{-i \frac{Z_p}{v_p} \ln(\vec{v}_p \cdot \vec{r}_p + v_p r_p)}
\end{aligned} \tag{2.3}$$

with

$$\phi_i^+ = e^{i \vec{K}_i \cdot \vec{R}_i} \varphi_{\alpha_i}(\vec{r}_t) \tag{2.4}$$

where $\varphi_{\alpha_i}(\vec{r}_t)$ is the initial bound state of the electron. As mentioned above, the atomic orbitals of Ca^{2+} and F^- are good approximations to the electron wave functions. They are tabulated, e.g. in [55–59], in the form of expansion coefficients of exponentials, which is convenient for the CDW-EIS calculation (“Roothaan-Hartree-Fock”). We adjust the binding energy of the electron by tuning the effective target charge Z_t (see below).

The resulting CDW-EIS transition matrix is

$$\begin{aligned}
T(\vec{k}_t, \vec{q}) &= \langle \xi_f^- | V_f^\dagger | \eta_i^+ \rangle \\
&= -(2\pi)^{-\frac{3}{2}} \int d^3 r_p e^{-i \vec{q} \cdot \vec{r}_p} E^+(Z_p, \vec{v}_p; \vec{r}_p) \\
&\quad \times \nabla_{\vec{r}_p} D^{-*}(Z_p, \vec{k}_p; \vec{r}_p) \\
&\quad \times \int d^3 r_t e^{i \vec{s} \cdot \vec{r}_t} \varphi_{\alpha_i}(\vec{r}_t) \nabla_{\vec{r}_t} D_t^{-*}(\vec{k}_t; \vec{r}_t)
\end{aligned} \tag{2.5}$$

with V_f the residual ion potential and $\vec{s} = \vec{q} - \vec{k}_t$.

Effective target charge Z_t We chose the effective target charge Z_t according to Belkić's prescription (hydrogenic model, $1\text{Ry} = 13.6\text{ eV}$) as

$$E_i = 1\text{Ry} \frac{Z_t^2}{n_i^2} \quad (2.6)$$

where E_i is the experimental binding energy for the respective shell (distance to the bottom of the conduction band, taken from [45]) and n_i its principal quantum number. This is an empirical prescription which has been successful in predicting experimental results and has to be verified by comparison to experiment. From a physical point of view, it effectively re-scales the wave function to take into account the crystal potential of the solid in an approximate manner. Extensions of this model include the choice of different effective charges for initial and final wave functions. In ion-atom collisions, it has been shown that employing model potentials instead of the Coulomb potential leads to improvements over the hydrogenic approximation [48]. This way, one could also insert the wake potential of the projectile (compare fig. 2.2 and appendix B), which requires a customized implementation and much longer computation times.

Implementation We used a public domain implementation by McSherry [60]. Expansion coefficients for F^- were taken from [55], for Ca^{2+} coefficients for the isoelectronic Ar atom had to be used. Binding energies were replaced by the experimental values from [45].

Validity Most authors cite the validity criterion of Belkić [49],

$$E [\text{MeV}/\text{amu}] \geq 0.08 E_i [\text{a.u.}] , \quad (2.7)$$

which is purely empirical and requires verification by comparison to experiment.

The ion energies considered in this work range from 0.2 to 26 MeV/amu, the largest binding energy considered is about 2 a.u. for the Ca(3s) state. Condition eq. 2.7 is therefore fulfilled and reasonable agreement to experiment can be expected over the whole range of energies, with the largest errors expected in the low velocity regime.

2.2.3 Results

After some tests that reproduced literature results, we have calculated total, singly, and doubly differential ionization cross sections for ion impact on CaF₂. This was done for 5 different projectile energies (and therefore charge states, c.f. fig. A.3), and for the four weakest bound shells of CaF₂, i.e. F(2p) (binding energy $E_i = 14.4$ eV [45]), F(2s) (35 eV), Ca(3p) (31.6 eV), and Ca(3s) (50.2 eV).

2.2.3.1 Validity of the approximation - calculating the stopping power

Since we have claimed target ionization to be the most important process responsible for energy loss of the projectile, a comparison of the calculated stopping power in the energy range where track formation is possible with $\frac{dE_p}{dz}$ from other sources provides a test for the model.

The stopping power, sometimes called linear energy transfer, is given by

$$S(E_p) = \left| \frac{dE_p}{dz} \right|, \quad (2.8)$$

the absolute value of the amount of energy lost by the projectile dE_p along a path of length dz . Energy conservation requires that the energy lost by the projectile

has to be equal to the energy transferred to the medium. We now link this quantity to our calculated cross sections.

The mean free path λ_{ion} for ionization is the average distance between subsequent ionization events. It is related to the cross section σ_{ion} and the number density n of scattering partners (electrons) as

$$\sigma_{ion}\lambda_{ion} = \frac{1}{n} , \quad (2.9)$$

i.e. in a cylinder of base area σ_{ion} and height λ_{ion} there is on average one scattering partner. From the number densities of F and Ca atoms (c.f. appendix D) and the number of electrons per shell (2 for an s shell, 6 for a p shell) one can calculate the average electron number density. The different contributions λ_i ($i = \text{F}(2p), \text{F}(2s), \text{Ca}(3p), \text{Ca}(3s)$) contribute to the total ionization mean free path λ_{ion} as

$$\frac{1}{\lambda_{ion}} = \sum_i \frac{1}{\lambda_i} . \quad (2.10)$$

The average energy transferred from the projectile to the target in one scattering event δE is the ionization potential of the electron, E_i , plus the average energy of the ejected electron, $\langle E \rangle_i$:

$$\delta E_i = E_i + \langle E \rangle_i \quad (2.11)$$

where $\langle E \rangle_i$ can be calculated from the singly differential cross sections $\frac{d\sigma_{ion,i}}{dE}(E_p)$ which give the probability to find the ejected electron from shell i in a state with energy E for a certain projectile energy E_p . Averaging and normalizing we get

(dropping the index i in all terms)

$$\langle E \rangle = \frac{\int \frac{d\sigma_{ion}}{dE} E dE}{\int \frac{d\sigma_{ion}}{dE} dE} \quad (2.12)$$

where the denominator is equal to the total cross section.

The stopping power for an ionization process from a given shell (index i) can now be approximated by

$$S_i(E_p) = \left| \frac{dE_p}{dz} \right|_i \approx \frac{\delta E_i}{\lambda_i} \quad (2.13)$$

and the total stopping power is the sum of the stopping powers for the different processes ($i=F(2p), F(2s), Ca(3p), Ca(3s)$), c.f. 2.10

$$S(E_p) = \sum_i S_i(E_p) \quad . \quad (2.14)$$

Fig. 2.4 gives the result of the calculation. We are not aware of any measurements of the stopping power of Xe in CaF_2 in this energy range. Therefore, we compare our results to the stopping power given by SRIM [31] which should be accurate to around 20 %.

Over the whole range of energies, the stopping power graph is reproduced well, validating our model. At the lowest energy considered, 0.27 MeV/amu, the stopping power is around 30% smaller than predicted by SRIM, partly due to the negligence of nuclear stopping (~ 5 %). We observe that our calculation tends to underestimate the stopping power, which we ascribe partly to the neglected multiple ionization channel. The data point at $E_p \sim 600$ keV/amu gives a stopping power which is, against the trend, larger than the calculated SRIM results.

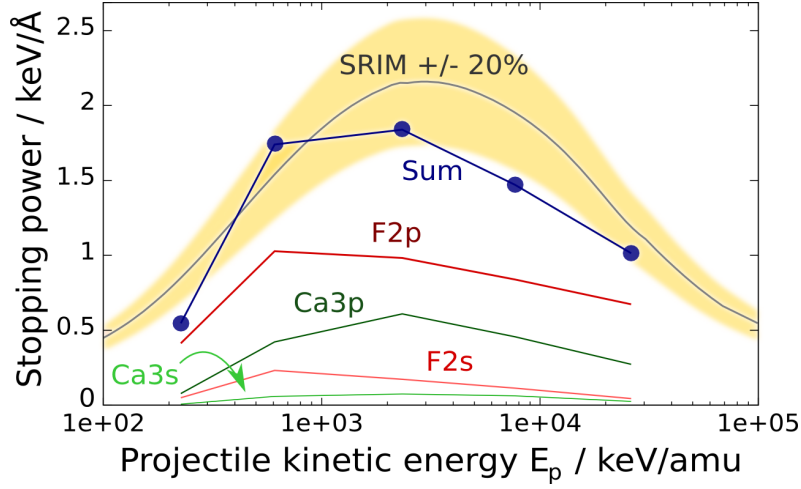


Figure 2.4: Comparison of stopping power calculated with CDW-EIS (blue points) and SRIM [31] versus energy. The contributions of the different shells to the total stopping power are depicted as indicated.

This can be attributed to the known over-estimation by CDW-EIS of cross sections near the maximum cross section $\sigma_{ion,max}(v_p = v_{max})$ with (at this E_p , Z_p) $v_{max} \approx v\sqrt{Z_p/Z_t + 1} \approx 3.5 \hat{=} 600$ keV/amu [61].

2.2.3.2 Discussion of singly differential cross sections

Figure 2.5 depicts singly differential ionization cross sections for a wide range of energies and projectile charge states investigated in this work.

As expected, the highest orbital (F(2p), blue) contributes most to the cross section. At higher energies, the contributions from lower shells increase compared to the F(2p) orbital.

In all cases, the majority of electrons is ejected with low to medium energies below 200 eV. The average kinetic electron energy is always well below 100 eV. Table 2.1 summarizes the results of the ionization cross section calculations.

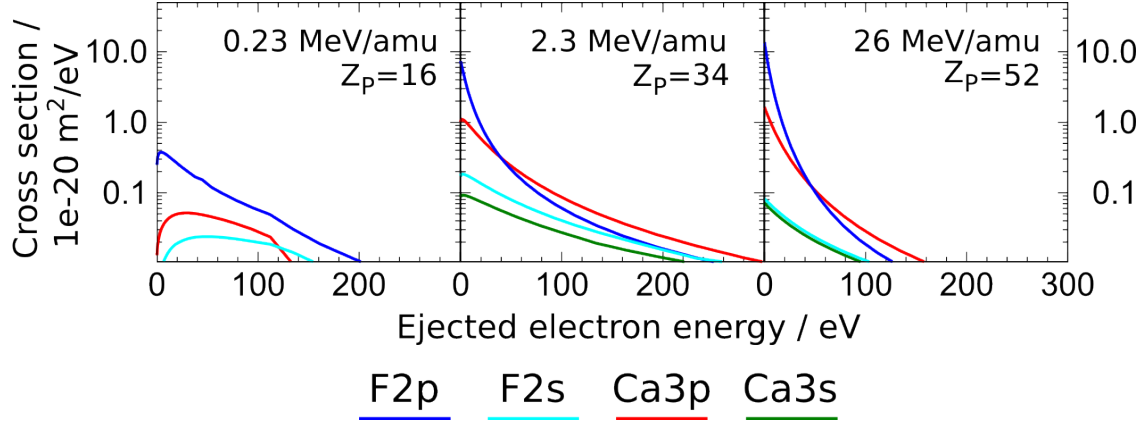


Figure 2.5: Singly differential ionization cross sections for the 4 highest target orbitals (F(2p), blue; F(2s), turquoise; Ca(3p), red; Ca(3s), green) for three different energies and charge states, which correspond to the left, center, and right of the stopping power graph, see fig. 2.4. On the leftmost picture, the cross section for the Ca(3s) orbital is below $10^{-2} \times 10^{-20} \text{ m}^2/\text{eV}$ for all electron energies.

Table 2.1: Details of the calculation of the ionization cross sections.

Projectile energy E_p [keV/amu]	Projectile charge state Z_p [e]	Total cross section σ_{ion} [Å ²]	Total projectile mean free path λ_{ion} [Å]	Average electron ejection energy $\langle E \rangle$ [eV]
226.21	16	29.7	0.142	60.0
608.56	23	90.5	0.051	70.3
2338.28	34	142.5	0.033	40.4
7692.72	44	142.1	0.031	27.0
26124.8	52	120.3	0.034	17.0

2.2.3.3 Summary

In this section, we have calculated doubly differential ionization cross sections in ion-atom collisions inside a solid. The approach is used to model the energy deposition from swift heavy particles to the electronic system of the medium. We use a one-electron time-dependent perturbation theory approach (CDW-EIS) which has

proven to be accurate in high-velocity ion-atom collisions. Hartree-Fock representations of the initial electronic wave functions are used. We tune a parameter of the CDW-EIS (“effective charge”) to match the experimental binding energy of the target. Our results for the stopping power (proportional to the total cross section) agree well with experimental data over a wide range of energies.

2.3 Energy diffusion in the electronic system and energy deposition to the lattice

2.3.1 Introduction

The second step in our three-step model is the energy diffusion in the electronic system and deposition of the energy to the lattice. In an intuitive picture, electrons with energies E_i (initial velocities) are released by the passing ion. They propagate inside the solid under the influence of elastic and inelastic scattering processes along their trajectory (fig. 2.6). Quantum mechanics enters our classical transport simulation through scattering cross sections (see below). In the following, we give a short overview over the possible interactions to be considered before describing each of them in detail.

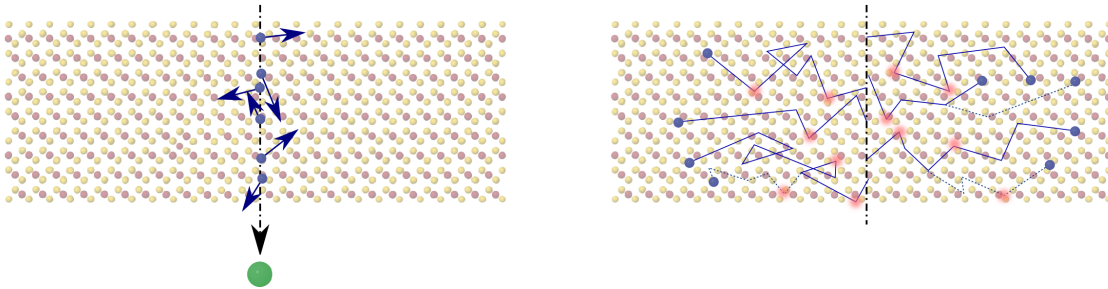


Figure 2.6: Schematic picture of the processes modelled in this chapter. Left: The ion (green) has passed the region of the crystal, leaving behind electrons (blue) along the track (dash-dotted line). Right: Electron cascades: electrons are propagated through the crystal, eventually being elastically deflected or creating secondary electrons through inelastic collisions. Phonon excitations (red spots) heat the target lattice.

First, electrons can be scattered elastically by the (mean-field) potential of a target atom (left panel of fig. 2.7). The initial energy $E = \frac{v^2}{2}$ (measured from the bottom of the conduction band) of the electron is unchanged but the direction

of the velocity vector changes. This change is often described in terms of the scattering angle θ between the velocity vectors prior to and after the collision. All the information is contained in the scattering potential, or, equivalently, in the energy dependent elastic differential cross section, $\frac{d\sigma_{el}}{d\Omega}(E)$. The latter gives a probability distribution for the scattering angle θ via $d\Omega(\theta) = \sin(\theta)d\theta d\phi$. The probability of the process is expressed via the energy dependent elastic total cross section $\sigma_{el}(E) = \int \frac{d\sigma_{el}}{d\Omega}(E) d\Omega$. The energy E of the electron is not changed in this process and the process can occur at any energy.

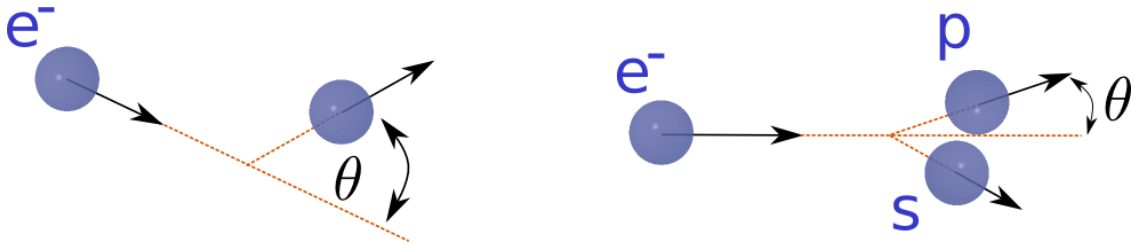


Figure 2.7: Schematic scattering geometry of the interactions. Left: Quasi-elastic scattering. The electron is scattered by the potential of a target atom by a scattering angle θ from its initial direction. Right: Inelastic scattering. The electron ionizes a target atom, producing a secondary electron “s”, while the primary electron “p” is scattered by the angle θ . The energy of the primary electron is reduced by the band gap plus the kinetic energy of the secondary electron.

Second, the electron may produce an electron-hole pair, thereby producing a secondary electron (right panel of fig. 2.7). Since the electron energy is reduced by $E_{gap} + E_{sec}$ (gap energy $E_{gap} \approx 12$ eV plus kinetic energy of the secondary electron after the collision), this is called an inelastic process. The process is only possible if the initial energy of the electron is large enough, i.e. higher than the binding energy of the secondary electron. Weakly bound electrons are more likely to be excited than core electrons. Another energy loss mechanism in free electron gases is plasmon excitation, a quasi-particle representing the collective motion of the

electrons. The plasmon eventually decays into an electron-hole pair or by emission of a photon. Electron-hole pair production and plasmon excitation are described by dielectric theory, see e.g. [62]. Here we assume it can also be applied to insulator targets [63]. Key quantity is the doubly differential inelastic scattering cross section $\frac{d\sigma_{in}}{d\Delta E d\Omega(\theta)}(E)$, depending on the energy of the incident electron. Probabilities for scattering angles θ and energy losses ΔE of the primary electron are derived from it.

If the electron energy becomes too small to allow for electron-hole pair excitation ($E < E_{gap}$), another energy loss mechanism is left: the excitation of phonons, quasi-particles of lattice vibration (heat). Due to the small energy loss (meV) this process is more similar to an elastic than an inelastic collision. Because of the kinematic limitations of the process ($m_e \ll m_{atom}$) the electron transfers only a small part of its energy to the atoms. To estimate typical energy losses, consider an electron which is backscattered from a (free) target atom. The momentum transfer will be almost like in a collision with a hard wall, $\Delta p \lesssim 2v$, which is also the momentum of the target atom after the collision. Expressing the energy of the target atom E_{atom} in terms of the electron energy E before the collision, we find $E_{atom} \approx 4 \frac{m_e}{m_{atom}} E$, which gives an energy loss of about 1 meV for a 10 eV electron in CaF_2 . With this estimate we are already within one order of magnitude of the excitation energy of a phonon in CaF_2 (acoustic phonon $\lesssim 30$ meV, optical phonon up to $E_{phonon} = 58$ meV [43, 64, 65]).

After the electron has lost all its energy, it may recombine radiatively, not contributing to the heating of the central zone. Recombination processes can also happen for electrons of higher energies and need not necessarily decay radiatively. In inelastic collisions, excitons can form instead of electron-hole pairs. Plasmon

excitations and excitons could both potentially couple to the phononic system and thus contribute to the heating process. Furthermore, it is difficult to assess the importance of these processes and also the time scales on which they happen.

We only model the above three processes (elastic and inelastic scattering and phonon excitation) in a stochastic electron transport simulation using classical transport theory, with initial conditions determined by the doubly differential electron ejection cross sections that were calculated in section 2.2. The electron is modelled as a classical point-like particle subject to stochastic scattering events. To reach statistical convergence many electron trajectories are calculated. The density of excited phonons corresponding to lattice vibrations (i.e. heat) serves as input for the subsequent MD simulation.

2.3.2 Electron transport

We solve the classical Langevin equation in the absence of an external force,

$$\dot{\vec{p}} = \vec{F}_{stoc}(\vec{r}, t) , \quad (2.15)$$

for a large ensemble of electron trajectories. The force $\vec{F}_{stoc}(\vec{r}, t) = \sum_i \Delta\vec{p} \delta(t - t_i)$ models momentum transfers $\Delta\vec{p}_i$ at discrete times t_i , which are chosen stochastically (see below). The momentum transfers account for elastic electron-atom potential scattering as well as inelastic scattering of the projectile electron. Trajectories of electrons released by inelastic losses are simulated as well.

We use an electron transport code that was originally developed in [66] and has since been applied to a large number of problems [1, 63, 67].

2.3.2.1 Initial conditions

The initial conditions for one electron trajectory are the initial position \vec{r}_0 and the initial momentum \vec{p}_0 .

Initial position For simplicity, we chose \vec{r}_0 to be on the track of the projectile. This choice is not obvious: we have already pointed out in section 2.2 that the characteristic interaction distance of the projectile potential is of the order of 10 Å and electrons are expected to be excited within this range. Later in this section, we will look into how smearing of the initial positions around the track axis changes the outcome of the simulation.

Initial momentum For the initial momentum of the electron, we use the results of section 2.2. Calculating the weighted sum of the doubly differential cross sections at a certain projectile energy E_p leaves us with a two-dimensional distribution for the probability of finding an electron with initial momentum $|\vec{p}_0|$ and emission direction θ (from the track axis).

2.3.2.2 Energy diffusion in the electronic system

The electron is propagated along straight lines between subsequent collisions. From the total electron mean free path λ the (Poissonian) probability density for a scattering event to take place after a path length s is given by

$$P(s) = \lambda^{-1} \exp(-s/\lambda) \quad , \quad (2.16)$$

where λ is determined from the mean free paths for both elastic and (different contributions to) inelastic scattering by

$$\frac{1}{\lambda} = \frac{1}{\lambda_{el}} + \sum_i \frac{1}{\lambda_{in}^{(i)}} . \quad (2.17)$$

Collisions can either be elastic or inelastic according to the ratio of their inverse mean free paths.

Elastic collisions In case of an elastic collision, the ratio of the relative concentrations of the elements constituting the target and their elastic scattering cross sections decide at which element the projectile will be scattered next. The scattering angle θ between the electron velocity before and after the collision is chosen from the energy dependent differential elastic scattering cross section $\frac{d\sigma_{el}}{d\Omega}(E)$ for that element, which was calculated using the ELSEPA code [68] (partial-wave solution for scattering states of the Dirac equation). In elastic collisions, the energy is conserved, i.e. the absolute value of the momentum does not change, $p' = p$. The momentum transfer $\vec{q} = \vec{p}' - \vec{p}$ defines the scattering angle θ .

Inelastic collisions In inelastic collisions, the energy of the incident electron is not conserved. The electron loses the energy ΔE and is deflected by θ from the incidence direction. For a given ΔE , the momentum transfer \vec{q} can be related to the scattering angle θ . The energy loss ΔE must be larger than the energy gap E_{gap} between valence and conduction bands (CaF₂: 12 eV). A secondary electron with energy $E_{sec} = \Delta E - E_{gap}$ and momentum derived from kinematics is added at the location of the scattering and is also followed on its way through the crystal, possibly leading to more secondary electrons.

Key input for inelastic collisions is the doubly differential cross section $\frac{d\sigma_{in}}{d\Delta E d\Omega(\theta)}(E)$ which gives the probability for an energy loss ΔE and a momentum transfer $q(\theta)$. It is customary to rewrite this quantity in terms of a doubly differential inverse mean free path $\frac{d^2\lambda_{in}^{-1}(E)}{d\Delta E dq(\theta)}$ (see eq. 2.9). It can be derived from dielectric theory applied to an electron moving in a solid, where the solid is characterized by a dielectric response function $\varepsilon(\vec{q}, \Delta E)$ [66]. The (Fourier components of the) total potential $\Phi(\vec{q}, \Delta E)$ in response to an external potential $\Phi_0(\vec{q}, \Delta E)$ is given by

$$\Phi(\vec{q}, \Delta E) = \frac{\Phi_0(\vec{q}, \Delta E)}{\varepsilon(\vec{q}, \Delta E)} \quad . \quad (2.18)$$

Inserting the Fourier transform of the charge density $\rho_0(\vec{r}, t) = -\delta(\vec{r} - \vec{v}t)$ of an electron moving with velocity \vec{v} into the Poisson equation, the external potential induced by the electron $\Phi_0(\vec{q}, \Delta E)$ is obtained. One can then define the doubly differential inelastic mean free path so that the stopping power $S(E) = \int d(\Delta E) dq (\Delta E) \frac{d^2\lambda_{in}^{-1}(E)}{d\Delta E dq}$ corresponds to the retarding force on the electron due to the electric field $-\vec{\nabla}\Phi(\vec{r} - \vec{v}t)$ at the position of the projectile. For an isotropic medium, the result is (with $\cos(\theta) = \frac{q^2/2 - 2E + \Delta E}{-2\sqrt{E(E - \Delta E)}}$):

$$\frac{d\lambda_{in}^{-1}(E)}{d\Delta E dq} = \frac{1}{\pi q E} \text{Im} \left\{ \frac{-1}{\varepsilon(q, \Delta E)} \right\} \quad . \quad (2.19)$$

The challenge is to find a sensible approximation to the dielectric function. For this purpose, one can analyze results from EELS (electron energy loss spectroscopy) [69, 70] or inelastic X-ray scattering [71] experiments. Theoretical approaches include linear response time-dependent density functional theory (TDDFT) [72, 73]. In this work, we use a method derived from dielectric theory.

The dielectric function at zero momentum transfer is taken from optical data

[65, 74] that measure the refractive and absorption indices, n and κ :

$$\varepsilon(q=0, \Delta E) = (n + i\kappa)^2. \quad (2.20)$$

We extrapolate this data into the q - ΔE -plane assuming that each feature of the spectrum behaves as a plasmon pole of a free electron gas [67, 75, 76]. One finds for the inverse imaginary part of $\varepsilon(q, \Delta E)$ (“loss function”, see fig. 2.8) entering eq. 2.19 [66]

$$\text{Im} \left\{ \frac{-1}{\varepsilon(q, \Delta E)} \right\} = \frac{\Delta E_0}{\Delta E} \text{Im} \left\{ \frac{-1}{\varepsilon(q=0, \Delta E_0)} \right\}, \quad (2.21)$$

$$\Delta E_0 = \Delta E - \frac{q^2}{2}. \quad (2.22)$$

In this work, we assume that this model is also a valid approximation for insulators [1, 63]. At least, the model gives a dielectric function that obeys the Thomas-Reiche-Kuhn sum rule [67] which links the dielectric function to the electron density of the medium.

2.3.2.3 Analysis of mean free paths; energy diffusion to the lattice

Fig. 2.8 shows the optical data $\text{Im} \left\{ \frac{-1}{\varepsilon(q=0, \Delta E)} \right\}$ of CaF_2 and the elastic and inelastic mean free paths for electrons of different energies in CaF_2 . The loss function (left panel) is proportional to the probability that a photon with energy ΔE is absorbed [77]. The gap energy of $E_{\text{gap}} = 11.7$ eV is clearly visible. Below this energy, only (optical) phonons can be excited ($E_{\text{phonon}} \approx 0.058$ eV). For photon energies between 0.1 and 10 eV the crystal is transparent. The oscillations directly above the gap energy can be attributed to excitonic states (localized electron-hole pairs). The first large peak (below 25 eV) stems from the F(2p) valence band (average binding

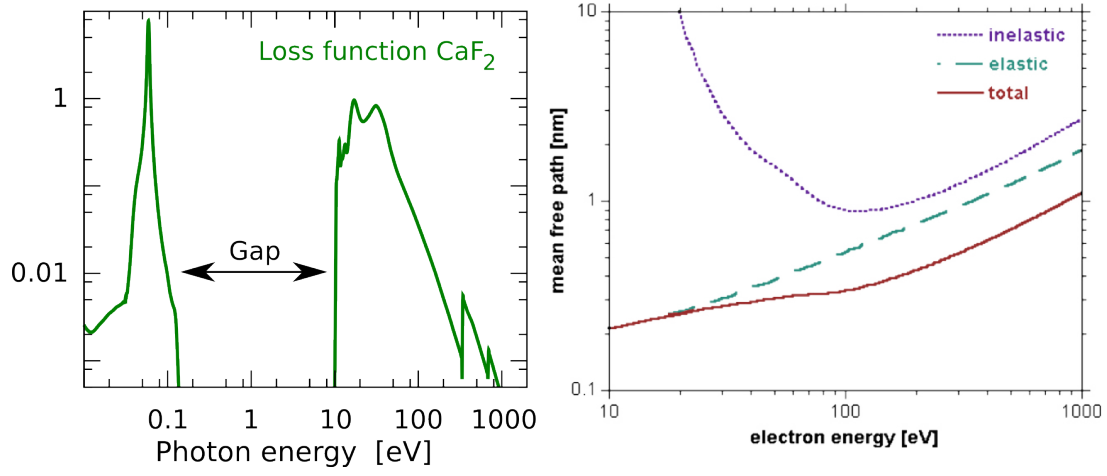


Figure 2.8: Left panel: Loss function $\text{Im} \left\{ \frac{1}{\varepsilon(q=0, \Delta E)} \right\}$ of CaF_2 . The gap energy is 11.7 eV (the left peak represents optical phonons). Right panel: Energy dependent magnitude of the elastic and inelastic mean free paths. The inelastic mean free path diverges as the energy approaches the gap energy (energy measured from top of valence band). Data for left figure from [65, 74]; right figure taken from [1].

energy 14.4 eV, width about 5 eV [45]). The structure at 30-40 eV is attributed to the lower lying orbitals, Ca(3p) (31.5 eV) and F(2s) (35 eV). Barely visible in the plot is the shoulder in the spectrum at the energy of the Ca(3s) orbital (50 eV). The sharp edges at higher energies indicate characteristic transitions from core orbitals (Ca(2p) and Ca(2s) at ~ 400 eV, F(1s) 700 eV, not shown is Ca(1s) at 4 keV [32]).

The right panel shows the elastic and inelastic mean free paths for electrons in CaF_2 . The electron energy is measured from the top of the valence band which is separated by $E_{\text{gap}} = 11.7$ eV from the bottom of the conduction band. The same applies to all electron energies in this section, unless otherwise noted.

It is important to realize that for an inelastic scattering event to take place, the incident electron must have an energy larger than $2E_{\text{gap}}$, because the final states of both electrons must be allowed and unoccupied (in an insulator, we expect all valence states to be occupied and all conduction states to be unoccupied). Therefore,

the *inelastic* mean free path diverges at that energy. In contrast, the *total* mean free path is almost an order of magnitude lower at low energies (10 eV) than at high energies (1000 eV) due to the short *elastic* mean free path. Thus, low-energy electrons will remain close to their initial spatial position, while electrons of elevated energy will quickly diffuse away and deposit their energy far from their point of emission. This will be discussed more quantitatively in section 2.3.3.2.

The above reasoning shows that for electron energies E smaller than $2E_{gap}$, the only remaining inelastic process is phonon excitation. In this process, the energy loss is very small, $\Delta E \approx E_{phonon} \ll E$; as a first estimate, we use the elastic cross sections for its angular dependence. We can therefore model phonon excitation in terms of a (to be determined) average (effective) number of phonons N_{phonon} which are created in each quasi-elastic scattering process, each of which reduces the energy of the electron by E_{phonon} . N_{phonon} therefore gives the energy loss dE per unit path length dx of low-energy electrons, for which no other loss mechanism is available, as

$$\frac{dE}{dx} = -\frac{N_{phonon}E_{phonon}}{\lambda_{el}} \quad . \quad (2.23)$$

Therefore, N_{phonon} influences the length of the path s low-energy electrons travel inside the solid before they have lost their initial energy E_0

$$s \sim \frac{E_0}{N_{phonon}E_{phonon}} \lambda_{el} \quad , \quad (2.24)$$

so that larger N_{phonon} (stronger coupling to the phononic system) leads to deposition of thermal energy nearer to the initial position of the electron and vice versa. N_{phonon} is energy dependent and has to be determined from the theory of electron-

phonon interaction. For our proof-of-principle study, we use a simpler approach.

Low-energy electrons ($E < E_{gap}$) are much more efficient in heating the part of the crystal close to the track axis, providing the main contribution to the energy necessary for track formation (compare section 2.3.3.2). We give an order-of-magnitude estimate for the coupling of low-energy electrons to the phononic system, N_{phonon} , based on data from scanning electron microscopy. Electrons of larger energy are assumed to have the same coupling.

Estimate of N_{phonon} Experimental data from scanning electron microscopy (SEM) can be used to estimate N_{phonon} . Secondary electrons (with energies ≤ 20 eV) produced by the primary beam can only escape from a relatively thin layer near the surface, and their intensity I is experimentally found to follow an exponential decay [78],

$$I \propto e^{-x/l} \quad (2.25)$$

with l the mean escape depth (attenuation length) and x the distance from the surface. For metals, $l \approx 10$ Å while for insulators, $l \approx 100$ Å [78]. Fig. 2.9 shows an energy spectrum of these low-energy electrons. Most of the electrons have energies smaller than the gap energy E_{gap} and thus cannot create secondary electrons. Therefore, they are slowed down mainly by electron-phonon interaction and we can relate the observed l to our parameter N_{phonon} .

The relationship between the microscopic parameter N_{phonon} and the macroscopic observable l is established empirically by comparing results from the electron transport simulation to experimental observations. We ran electron transport simulations for initial energy distributions as in fig. 2.9. The simulations differ only in the

choice of N_{phonon} . Fig. 2.10 shows the relative intensity (number of electrons) in a distance x from their point of origin.

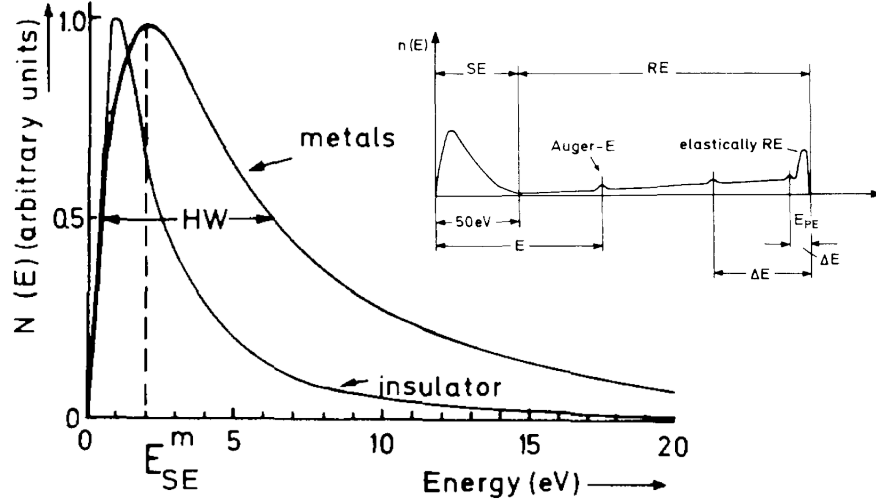


Figure 2.9: Secondary electron ($E \leq 20$ eV) spectra from scanning electron microscopy (large) and complete electron spectrum up to the primary beam energy E_{PE} (inset), including Auger and backscattered primary electrons. Figures taken from [78]. The electron energy is counted from the vacuum level.

The choice of N_{phonon} influences the slowing down of the electrons as expected. For larger N_{phonon} (stronger coupling), electrons lose their energy more rapidly and their intensity decays faster, and vice versa.

Along with the intensities, exponentials of several decay constants are plotted in fig. 2.10 that indicate that the intensity is asymptotically well described by an exponential (experimental behavior from eq. 2.25). From a comparison of the two, we find that a choice of $N_{phonon} \lesssim 0.1$ yields best agreement with the experimental value of $l \approx 100$ Å from [78].

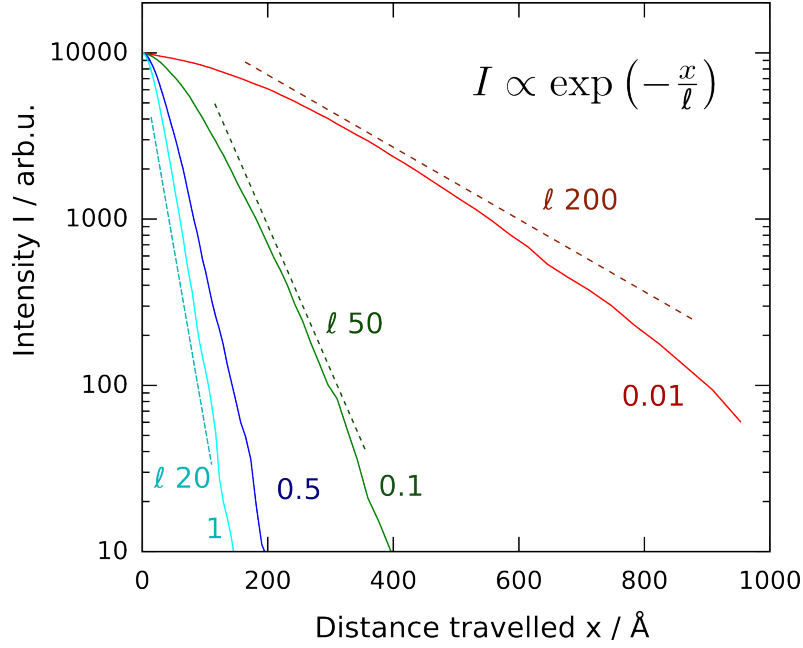


Figure 2.10: Intensity of low-energy electrons with an energy distribution as in Fig. 2.9 in distance x from their point of origin inside the solid (solid lines). Depending on N_{phonon} (0.01...1), the attenuation length l varies between 20 and 200 Å (dashed lines).

2.3.3 Results

10^4 electron trajectories sampling each initial condition (projectile energy E_p) derived from section 2.2 (see fig. 2.5) were calculated. Their initial conditions correspond to ion energies E_p of 0.226, 0.609, 2.3, 7.7, and 26 MeV/amu and equilibrium charges Z_p of 16, 23, 34, 44, and 52, respectively (c.f. fig. A.3). This is the energy range in which the stopping power is above the threshold for track formation.

Radial energy density distributions are calculated from the sum of phonon energies $\langle E \rangle(R)$ excited in a cylindrical shell of thickness ΔR in distance R from the track axis containing $N_{atom} = 2\pi R \Delta R \Delta z \cdot n_{CaF_2}$ atoms. n_{CaF_2} is the number density of atoms in CaF_2 , see eq. D.1. $\Delta z = N_{traj} \lambda_{ion}$, the height of the cylinder, is given by the number of calculated electron trajectories times the ionization

mean free path derived in section 2.2. The average energy density is then given by $\rho_E(R) = \frac{\langle E \rangle(R)}{N_{atom}}$. For the subsequent molecular dynamics simulation, a “temperature distribution” $T(R)$ is derived from the energy density $\rho_E(R)$. Each atom in the crystal has three translational degrees of freedom plus three (approximately harmonic) vibrational degrees of freedom. The energy is distributed according to the equipartition theorem,

$$\begin{aligned}\langle E \rangle(R) &= \frac{6}{2} N_{atom} k_B T(R) \quad \rightarrow \\ T(R) &= \frac{1}{3k_B} \rho_E(R)\end{aligned}\tag{2.26}$$

For T in K and ρ_E in eV/atom, the proportionality factor is $T \approx 3900\rho_E$.

2.3.3.1 Effect of N_{phonon} on energy distribution

We assess the importance of the parameter N_{phonon} by varying it around its estimated order-of-magnitude, $N_{phonon} \lesssim 0.1$ (see above) for a test case that corresponds to the maximum of the stopping power graph, $E_p = 2.3$ MeV/amu. Fig. 2.11 shows the resulting radial energy distributions for different N_{phonon} together with the energy density necessary for melting (minus the energy density corresponding to room temperature $E_{room} = 0.078$ eV/atom ; $E_{melt} = 0.55$ eV/atom [79]).

As expected, the distribution depends on the choice of N_{phonon} . For small N_{phonon} more elastic scattering events are required in order to deposit the energy. This, in turn, leads to a longer trajectory length of the random walk of the electron and, consequently, to a smaller energy density. Therefore, the energy density falls off steeper for large N_{phonon} than for low N_{phonon} .

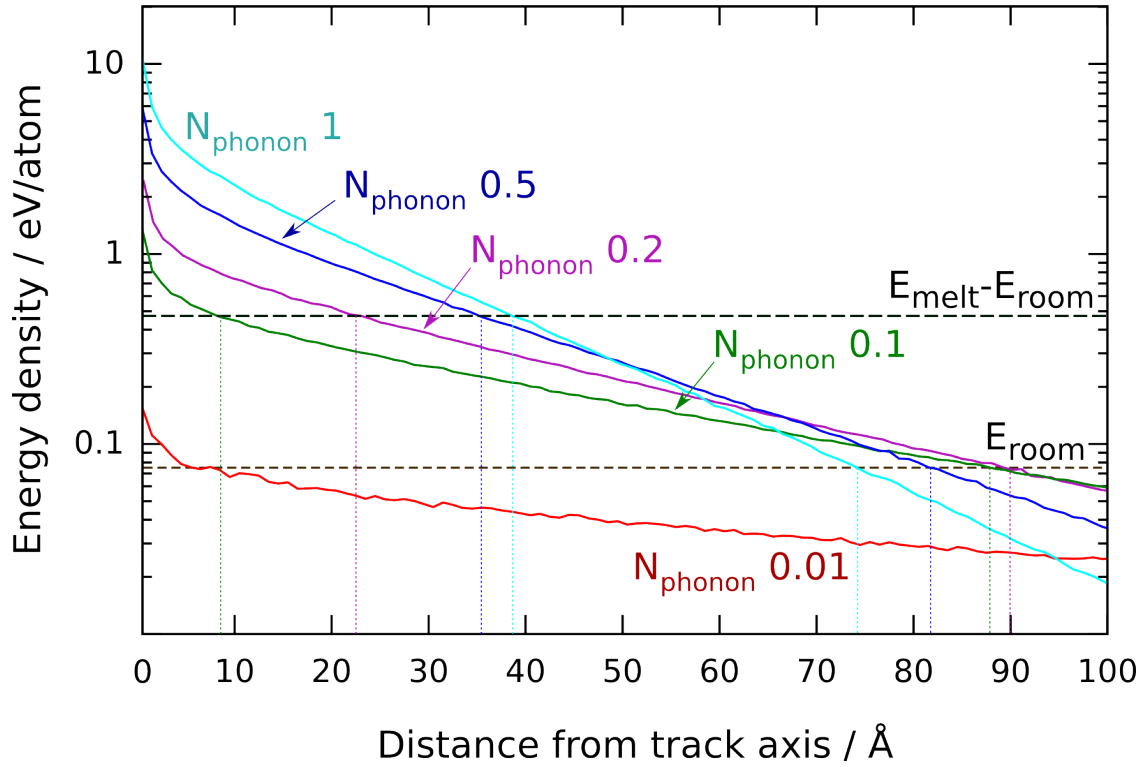


Figure 2.11: Radial energy distributions in the lattice of CaF_2 after the passage of a Xe ion of 2.3 MeV/amu. The distribution depends on the choice of the parameter N_{phonon} . For comparison, the energy density necessary for melting $E_{\text{melt}} - E_{\text{room}}$ and the energy density corresponding to room temperature (300 K) E_{room} are shown as horizontal lines. Vertical dotted lines indicate the distance from the track axis where the energy density crosses $E_{\text{melt}} - E_{\text{room}}$ or E_{room} . The integrals over each distribution (total energy) are almost equal (except for energy which is lost due to increased secondary electron production).

Bounds for track diameters based on energy density distributions

In a simple model, one could expect that the region where the energy is higher than the melting energy will melt and constitute the future “track” while the rest of the crystal will remain stable. Of course, one has to take into account the interplay between the excess heat in the central region and cooling by the rest of the crystal which will shift the border between the molten and crystalline region outwards. Still, the size of the region where the energy density for melting is reached is a

lower bound of the diameter of the future track. Similarly, an upper bound for the diameter of the track is given by the size of the region whose temperature is only negligibly influenced by the electron cascade. We estimate that this is the case if the additional energy density deposited by the electron cascade is lower than the energy density at room temperature, E_{room} .

The crossing points of the energy density distributions with the horizontal lines that indicate $E_{melt} - E_{room}$ and E_{room} are shown as dotted lines in fig. 2.11. For $N_{phonon} = 0.01$, the melting energy density is not even reached on the ion path itself, indicating that this choice of N_{phonon} is too low. The other choices which are shown in fig. 2.11 give lower bounds for the track radius of $\sim 10 - 40$ Å and upper bounds $80 - 90$ Å. This compares well to the experimental track radius of $50 - 70$ Å, independent of the exact value of N_{phonon} which is varied between 0.1 and 1.

We find best agreement with experimental results for $N_{phonon} = 0.2$. All further results are calculated using this value for the electron-phonon coupling.

2.3.3.2 Dependence of energy distributions on the initial electron energy

It is instructive to visualize the dependence of the heating efficiency on the energy of the primary electron. Figure 2.12 shows the average thermal energy distribution produced by one electron of primary energy 1, 10, 100, and 1000 eV, including heat generated by secondary electrons. Note that the fraction of high-energy electrons is by orders of magnitude lower than low-energy electrons for the initial conditions derived in section 2.2, see fig. 2.5.

Fig. 2.12 shows that low-energy electrons contribute disproportionately much to the heating of the central cylinder. This is due to two reasons: first, they stay closer

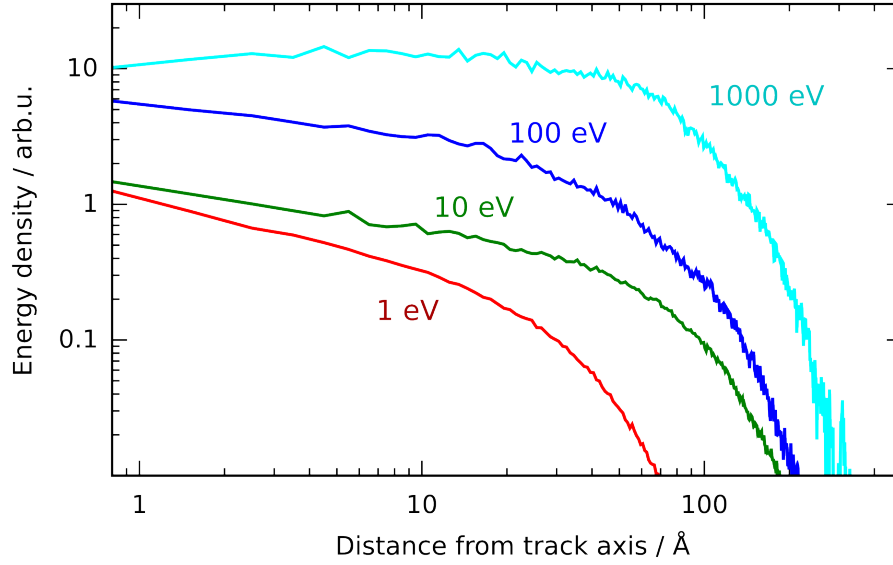


Figure 2.12: Radial thermal energy distributions per electron following the ejection of an electron with different kinetic energies as indicated, including heat deposited by secondary electrons.

to the track due to their lower mean free path and deposit their energy there rather than further away. Second, a larger fraction of their energy is converted to phonons while no energy is spent for secondary electrons. An electron of primary energy $E = 1$ or 10 eV deposits 100 % of its energy as phonons because no secondary electrons can be created. Once secondary electron creation is possible ($E > E_{gap} \approx 12$ eV), it is the main energy consumption mechanism. An electron of $E = 50$ eV (not shown in the graph) already deposits 75 % of its initial energy as secondary electrons and only 25 % remain for lattice heating. This fraction stays roughly constant for more energetic electrons; an electron of 1000 eV, for example, creates ~ 14.5 secondary electrons of average energy ~ 60 eV which in turn create ~ 50 more secondary electrons. Altogether, $64.5 \cdot E_{gap} \approx 77\% \cdot E$ are lost due to secondary electron excitation, and only $\sim 23\%$ of the initial energy remain effective for heating.

2.3.3.3 Ion energy dependent radial energy distributions

Following the model presented in the preceding sections, we have calculated the radial energy density distributions in the lattice of the target after the passage of the ion. We have calculated distributions for ion energies of 0.226, 0.609, 2.3, 7.7, and 26 MeV/amu or equilibrium charges of 16, 23, 34, 44, and 52, respectively. In all of these cases, the stopping power $S(E_p)$ is larger than the threshold for track formation.

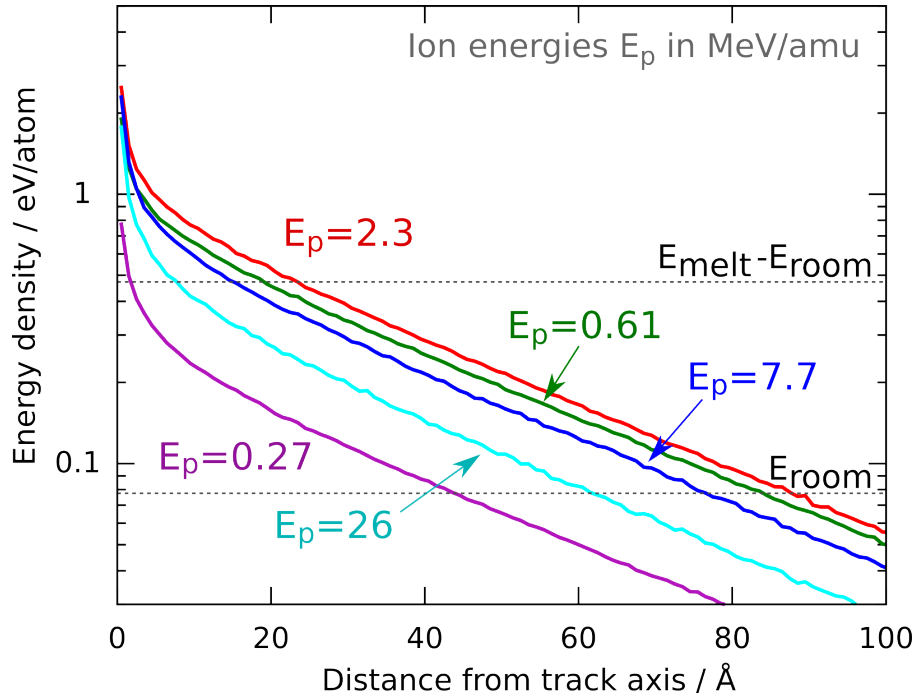


Figure 2.13: Radial energy densities in the target lattice after a passage of a Xe ion of indicated energy E_p (MeV/amu). Horizontal lines represent energy density for melting (reduced by room temperature) and room temperature as indicated.

In fig. 2.13 the calculated energy densities are plotted along with the melting energy density $E_{melt} - E_{room}$ and the energy density corresponding to room temperature E_{room} . The top graphs (2.3, 0.61 and 7.7 MeV/amu) correspond to points near the maximum of the stopping power while the bottom graphs (0.27 and 26

MeV/amu) are near the threshold for track formation (compare fig. A.3). As mentioned in section 2.2.3.1, the stopping power at the lowest ion velocity is underestimated, placing it at the threshold stopping power. As a result of this, the radius where the energy density is higher than E_{melt} is much smaller than for the other ion energies.

We give upper and lower bounds for track diameters following from these energy distributions by examining the crossing points of the energy distributions with E_{room} and $E_{melt} - E_{room}$ respectively, see section 2.3.3.1. Excluding the lowest velocity from the analysis, we find lower and upper bounds of $9 \dots 24 \text{ \AA} \lesssim R \lesssim 44 \dots 89 \text{ \AA}$, in accord with experimental results ($50 - 70 \text{ \AA}$).

Impact parameter dependence of the ionization process Electrons will not only be ionized near the track axis. Rather, the projectile will ionize electrons within a characteristic distance of $\lesssim 10 \text{ \AA}$ from the track axis (compare section 2.2). This will lead to a smearing of the radial distribution of the energy by about the same magnitude, increasing the lower bound of the track diameter. We study this effect by modifying the initial positions of the electrons. For simplicity, we chose a Gaussian $\propto \exp(-r^2/2d^2)$ with $d = 5 \text{ \AA}$ as the radial distribution function for the initial electron positions to qualitatively assess the importance of this effect. A more accurate approach could proceed along the following pathway: In [42], it is shown how the impact parameter dependence can be extracted using CDW-EIS. Calculations for each projectile energy, shell, electron ejection energy, and electron ejection angle have to be performed. This method is very time consuming and would require rewriting the CDW-EIS code.

Figure 2.14 shows the electron densities resulting from smeared initial electron positions. The only notable change is the flattening of the peak at small distances.

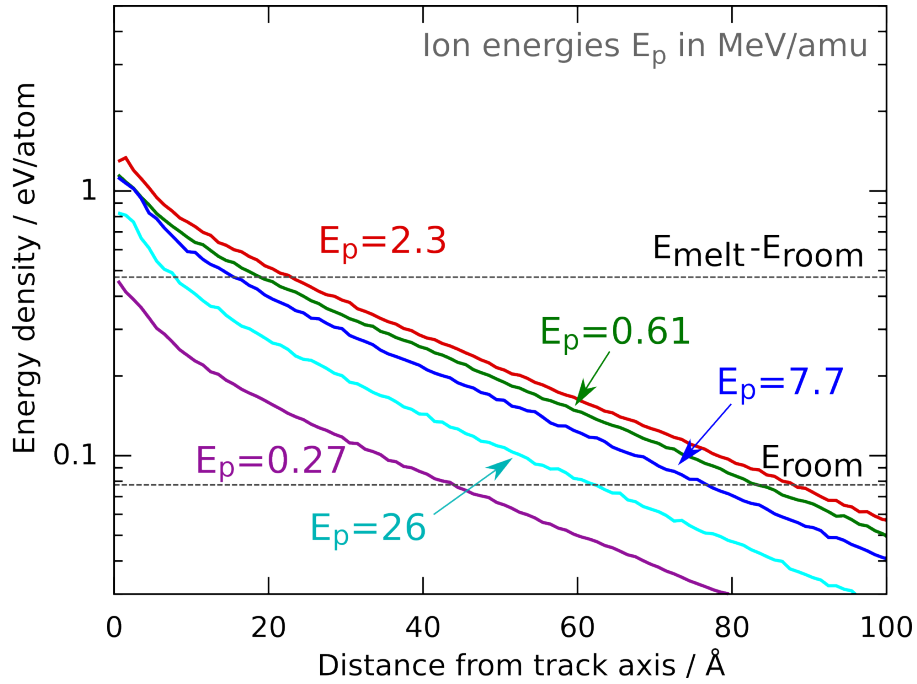


Figure 2.14: Radial energy densities in the target lattice after a passage of a Xe ion of indicated energy (in MeV/amu). Horizontal lines represent energy density for melting (reduced by the energy density corresponding to room temperature) and the energy density corresponding to room temperature as indicated. Initial electron positions are assumed to be Gauss-distributed with a root mean square deviation of $d = 5\text{\AA}$ around the track axis.

For the slowest projectile (0.27 MeV/amu) the distribution does not reach the melting temperature any more. As mentioned before, this may be related to the deficiencies of CDW-EIS at low velocities which leads in this case to a stopping power about 30 % smaller than predicted by SRIM. Increasing the ionization cross section to match the SRIM value leads to energy densities above $E_{\text{melt}} - E_{\text{room}}$ for radii below 8 Å. The stopping powers at other projectile energies are at least a factor of two above the threshold for track formation. The distributions are virtually unchanged above $R \approx 5\text{\AA}$.

We conclude that the energy distributions are largely insensitive to changes in the initial spatial distribution of the ionized electrons.

2.3.4 Conclusion

In this section, we have presented a model for electron transport and energy deposition to the lattice. In a CTMC simulation a large number of electrons is propagated starting from initial conditions derived from the ionization cross sections. Transport through a solid is described by a stochastic sequence of elastic and inelastic scattering events leading via secondary electron generation to a cascade. In quasi-elastic scattering events, phonons can be excited leading to heating of the lattice. We have presented energy distributions in the solid at the end of the electron cascade. Comparison to characteristic energy densities required for melting and at room temperature give lower and upper bounds for track diameters, which are consistent with experimental data.

2.4 Energy diffusion in the lattice and restructuring

Previous steps of our multi-scale model have left us with a crystal with an elevated temperature distribution which depends on the kinetic energy of the incident ion. As the final step we have to model the motion of the target atoms in response to their elevated kinetic energy density. We hope to find a signature of “tracks”, distinct regions (with smeared out border) inside the target where “damage” is visible, i.e. where the lattice structure is partially dissolved (increased disorder).

Up to now, we have treated the target as a structureless medium with certain properties, i.e. lattice structure effects have been neglected. Now, we need to take the crystal structure into account. A summary of some lattice properties of CaF_2 is given in appendix D. As explained in section 2.1, the time scale of this next step of the simulation is much larger than the time scales of the previous steps, which is why we assume the ionization and electron cascade processes to be finished and use their output as input for the Molecular Dynamics (MD) simulation. Other processes which happen due to the electron cascade and might not be finished at this time (e.g. recombination of electrons and holes, self-trapped excitons, color centers, or residual charges) are neglected in our model.

As the relevant time scale ($\gtrsim 1$ ps) is much longer than the orbital period of a target electron (0.3 fs for a F2p electron, the slowest in our material), we can neglect the motion of the electrons. Using effective potentials we can treat the crystal by a molecular dynamics (MD) simulation.

Molecular dynamics is an important tool of modern computational physics. It has been successfully applied to model situations similar to ours, e.g. sputtering [80–84],

cluster bombardment [85], laser ablation [86], and the calculation of transport coefficients [87–90]. It is the essential tool of the theoretical biologist [91–94] for the prediction of protein folding, transport of macromolecules through membranes, and much more.

The potentials are the key ingredient of any MD simulation. For our proof-of-principle study, we use the most basic approach, two-body potentials. Depending on the nature of the material, refinements to this approximation can be made. The use of many-body potentials allows one to take into account the effective electron density that mediates the binding in materials consisting of neutral atoms [85] while for hydrocarbons, reactive empirical bond order potentials [80, 81, 95] have proven successful. For ionic materials like CaF_2 , taking into account the polarizability of the atoms can improve agreement to experiment [87, 88] but comes at the expense of computing and man-power not available for this work.

A major concern of modern MD simulations is efficient implementation as the size of the system which can be modeled is limited by the computer power available. Efficiency is increased using parallelization, the extreme case of which is perhaps Folding@home (<http://folding.stanford.edu/>) from Stanford (example result [96]). They calculate large-scale problems using cloud computing to split the work among around 350000 volunteering home pc's, graphic cards, and Sony Play Stations, amounting to 7.3 x86 PFLOPS (09/7/19) which makes it currently the world's largest computing power. It is fuelled to a large part by graphic cards and game consoles because of their inherently parallel nature and their ability to compute trigonometric functions and exponentials about 10 times faster than CPUs. Of course, very specific code has to be developed to use this power. Another interesting project in this respect is HOOMD (Highly Optimized Object-oriented

Molecular Dynamics) [97, 98], a general-purpose MD implementation which is designed to run on a graphic card, boasting speedups up to a factor of 30 compared to CPU-based implementations. It uses NVIDIA®’s CUDA (Compute Unified Device Architecture) [99] which provides convenient access to low-level functions of graphic cards as a cost-effective way to treat numerically intensive problems.

In contrast to these highly optimized implementations, the code we use was originally developed by G. Betz (example result [85]) for sputtering simulations of metals and modified for our purposes. It is not parallelized and is mostly run on a desktop PC, which sets serious limitations on the system size which can be treated within realistic times.

2.4.1 Overview of Molecular Dynamics (MD)

MD propagates an ensemble of N atoms (in our case $N \approx 10^4 - 10^5$) according to Newton’s equations of motion,

$$\vec{p}_i(t) = \vec{F}_i(t) , i = 1, 2, \dots, N . \quad (2.27)$$

The integration method is a core part of the code. One typically uses a symplectic integrator (e.g. from the Verlet family [100]), sacrificing the accuracy of individual trajectories in favour of better energy conservation properties. We use a similar algorithm [84, 101], but with an adaptive step size which is tuned to the fastest atoms in the ensemble. Integration time steps are $\sim 1 - 4$ fs.

The initial conditions at time $t = 0$, $x_i(t = 0)$, are chosen according to the equilibrium positions of the lattice (see appendix D). Since only a very small part of an actual crystal can be modelled (10^5 out of 10^{23}), periodic boundaries are used

to avoid edge effects. The key input to the simulation is the force $\vec{F}_i(t)$ which is applied to the i -th atom at time t . In addition to the physical forces of all other atoms exerted on the i -th atom through two-body-potentials, additional forces can account for external force fields, the influence of the rest of the crystal, or a heat bath.

2.4.1.1 Choice of physical forces

We start with a description of the calculation of physical forces between the atoms. CaF_2 is an ionic crystal, so the main part of the force is the Coulomb attraction or repulsion between the under-/over-shielded cores (Ca: 2+, F: 1−); the Coulomb force decays with $1/r^2$ with r the internuclear distance. Other effects can be accounted for by using additional terms with a different asymptotic behavior. We employ a so-called rigid-ion potential which has been successfully used to predict the thermal conductivity of CaF_2 at elevated temperatures and other properties [89]. The term “rigid-ion” refers to the lack of polarization effects where the shape and center of charge of the electron cloud is changed with respect to the initial configuration. Such an improvement is described in [102] but lies beyond the scope of this work. Here, we use a pair potential of the form

$$V_{ij}(r) = \frac{q_i q_j}{r} + A_{ij} e^{-r/\rho_{ij}} - \frac{C_{ij}}{r^6} \quad (2.28)$$

where the second term reflects short range repulsion due to overlapping electron clouds and the third term reflects induced dipole-dipole (van der Waals) interactions. The ions are assigned their nominal screened charges q_i ($q_F = -1$, $q_{Ca} = +2$). The coefficients in eq. 2.28 depend only on the types of the atoms i and j (i.e. Ca or F).

The force can be calculated from this potential according to

$$\vec{F}_{ij}(\vec{r}) = -\vec{\nabla}V_{ij}(r) \quad . \quad (2.29)$$

For each atom, the total force at each time step is computed as the sum of all forces exerted on the atom by all other atoms. However, it is more economical to cut off the force at some distance r_{cut} and assume contributions of atoms outside this distance to be negligible. This is the standard technique in simulations with only short-range forces. Due to the long-ranged Coulomb interactions in our simulation, the contribution of atoms outside r_{cut} is not small, and atoms diffusing in and out of r_{cut} lead to unrealistically strong variations in the force field which in turn break the crystal apart. We found that the best way to circumvent this problem is an advantageous choice of the cut-off radius r_{cut} combined with a softening of the cut-off by multiplying the force function with a Fermi-type function $f(r; r_0, \beta) = \frac{1}{1+\exp(\beta(r-r_0))}$. After analyzing many combinations of r_0 and β , we chose $r_0 = 4 \text{ \AA}$ and $\beta = 12 \text{ \AA}^{-1}$ which amounts to a soft cut-off over a range of around 1 \AA ,

$$\vec{F}_{ij,cut}(\vec{r}) = f(r; r_0, \beta) \vec{F}_{ij}(\vec{r}) \quad . \quad (2.30)$$

Since the dominant Coulomb forces decay with $1/r^2$ but the number of atoms in a spherical shell of thickness Δr in distance r from the test point increases with r^2 , it is a priori not clear that any kind of cut-off will model the interactions correctly. We will discuss below which properties of actual CaF_2 our model reproduces. Unfortunately, a better treatment of Coulomb forces would include major rewriting of the existing code, up to a complete redesign [103]. We must therefore assume that

our model at most qualitatively represents a real CaF_2 crystal.

2.4.1.2 Thermostat

In addition to the physical forces, other properties which one wishes to simulate can be included in the simulation by the application of additional “generalized” forces. The most important property for our simulation is the temperature.

An ensemble of atoms of temperature T is exponentially relaxed to a target temperature T_0 (where $\langle E \rangle = \frac{6}{2} N k_B T$) by [104]

$$\frac{dT}{dt} = \frac{T_0 - T}{\tau} \quad . \quad (2.31)$$

We estimate the order of magnitude of the time constant τ by calculating how long it takes a sound wave of velocity $v_{\text{sound}} \sim 3.8 \text{ km/s}$ [30] to pass a nearest-neighbor distance (2.5 \AA). The result is $\sim 70 \text{ fs}$. Eq. 2.31 is translated to a modification of the force, effectively rescaling the velocities of the particles. This method is called Berendsen thermostat [104] and is widely used for the sake of its efficiency. However, it suppresses temperature fluctuations and therefore does not represent a canonical ensemble correctly. Therefore we use it for equilibration only, as our main calculations will be non-equilibrium simulations where only two layers on each side of the crystal are coupled to the heat bath (see below).

2.4.1.3 Application of MD to track formation

In order to model the crystal dynamics after the electron cascade is finished, we first equilibrate the whole crystal to $T = 300 \text{ K}$ and then slowly heat up a cylindrical central region (see below) until a temperature distribution inside the crystal similar to the output of the electron transport simulation is reached. Time dependent MD is

then used to investigate the effects of this temperature distribution on a picosecond time scale. Fig. 2.15 illustrates the time dependent temperature of the hot central region, the rest of the crystal (heat bath), and the whole crystal for one particular case.

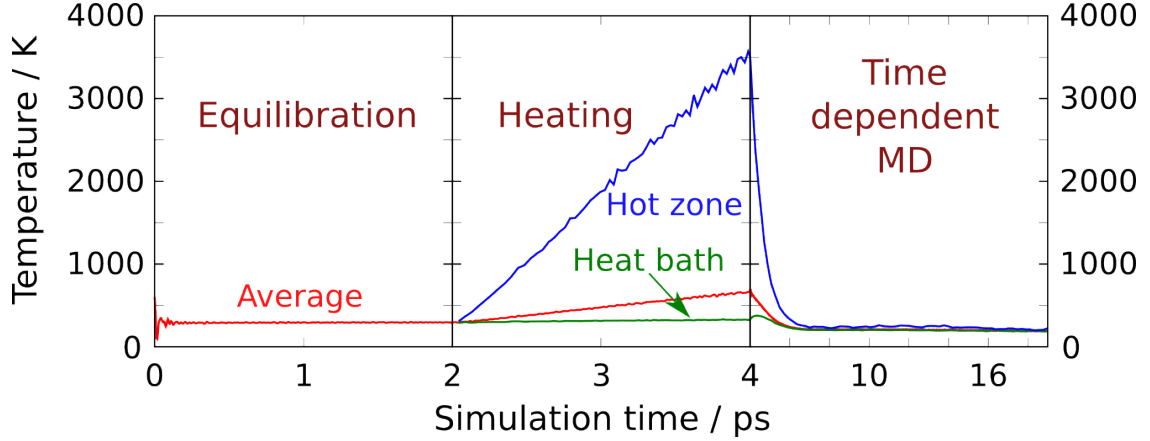


Figure 2.15: Time dependent average temperature of the whole crystal (red), the hot zone (blue) and the rest of the crystal (green) in the three phases of the simulation ($R=16$ Å, $T=4000$ K). Note the different time scale chosen for the last phase.

Equilibration All atoms in the lattice built from the initial conditions are given Gaussian velocities so that the energy density in total amounts to a temperature of $2 \cdot T_{bath}$. According to the equipartition theorem (supposing a roughly harmonical potential for the three vibrational degrees of freedom of each atom), this energy is subsequently shared equally among translational and harmonic degrees of freedom and gives the desired temperature T_{bath} . The simulation starts with an equilibration phase. The system is relaxed for typically 2 ps from its initial state to a thermalized state of temperature T_{bath} . During this phase, all atoms are coupled to the heat bath. We use $T_{bath} = 300$ K unless otherwise noted, which corresponds to a target at room temperature.

Heating of a central zone To obtain radial temperature distributions, a central cylinder of the crystal is heated by setting the target temperature T_0 of the Berendsen thermostat (c.f. eq. 2.31) to a value that linearly increases from the equilibration temperature of the first phase, T_{bath} , to a “hot” temperature, T_{hot} , if the atom is inside the “hot” region (distance to the track axis lower than R_{hot}). R_{hot} and T_{hot} will for now be treated as parameters; later, we will show how they can be related to the calculated kinetic energy density distributions from section 2.3. Atoms outside the hot region are thermalized to T_{bath} . Note that even though both regions are thermalized to different temperatures, one will not obtain a step function in the radial temperature distribution because the atoms in the “hot” zone can interact with the atoms from the “cold” zone and vice versa. This heat conduction mechanism leads to a smooth radial temperature (kinetic energy) distribution. However, it also leads to a central temperature which is somewhat higher than T_{hot} . Temperature distributions after this heating period are depicted in fig. 2.17 later in this section.

An important parameter for this step of the simulation is the heating duration, t_{heat} . The shorter it is, the better the step temperature distribution is reproduced, but the change induced in the material is more violent. From a physical point of view, t_{heat} should be of the order of magnitude of the duration of the electron cascade, 100 fs (see section 2.2). Unfortunately, such short heating times affect the long-time stabilities of the simulated lattice, which we ascribe to our treatment of long-range forces in our simulation. Furthermore, the creation of tracks depends sensitively upon t_{heat} if it is chosen so short. Therefore, we chose a much longer t_{heat} (> 1 ps). Then, the heated region reaches (dynamical) equilibrium during the heating process, and its exact duration does not influence the outcome of the

simulation. In this way, a “molten” phase (of the less stable F sub-lattice) is created, whose time development we can then observe. For the results presented here, we chose $t_{heat} = 2$ ps.

Time-dependent MD After heating up, the system evolves on its own, i.e. without coupling to heat baths. Only two layers on the side walls of our simulation box are coupled to an external heat bath with increasing coupling coefficient $1/\tau$, reflecting the influence of a crystal of 300 K temperature outside the box. The system is propagated in time until no further changes are observable. Long-time simulations have been performed to determine the stability of the cooled system. It was found that the state of the system did not change anymore after 15 ps.

2.4.2 Features and deficiencies of the simulation

Despite its simplicity, the model explained above can be used for our purposes. It succeeds in keeping the crystal stable at non-zero temperatures. When the temperature is raised, the F sub-lattice breaks at lower temperatures than the Ca lattice (“superionicity”, [89]), which stays always intact in our simulation at the temperatures we consider here. The short-range forces are reasonably well reproduced while the treatment of long-range interactions using a relatively sharp cut-off leads to long-time instabilities for short heating times (violent changes in the kinetic energy distribution).

An important macroscopic parameter that our simulation should be able to reproduce is the thermal diffusivity, which decides how fast heat is transported away from the track core. We find that our model reproduces the correct order of magnitude of the thermal diffusivity, see appendix F.

The many possible electronic excitations after the passing of the projectile (excitons, residual cores, color centers) are neglected in our simulation, as are charge transfer processes between target atoms despite the extreme temperatures in the central region of the track and the preceding electron cascade. The importance of such processes can be seen in fig. 2.16 which shows a bright-field TEM image of tracks in CaF_2 .

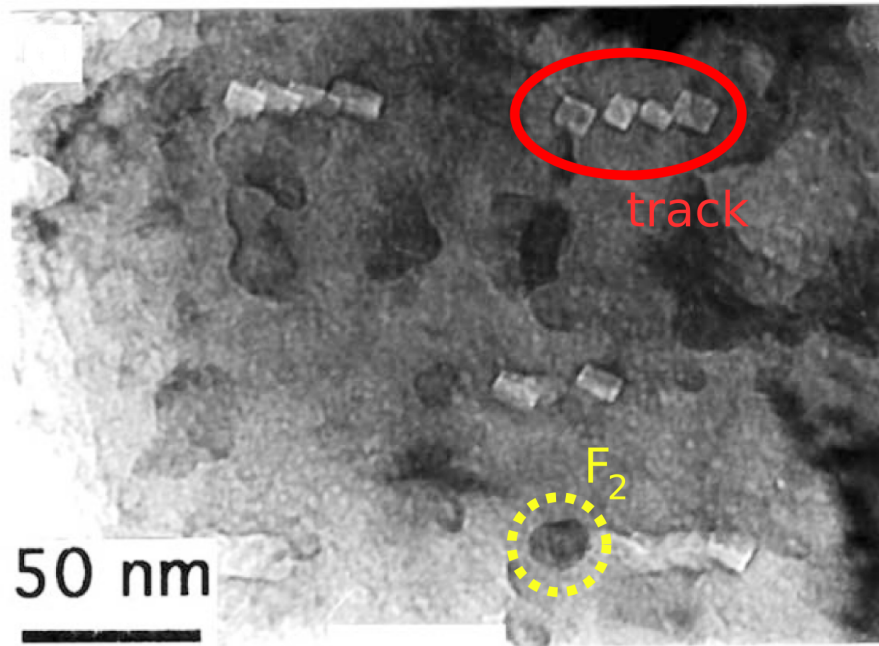


Figure 2.16: Bright-field 300 keV TEM image of 30 MeV C_{60} cluster ion latent tracks in CaF_2 , from [15, 105, 106]. Dark contrast loops of liberated fluorine gas (yellow dashed circle) are often seen at the end of heterogeneously nucleated individual tracks (red ellipse), which consist of intermittent 100 faceted calcium colloids along each track.

From cluster experiments, it is known that tracks in CaF_2 consist of F voids (aggregation of vacancies) and bubble-like defects [15, 105, 106], see fig. 2.16. The Ca sub-lattice stays unaltered by the formation of anion voids, which can be viewed as Ca inclusions in the CaF_2 lattice, with fully developed 100 faces (white rectangles in fig. 2.16). These inclusions can develop easily because the lattice constant of

CaF_2 is only $\sim 2\%$ off the lattice constant of Ca [15], minimizing the distortion of the surrounding CaF_2 lattice. The F_2 aggregates as interstitials, forming the bubble-like structures. This behavior can be linked to the chemical reaction $\text{CaF}_2 \rightarrow \text{Ca}^{2+} + \text{F}^- \rightarrow \text{Ca} + \text{F}_2$. Such a process, of course, heavily relies on charge transfer which is not included in our simulation. We restrict ourselves to modelling the track formation without charge transfer, interpreting disorder in the F sub-lattice as sign of a track.

2.4.3 Results

2.4.3.1 $R_{\text{hot}}\text{-}T_{\text{hot}}$ - ($R\text{-}T$ -) plane

We present a set of calculations that scan the $R\text{-}T$ -plane for track formation. The radius of the hot zone has been varied between 2 and 32 Å, and its average temperature has been varied between 500 and 6000 K. The system size was always around 15000 atoms, amounting to $84 \times 88 \times 30 \text{ Å}^3$. It was substantially increased for some test cases to around 120000 atoms, amounting to $180 \times 180 \times 60 \text{ Å}^3$, without any noticeable differences.

Figure 2.17 shows projections of the lattice at the end of the simulation for two parameter combinations, $\{R, T\} = \{16, 2000\}$ and $\{32, 4000\}$. In the former case, the lattice returns to its original position (except for one Ca interstitial, which to find is left as an exercise to the reader). In the second case, lattice disorder in the F sub-lattice remains after the cooling is completed. F ions leave their potential wells due to increased kinetic energy. While their temperature is high enough, they can move freely and transmit their thermal energy (by scattering) to larger distances from the track axis. Eventually, they cool down (become slower) and are trapped again, but now in *local* minima of the energy hyper-surface. Along with projections

of the lattice, fig. 2.17 shows the actual temperature distributions at the end of the heating phase.

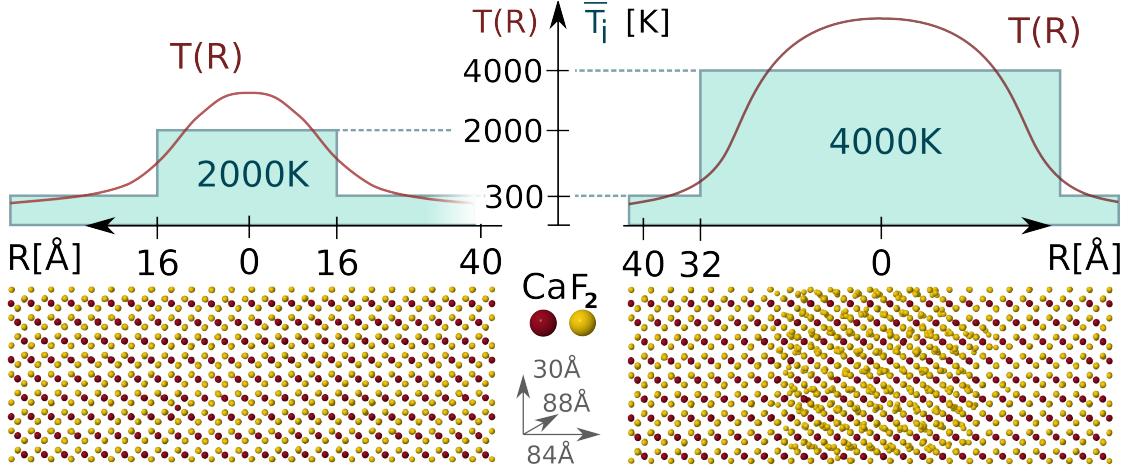


Figure 2.17: Above: Temperature distributions $T(R)$ and average temperatures T_{bath} , T_{hot} reached after heating; left: $T_{hot} = 2000\text{K}$, $R_{hot} = 16\text{\AA}$; right: $R_{hot} = 32\text{\AA}$, $T_{hot} = 4000\text{K}$. Below: Images from the time dependent molecular dynamics simulation several picoseconds later. In the first case, no lattice disorder is found, while in the second case a track of displaced F ions is clearly visible.

A quantitative measure of the amount of disorder induced by melting and restructuring is the pair correlation function $g(r)$ (sometimes also called “radial distribution function”). It measures the probability density to find an atom in distance r from another atom, see appendix E. Fig. 2.18 shows the pair correlation function for the crystal before heating, shortly after the heating phase, and at the end of a simulation which produced a track. In each case, the pair correlation function has been averaged over ~ 250 central atoms. For the undamaged system (blue graph), $g(r)$ shows sharp peaks at the different neighbor locations as expected. Shortly after the heating (red graph), the peaks are still visible but much less pronounced, indicating a liquid-like behavior. After cooling (green curve), most atoms return to places which form a lattice structure, but the peaks are much less pronounced,

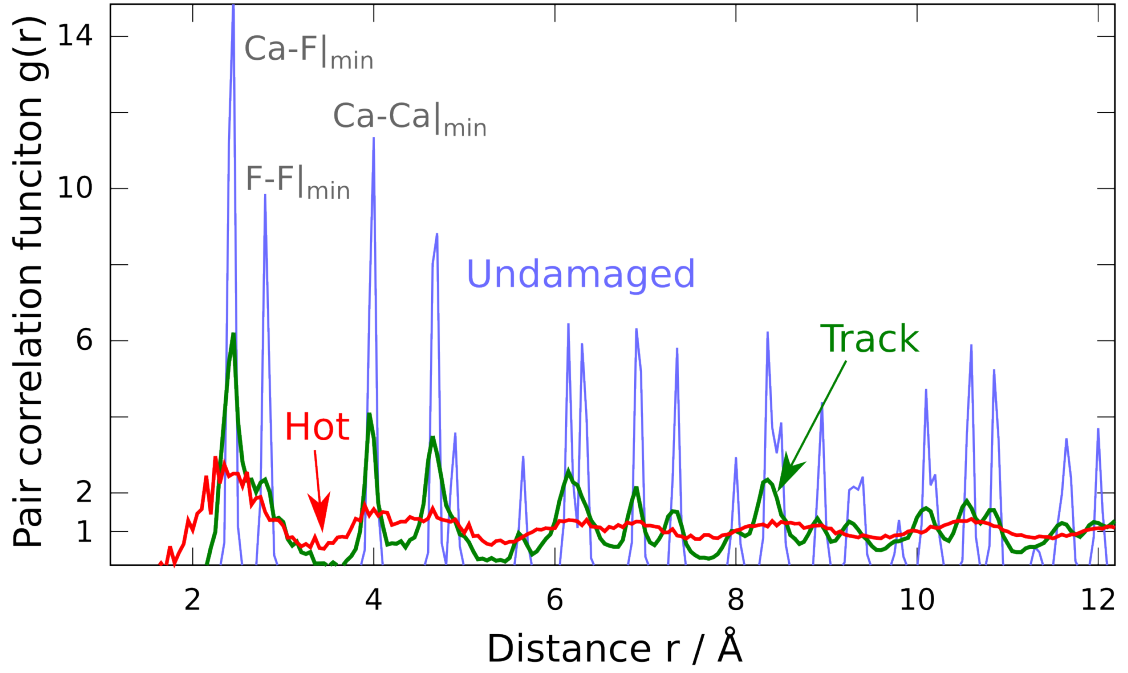


Figure 2.18: Pair correlation function for crystal before heating (same as undamaged crystal) (blue), hot crystal shortly after the heating phase (red), and cooled down crystal including damage (right panel in fig. 2.17). In the undamaged crystal, peaks at nearest-neighbor distances are visible (grey).

indicating defects. Most notably, the pronounced F-F peak is only visible as a shoulder, indicating that the F sub-lattice suffers more than the Ca sub-lattice.

Fig. 2.19 shows the R - T -plane with regions of (visually determined) track formation (green) and parameter pairs R and T that do not lead to restructuring (red). The transition region shows individual dislocations, but no clear signs of a track. Track formation sets in only above the melting temperature (1693 K), a validity test which our model passes.

The point to stress here is that there *is* a threshold, and that both the total deposited energy ($\propto R^2T$) and the kinetic energy density ($\propto T$) determine whether or not a track is formed. The threshold for track formation can neither arise from the ionization process nor from the electron cascade, because neither part

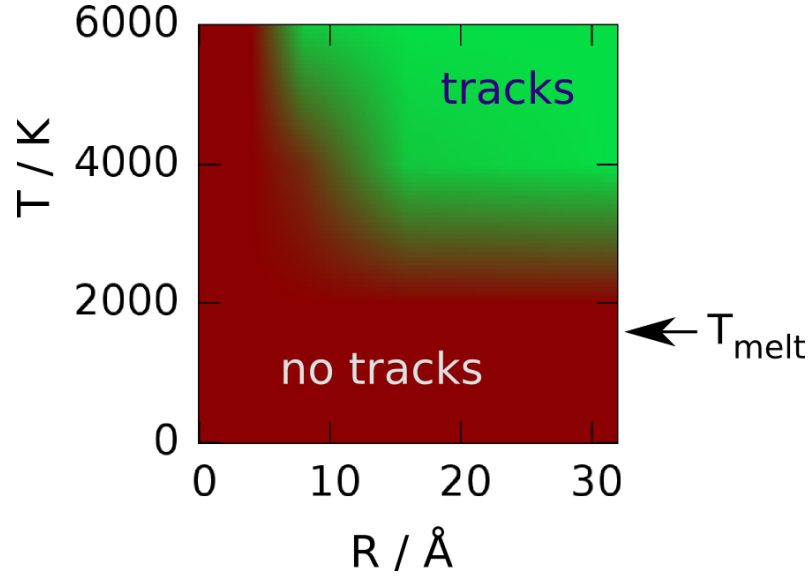


Figure 2.19: Sketch of track formation depending on the simulation parameters R and T . No tracks (red), tracks (green).

features a well-defined threshold. The estimation of the track diameter in section 2.3 was only done by comparing the radial temperature distributions to characteristic temperatures where macroscopic modifications of the crystal structure may happen.

Conclusion Our model, despite its simplicity, shows a clear threshold for track formation in the simulation parameters R and T , which correspond to the total energy and the energy density deposited in the target, in agreement to experiment.

2.4.3.2 Comparison to calculated temperature distributions

Finally, we establish a link between the temperature distributions calculated with the electron transport code in section 2.3 and the MD parameters. The energy density distributions (fig. 2.13) are analyzed in order to estimate R_{hot} and T_{hot} .

R_{hot} is calculated as the crossing point of the energy density distribution with the energy density that corresponds to melting temperature (eq. 2.26). T_{hot} is

calculated as the expectation value of the energy density for distances smaller than R_{hot} and again related to a temperature via eq. 2.26. Figure 2.20 shows the R - T -plane together with the R - T combinations that can be ascribed to ions of different energies (blue dots).

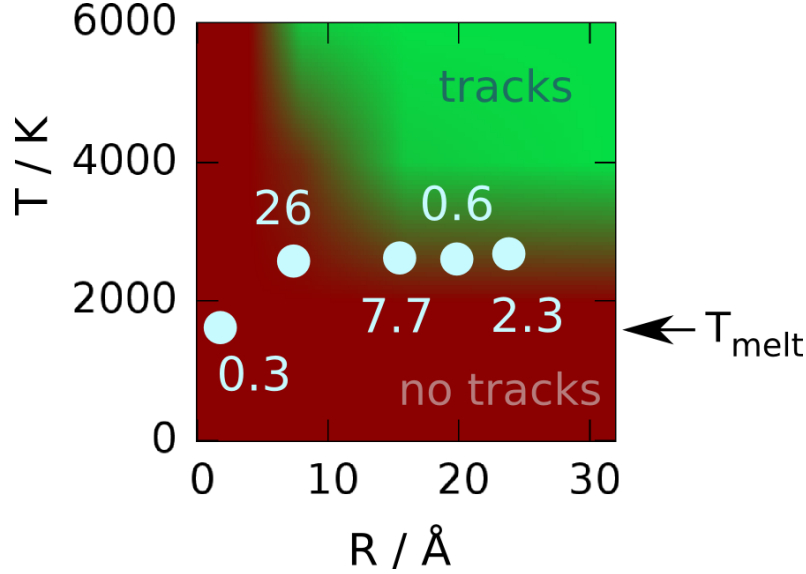


Figure 2.20: Map of track formation with $\{R, T\}$ combinations that correspond to ions of different energies (in MeV/amu) (see text).

Points from the border of the stopping power distribution (0.3 and 26 MeV/amu) are well outside the green region of the R - T -plane. For the low-velocity point this is also related to the underestimated stopping power (see above). All other points are at the border of the green region. The reason that they are not inside the green region might lie partly in the choice of the strength of the electron-phonon-interaction, see section 2.3, and the failures of the MD implementation (see above). Another reason, however, is the somewhat heuristic definition of the relation of temperature and energy density, see eq. 2.26. There, we assumed that a harmonic approximation for the crystal potential is adequate. While the approximation is sensible for low temperatures, it is only approximately true for higher temperatures

and near-liquid behavior. The experimental melting point of CaF_2 is given as $T = 1693$ K [89] or $\langle E \rangle / N = 0.55$ eV/atom [79]. Inserting into a linear relation between $\langle E \rangle$ and T , we find for the number of degrees of freedom f

$$\begin{aligned} \langle E \rangle &= \frac{f}{2} N k_B T \quad \rightarrow \\ f &\approx 7.5 \quad . \end{aligned} \tag{2.32}$$

This indicates that the temperatures estimated from the electron transport calculation might be up to ~ 25 % too low, moving the three rightmost points of fig. 2.20 towards the green region.

2.5 Conclusions and outlook

We have presented a microscopic model for track formation, covering 5 orders of magnitude in time. This is achieved by breaking the process down into 3 steps: the excitation of the electronic system of the target (0.1 fs), energy diffusion in the electronic system and energy deposition into the lattice (100 fs), and lattice dynamics (10 ps). These three steps are modeled using time-dependent perturbation theory, classical electron transport with phonon excitation, and molecular dynamics, respectively. We were able to calculate the electronic stopping power, energy distributions in the target lattice about 100 fs after the ion has passed, and restructuring of the target lattice. An energy threshold as found in experiment is only apparent in the final step of the model, the lattice dynamics. There, a minimum energy is required to overcome the restoring (cooling) forces of the target crystal. Results of individual steps closely resemble experimental data, the combination of all simulation steps is close to experimental findings.

Future improvements are expected to increase the agreement of model and experiment. In the electron transport part, electron-electron interactions between the simultaneously diffusing electrons and static Coulombic forces from the remaining cores near the track axis are not included, and a derivation of the electron-phonon interaction instead of a heuristic effective interaction would be more satisfactory. Furthermore, the dielectric function governing energy loss along the electron trajectory could be calculated from first principles instead of the extrapolation method used in this work. Our molecular dynamics simulation is the part that would benefit most from further work. The most effective tasks there would be parallelization, a model for charge transfer processes, and treatment of long-range forces. Improvements of the latter would likely also allow for a reduction of the heating time t_{heat}

thereby facilitating a more realistic simulation of the process.

It would be interesting to apply our model to different materials, for example other ionic crystals, synthetic materials like Mica, SiO_2 , or biological materials. A consistency check would be to apply it to a metal, where, so far, no tracks have been found. If these calculations also agree with experiment, our model could possibly gain predictive power to determine which projectile-target combination would lead to lasting target damage. This could have applications for the expected wear of materials exposed to swift heavy ions, e.g. in nuclear fusion reactors, for the damage done by swift heavy ions in biological materials (e.g. in space stations), or for the design of high-temperature superconductors in which tracks are used to pin magnetic flux lines.

3 Nano-hillock formation

3.1 Introduction

In recent years, there has been vivid interest in the interaction of highly charged ions with surfaces. This area of surface physics is of interest both to the theorist who seeks to understand the complex processes involved, and the application-oriented experimentalist because it holds the promise of controlled surface modification on the nanoscale.

CaF₂, for example, has a lattice constant of 5.46 Å, which is only ~0.5 % off the lattice constant of Si, 5.43 Å. It has been shown that thin, atomically flat Si films (1 nm) can be grown epitaxially on CaF₂ [107]. Therefore, applications include, e.g., nano-scale patterning of microelectronic devices.

This chapter is organized as follows: we will first give a quick review of the experimental evidence on nano-hillock formation and its physical implications. Then, a model for nano-hillock formation will be discussed, which bears interesting similarities to the track formation model we have discussed in the previous chapter. In earlier works [1, 108], excitation of the electronic system by an incoming highly charged ion and electron transfer as well as lattice heating have been modeled. In this work, we will take the simulation one step further and model the last step,

lattice dynamics, by molecular dynamics (MD). Finally, we will discuss the similarities of the mechanisms of track formation and hillock creation.

3.2 Experimental evidence - threshold behavior

Let us first review the existing experimental evidence for hillock creation. A brief summary can be found in [108], where the results discussed in this section are taken from unless otherwise noted.

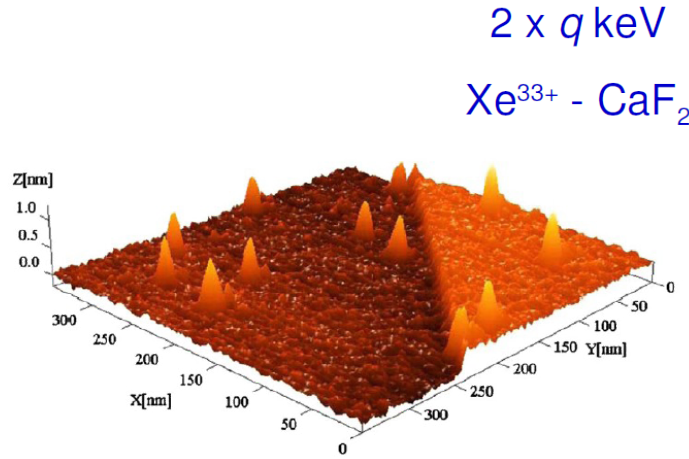


Figure 3.1: Topographic contact-mode AFM picture of a CaF_2 (111) surface irradiated with $2q$ keV Xe^{33+} ions. Hillock-like nanostructures protruding from the surface are observed. Note the different scales on the xy and z axes, from [108].

Figure 3.1 shows an AFM (atomic force microscope) topographic image of an atomically flat fluorine-terminated CaF_2 (111) surface after irradiation with highly charged ions (kinetic energy $2q$ keV Xe^{33+} , with q the charge state). One observes hillock-like nanostructures protruding from the surface. The hillocks are stable over macroscopic time scales in air and are not destroyed by the AFM measurement.

They are, on average, 200 Å wide and 8 Å high. Width measurements are subject to a large error bar due to the unknown structure of the AFM tip which has a finite width, comparable to the hillock diameter (≈ 100 Å). Furthermore, it can scratch off surface atoms/layers in contact mode, worsening the resolution. The errors from the latter effect are very difficult to assess experimentally. Height measurements, on the other hand, are less prone to systematic errors and are generally believed to be quite accurate.

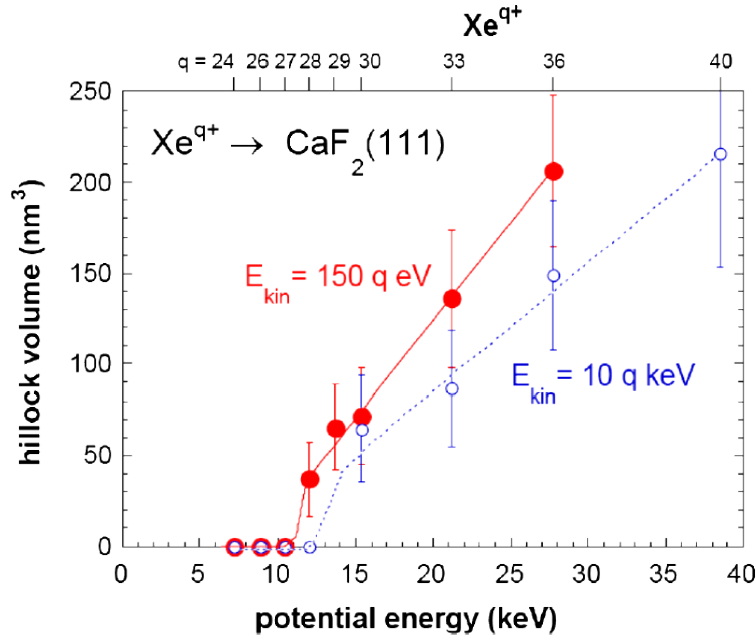


Figure 3.2: Mean volume of hillocks as a function of the potential energy of the HCl (corresponding charge state on top) for two different ion velocities. The error bars represent the statistical mean standard deviation of the ensemble of hillocks that were measured (not the uncertainty of a single measurement), from [108].

In the experiment, the incident ions have been slowed down to very low velocities (150q eV, corresponding to ~ 40 eV/amu), without notable changes of the surface modification. From a comparison of the number of hillocks per unit area to the beam fluence, one can conclude that at least $\sim 80\%$ of the incident ions produce a hillock.

Interestingly, a minimum charge state (potential energy) of the highly charged ion is required for hillock formation, almost independent of the kinetic energy of the projectile. Figure 3.2 shows this threshold in the volume of the hillocks for two different HCI velocities. These results suggest that hillock formation is mainly driven by the potential energy of the incident ion, in contrast to track formation that is driven by the kinetic energy. It is remarkable, however, that both processes feature a threshold in the energy that is deposited into the target: by slowing down of swift projectiles ($S(E_p)$) in the case of track formation or by conversion of the ionic potential energy (charge state) stored in the HCI in the case of nano-hillock formation.

Similar hillocks have been found [109] on the surface of insulators that have been irradiated with *swift heavy* ions. As described in the previous chapter on track formation, the onset of track formation is linked to a minimum stopping power. In tracks starting at the surface the material around the impact site is heated up by the same mechanisms described above, melts, and spills out. Upon cooling, it remains amorphous and forms hillock-like structures.

3.3 Energy deposition to the lattice

Basic mechanism From the experimental evidence, we have concluded that the mechanism for hillock formation should be similar to the one for track formation: The HCI is de-excited near the surface during a very short time span and deposits its potential energy in a small region near the point of impact into the electronic system of the target. The energy diffuses through the electronic system of the target by an electron cascade and is eventually deposited to the target lattice by electron-phonon coupling. Then, the lattice around the impact site starts to melt due to

the high kinetic energy density. Finally, material spills out forming structures that protrude out from the surface. As in the model for track formation, the threshold is related to the lattice dynamics, which leads to restructuring only above a threshold energy density that is sufficient for melting.

Time scales In order to model potential energy-driven hillock formation, it is important that the process can again be broken up in independent steps due to different time scales involved. To show this, we briefly estimate characteristic times for the different processes: First, the de-excitation of the slow highly charged ion (velocity around 1 Å/fs) will happen in the surface region. This complex process cannot be easily simplified. However, within the classical over-the-barrier model [110] and its extension to insulator targets [111], it is possible to estimate the time scale by the fastest Auger transitions, ≈ 5 fs. For the other steps, we can use the estimates from section 2.1, giving times of the order of 100 fs for the energy diffusion in the electronic system and 1 ps for the time scale of lattice dynamics. These estimates show that a step model is a good approximation to the process.

Review of theoretical results for the first two steps A quantitative implementation of the first two steps of this model has been given in [1, 108]. The de-excitation is modeled using the classical over-the-barrier model [110] and its extension to insulator targets [111, 112]. Additional information about the interaction of slow multiply charged ions with surfaces including a review of the experimental results in this field can be found in [29]. In short, target electrons are transferred into highly excited projectile states, from where they decay through different channels (collisional, radiative, Auger), which can be modeled using a system of coupled rate equations (classical over-the-barrier model). The emission of target

electrons leaves unbalanced holes, mainly F^0 atoms, in the surface, storing part of the potential energy. The interaction time above the surface is not long enough to complete the neutralization which eventually ends around $10 - 40 \text{ \AA}$ below the surface, depending on the initial kinetic energy of the ion. The electron spectrum emitted by the incident ion has a pronounced maximum at low energies while its detailed shape depends on the initial charge state of the projectile. For example, in the case of Ar^{18+} , core holes have to be filled, eventually leading to the emission of keV-electrons. The energetic electrons emitted in this neutralization process are then propagated inside the solid (electron cascade) using an electron transport code which is very similar to the one that we described in section 2.3, the only difference being the presence of a surface. The lattice is heated by electron-phonon interaction, which is the dominant process for low-energy electrons. As in the track case, high-energy electrons do not contribute much to the heating because their elastic mean free path is larger.

Fig. 3.3 shows the calculated energy distributions in the target after the energy has been deposited to the lattice for different ion charge states and kinetic energies. The shape of the heated region strongly depends on the kinetic energy of the incident ion. While it is flame-like for projectiles of higher kinetic energy, it becomes almost hemispherical for slow projectiles. However, it always features a hot “core” region (bright yellow) where the average energy density is higher than the energy needed for melting. The width of this core depends on the potential energy (charge state) of the incident ion. It has a typical diameter of 15 \AA . In the model for track formation, we were able to estimate a lower bound of the track diameter from the diameter of the region that was heated above melting temperature. In the hillock case, the observed hillocks are much larger than the volume of the hot zone, even

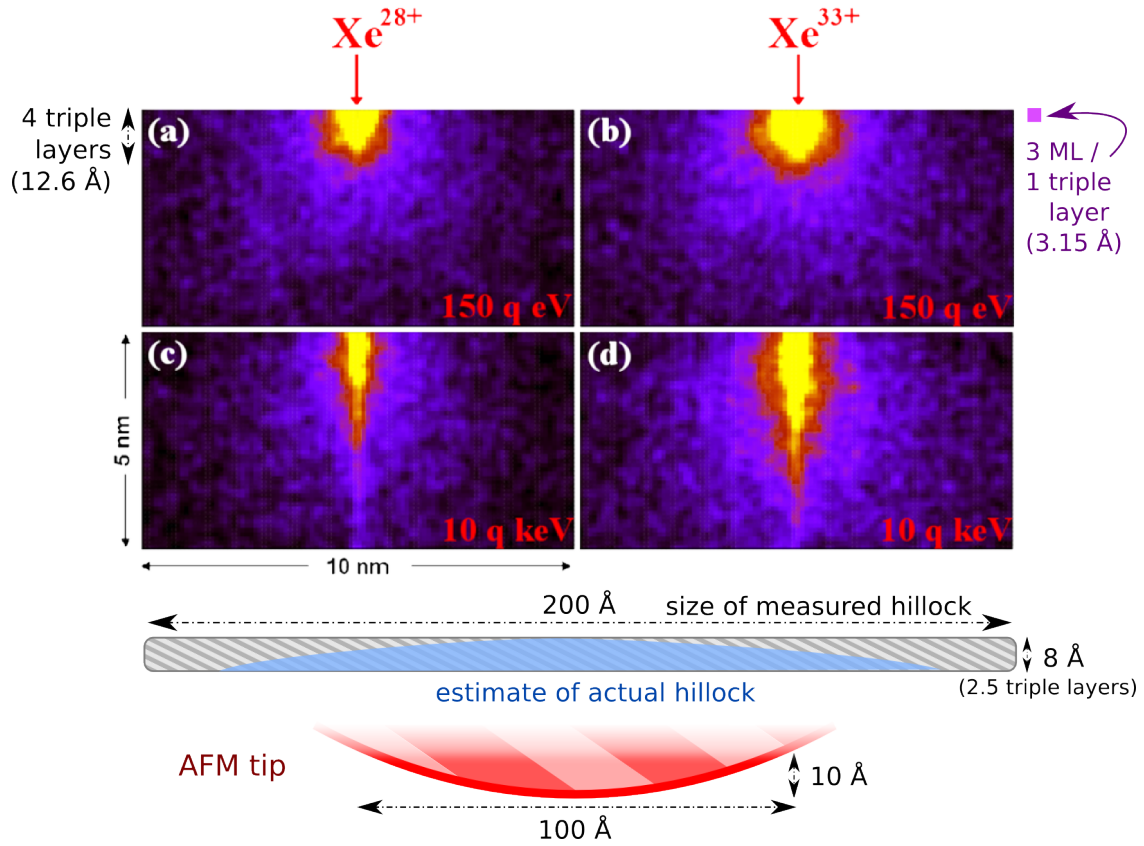


Figure 3.3: Top: calculated energy density distribution deposited by Xe ions of different kinetic and potential energy (charge state). C.f. fig. 3.2: (a,b,d) lead to hillock formation while (c) does not. Figure taken from [108]. Bottom: Sketches (to scale!) of the size of a hillock, the shape an actual hillock might have, and a typical AFM tip which is used to measure the hillock.

taking into account the width of the AFM tip (bottom of fig. 3.3). Therefore, an additional mechanism must be responsible for the measured size of the hillocks, especially if one takes into account that some of the atoms from the hot zone will be sputtered and material will be lost. Among the candidate processes for this increase in defect size are shock waves produced by the ion impact, surface diffusion, and preferential adsorption at the boundaries of a pre-hillock.

3.4 Energy diffusion in the lattice and restructuring

After the deposition of part of the potential energy of the incident ion to the target lattice, the atoms of the target start moving. As in the track case, we model the subsequent processes on a picosecond time scale with the help of a molecular dynamics simulation. We can adapt the simulation of track formation (details see section 2.4) to the hillock case by the following changes:

Presence of a surface The surface is modelled by keeping periodic boundary conditions in x and y directions (in the surface plane), but not in the z direction (perpendicular to the surface, c.f. fig. D.2). To model the influence of the semi-infinite crystal, we apply a restoring force to atoms of the deepest layer. The simulation box is extended into vacuum up to twice the simulated crystal thickness in $+z$ direction. Atoms which traverse the top boundary of the computing box are considered as sputtered and are no longer followed (which is computationally favorable as they often have high velocities which decrease the adaptive time step used in the trajectory integration).

Shape of the “hot” zone Instead of a hot central cylinder, we use a hot hemispherical region extending from the surface inwards, in agreement to the calculated energy distributions for slow ions (top row in fig. 3.3). The hot zone is characterized by its radius R and its average temperature T . We equilibrate the crystal for 2 ps, then the crystal is heated up over 5 ps. After this heating, we consider the initial conditions after the energy deposition to the lattice as reached. We follow the evolution of the system for 10 ps. This time is long enough to cool the system to a point where the surface structure remains stable.

3.4.1 Results

3.4.1.1 Snapshots

Before we scan the R - T -plane for hillock formation, we show some snapshots of the simulation in fig. 3.4 to give an impression of the quantitative results discussed in the following. As in the track case, the Ca sub-lattice (purple in right panel of fig. 3.4) remains stable while the disorder in the F sub-lattice (green) is much larger. The height of the hillock is around two or three triple layers, as in experiment, while its width is too small.

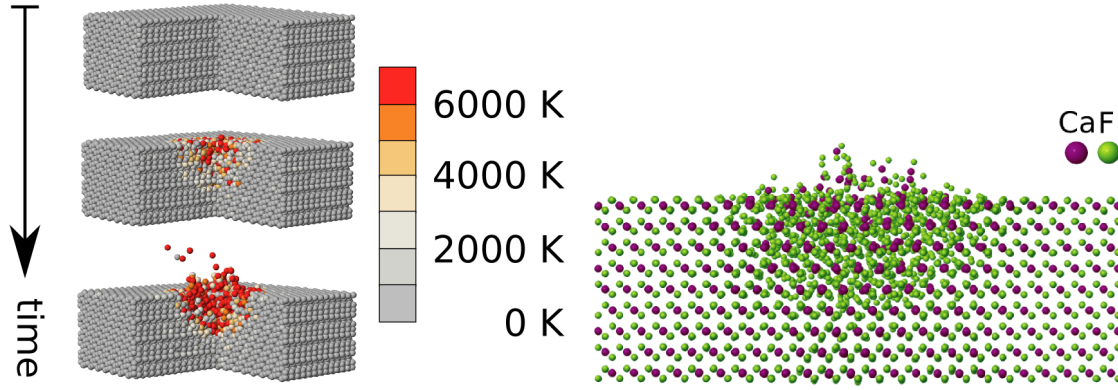


Figure 3.4: Snapshots of the simulation. Left, from top to bottom: Equilibration of the crystal (300 K), heating (to 5000 K, radius of hot hemisphere 26 Å), evolution of the system. The crystal is cut open for better visibility (not in the simulation). The colors indicate the kinetic energies of single atoms, converted to a “local temperature” via eq. 2.26 (see color code). Right: Projection of the crystal after propagation for 10 ps. Colors indicate type of atom (Ca, F). A hillock is observed. The size of the simulated system is $\sim 84 \times 88 \times 30 \text{ Å}^3$.

3.4.1.2 Threshold behavior

The experiments show a clear threshold for hillock formation. If our model is correct, we should be able to observe a threshold in the parameter space, R and

T . We performed a series of calculations for different values of R and T , and determined whether or not they lead to hillock formation by visual inspection. The result is the “map of hillocks” depicted in fig. 3.5.

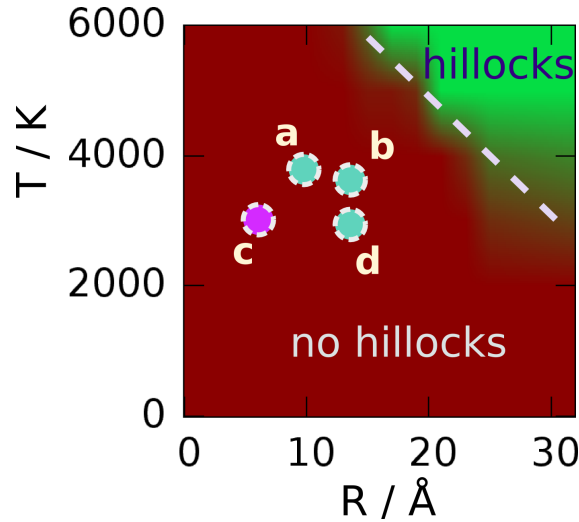


Figure 3.5: Hillock formation as a function of the simulation parameters R and T . Red indicates no hillock formation while green indicates the formation of hillocks. In the transition region (purple dashes), a visual inspection is inconclusive, and might have different outcomes for different runs of the simulation with the same parameters R and T .

The dots represent pairs $\{R, T\}$ obtained from the *simulated* energy density distributions (fig. 3.3). They correspond to projectile charge states and kinetic energies as follows: a ... Xe^{28+} with $150q$ eV kinetic energy, b ... Xe^{33+} $150q$ eV, c ... Xe^{28+} $10q$ keV, d ... Xe^{33+} $10q$ keV.

In *experiment*, hillock formation is found for projectile charge states and kinetic energies that correspond to a, b and d (turquoise dots) while no hillock formation is observed for c (purple dot).

We observe a clear threshold in the R - T -plane, similar to the track formation case (purple dashes). As expected, it is not only the total deposited energy but also the energy density that decides whether or not hillock formation occurs.

Note that the temperature necessary for hillock formation is higher than in the track case. That can be understood from the geometry. Heat transport in our model proceeds through interaction of atoms from the hot zone with atoms from the cold

zone. A larger surface area of the hot zone therefore facilitates the transport of thermal energy away from the hot region. On the other hand, the total thermal energy added to the system through heating is roughly proportional to the volume of the hot zone. In the track case (cylindrical hot zone of radius R), the ratio of surface over volume is $2/R$; in the hillock simulation (hemispherical hot zone), this ratio is $3/R$ so that heat conduction is enhanced compared to the track case. Therefore, higher temperatures T are necessary at the same R for restructuring.

The calculations of the thermal energy density produced by the electron cascade (section 3.3) predict radii of the hot zone $R \lesssim 15 \text{ \AA}$. In contrast, we do not observe surface restructuring for such low values of R . This is similar to the track simulation, where we found that track formation happens only somewhat above the experimental melting temperature, indicating that the simulated crystal is more heat-resistant than the real one. We ascribe this failure of the simulation to the lack of long-range interactions and charge transfer processes.

Fig. 3.5 also contains pairs of $\{R, T\}$ that we obtain from the simulated energy density distributions after the electron cascade (fig. 3.3). They were obtained as follows: T is the average temperature (plus room temperature) of the bright yellow region in fig. 3.3, where the energy density exceeds the melting temperature. The radius of the hot hemisphere is calculated by equating the volume of the hot zone to the volume of a hemisphere of radius R (in order to be able to compare the flame-like energy distributions to the near-hemispheric ones). The labelling is the same as in fig. 3.3.

As stated above, we do not observe hillock formation for any of the simulated energy density distributions $\{a-d\}$. However, the threshold region in the R - T -plane between $\{c\}$ (purple) and $\{a, b, d\}$ (turquoise) is relatively narrow, similar to

the one we observe in our simulation at higher values of R and T (purple dashes). Even their direction in the R - T -plane appears to be similar, which we view as a coincidence.

It is also interesting to compare the effect of the velocity of the impinging ion between the points $\{a,b\}$ and $\{c,d\}$ which correspond to slow and fast ions, respectively. In the latter case, the hot region is flame-shaped while it is hemispherical for slow ions. Not only the base diameter is larger in $\{a\}$ than in $\{c\}$, the average temperature of the hot region is also higher for slow ions, as the electrons deposit their energy closer to the point of impact.

3.4.1.3 Height and width of simulated hillocks

Fig. 3.6 shows a contour map of a typical crystal at the end of the simulation (after 10 ps), with parameters R and T chosen at the border of the green area of fig. 3.5 ($R = 26 \text{ \AA}$, $T = 5000 \text{ K}$).

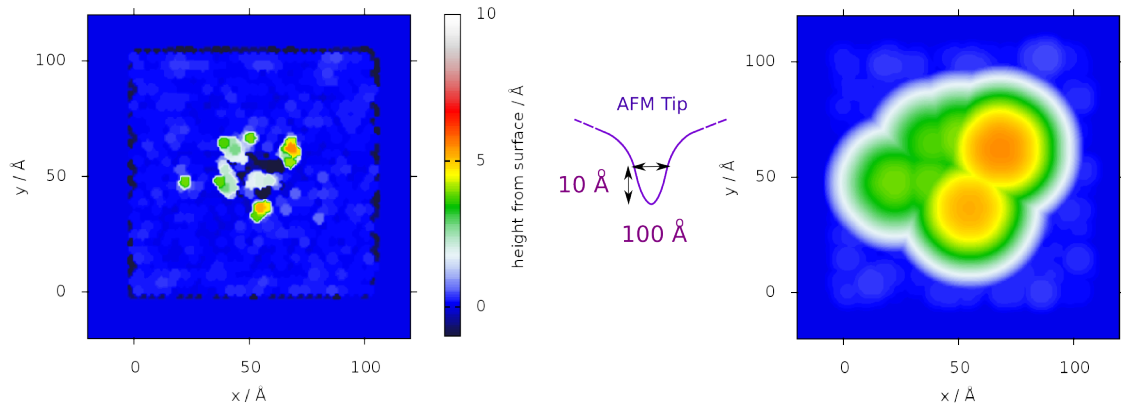


Figure 3.6: Left: Contour map of a hillock (from the same simulation as in fig. 3.4, left) (size of simulated crystal is visible as faint black border). Middle: Sketch of an AFM tip with which the contour map is broadened; right: Broadened contour map (same color code). Hillock diameter is around 100 \AA .

The figure sketches a possible method of deriving “experimental” AFM pictures

from the MD calculation. A contour map of the crystal is broadened geometrically by a virtual AFM tip of indicated shape and dimensions. The individual protrusions from the surface are smeared out to a hillock of ~ 100 Å in diameter (experimental diameter ~ 200 Å). We obtain heights that are in good agreement with the experimental value of about 8 Å, which suggests that hillocks are two or three triple layers high, c.f. fig. 3.3.

3.4.1.4 Target temperature dependence

We have tested the dependence of hillock formation on the target temperature which is a parameter that can be easily adjusted in experiment. Upon first glance, one would expect that an increased target temperature would shift the potential energy threshold for hillock formation downwards because the melting temperature of the material is reached more easily. On the other hand, heating the target restores the original lattice structure and heals surface defects because it increases the mobility of the atoms. Therefore, it is a priori not clear whether a heated/cooled target will show hillocks for different threshold charge states, or not at all.

We model target temperatures different from 300 K as follows: for a target which is heated/cooled to T_{target} , we set $T_{bath} = T_{target}$. To mimic the effect of the incident projectile, we put $T_{hot} = T_{hot}|_{300K} + (T_{bath} - 300 \text{ K})$ to make it comparable to the results from above. We ran tests for several combinations $\{R, T\}$ in the transition region, for heat bath temperatures T_{bath} ranging from 50 to 1200 K.

We find that the influence of the temperature at which the sample is kept is much smaller than the influence of the simulation parameters R and T . In general, results do not change for small variations of T_{bath} in the range 300 – 900 K, while both much higher or lower temperatures enhance the creation of hillocks ($T_{bath} \gtrsim 1200$ K

or $T_{bath} \lesssim 150$ K). Experimentally accessible effects are therefore only expected in temperature regions difficult to reach at the target surface (melting point 1693 K) or in the liquid nitrogen temperature range (77 K).

3.4.2 Conclusions and outlook

We have shown how the molecular dynamics simulation can be adapted for the simulation of hillock formation. We find a threshold for hillock formation in simulation parameters which correspond to the total energy and the energy density deposited in the target, consistent with experimental results. However, we do not observe hillock formation for simulation parameters extracted from earlier theoretical work. Still, the results presented in this section indicate that the experimentally observed threshold behavior has to be linked to lattice restructuring as in the case of track formation. The height of the simulated hillocks compares favourably to experiment while their width is around 50% too small. We attribute this discrepancy to AFM width measurements or an additional mechanism for the growth of hillocks, possibly on much larger time scales $\gg 10$ ps. Candidate processes include surface diffusion or additional lattice defects due to shock waves.

There is ample room for improvement of our simulation. The molecular dynamics simulation suffers from the same weaknesses as in the track case, see section 2.4. An analysis of the available literature shows that there is no undisputed method for the simulation of Coulomb forces and a surface at the same time, which nevertheless would be an indispensable ingredient for a more realistic simulation. Charge transfer processes might even be more important than in the track case, because it has been found that neutral F^0 atoms bind and leave the crystal as F_2 , leaving behind a Ca-enriched region where the hillock may form.

3.5 Comparison between track and hillock formation

In this work, we have investigated two substantially different processes which can be treated by very similar methods, and which both lead to structural modifications of the target. While the source of the energy (kinetic vs. potential energy of the projectile) and the primary energy transfer method (ionization vs. a complex de-excitation and neutralization cascade) are different, they both lead to energetic electrons in the conduction band of the target. In addition, they lead to quite similar electron energy spectra, with their maximum at low energies. These electrons are the most important source of heat as they do not diffuse very far, but deposit the larger part of their energy close to their initial position. In both cases, the energy is transferred from the electronic system to the lattice by electron-phonon interaction. The structural modification is achieved by melting and recrystallization on the nano scale.

While a different model is needed for the primary energy deposition to the target, we have shown that the same methods can be used to investigate the energy diffusion in the electronic system and the melting and recrystallization. This opens up the pathway to a wider spectrum of possible applications. A first candidate for future research will be laser ablation, where the electrons are created by photoexcitation. The interaction of photons with matter is well investigated and accessible to experiments (photoelectron spectra etc.). It should therefore be possible to derive realistic conditions for the state of the system after the primary energy transfer.

4 Summary and conclusions

We have presented a microscopic model for track formation by swift heavy ions in insulator targets. The model covers five orders of magnitude in time from primary energy deposition to restructuring. We have shown that the process can be described by three sub-processes which happen on different time scales, and proposed a microscopic model for each step.

During the first 0.1 fs, the energy transfer from the swift heavy ion to the electronic system of the target is described by time-dependent perturbation theory in a single active electron approximation (CDW-EIS). The validity of the approximation is confirmed by the reproduction of the stopping power to within 20-30% of its (semi-)experimental value over two orders of magnitude in the kinetic energy of the ion. The results are doubly differential ionization cross sections, which serve as initial conditions for the following step.

Within the next 100 fs, an electron cascade develops which we model by classical transport theory. Electrons can undergo inelastic scattering events, which lead to secondary electrons, and quasi-elastic scattering events in which phonons are excited, thereby heating the lattice. We give an estimate of the magnitude of electron-phonon coupling based on experiments. Temperature distributions in the target lattice after the electron cascade are derived. Only a part of the stopping

power is effective for heating.

We model subsequent lattice restructuring on a picosecond time scale with a proof-of-principle molecular dynamics (MD) simulation. We find threshold behavior in simulation parameters that correspond to the energy density and the total energy deposited by the ion, in agreement to experiment. Results from the previous step are compared to input parameters of the MD simulation and reasonable agreement is found.

The last step, lattice restructuring, has also been applied to nano-hillock creation by *slow highly charged* ions. Starting from earlier results indicating a molten zone around the ion impact site, we find a threshold in simulation parameters, in qualitative agreement to experiment. Experimental hillock heights are reproduced while widths are a factor two too small, indicating additional mechanisms.

Microscopic models for both processes are given and the influence of remarkable similarities is found. The source of energy (kinetic vs. potential) and the mechanism of primary energy deposition (ionization vs. a complex de-excitation cascade) are different in track and hillock formation, respectively. However, both processes result in low-energy electrons in the conduction band of the target which heat the lattice by electron-phonon coupling. If a threshold quantity (stopping power vs. potential energy) of the projectile is reached, melting and restructuring is observed. We have shown that a sharp threshold behavior can only be due to lattice dynamics, ascribing it to the interplay between heating and cooling of the crystal. A unified model for track and hillock formation has been established which bears the promise of future application to similar processes, e.g. to laser ablation.

Appendices

A Equilibrium charge state

A.1 Introduction

This appendix is devoted to a write-up of the technical issues involved in the application of G. Schiwietz's paper [34] to a Xenon projectile of any given energy in CaF_2 . For further reading on the topic of equilibrium charges as well as shape parameters of charge state distributions and the like, the reader is referred to the references given in [34]. A somewhat older review which introduces the basic theoretical concepts can be found in [113].

The problem is to calculate the equilibrium charge of a particle which moves through a solid at a given energy E_p . The particle loses electrons to the target and also captures electrons from the target, which in total gives rise to an average net charge ("equilibrium charge state") which is later used as the "effective charge", the estimated projectile charge felt in the ionization process by the target electron.

Many quantities (e.g. ionization cross sections and stopping powers) scale with the square of the projectile charge, compare appendix C. Therefore, it is essential to have low uncertainties in the estimated equilibrium charge. Up to now, only experiments can provide the required accuracy because in addition to charge exchange processes, complications arise from multi-electron loss processes, meta-

stable excited states, and Auger and radiative transitions of the highly excited projectile-electron system. In solids, the mean charge state is increased compared to gaseous targets because of the much higher collision frequency: highly excited electrons are stripped off before they can decay to a lower state.

Of course, this balance of electron capture and loss is a stochastic process and leads to a distribution of charge states around the equilibrium charge. An example is depicted in fig. A.1 for a system that is similar to Xe in CaF_2 (I in formvar). From exponential ansatzes for the cross sections of (single) electron capture and loss it can be shown that the distribution function $F(q)$ of the population of charge states around the equilibrium charge is given by a Gaussian $F(q) = (2\pi d^2)^{-\frac{1}{2}} \exp(-(q - q_{\text{mean}})^2/(2d^2))$ [113]. Heuristically, this fit agrees to experiment up to charge states with relative intensities of $\geq 1\%$. The maximum width found at projectile velocities $v_p \approx 1 - 10$ a.u. is roughly given by $d = 0.27Z^{\frac{1}{2}}$ [113]. Asymmetries in $F(q)$ are observed for heavier targets and at lower projectile velocities, where $F(q)$ decreases more slowly for $q > q_{\text{mean}}$ than for the low charge states. This is largely due to the cross sections for multiple electron loss which are small in light targets but very large in heavy targets. The lack of an equivalent multiple capture mechanism leads to the asymmetries. The charge state distribution is not considered in the present work.

The approach taken in [34] is pragmatic. They analyze a large number of experiments in which the charge states of projectiles of varying energies are measured after traversing thin foils of different materials. By a multi-parameter least squares fit, a scaling parameter x is found that minimizes the scatter of q_{mean}/Z , with q_{mean} the equilibrium charge state and Z the nuclear charge of the projectile. The other quantities that enter the fit are the velocity v of the projectile (in atomic units) and

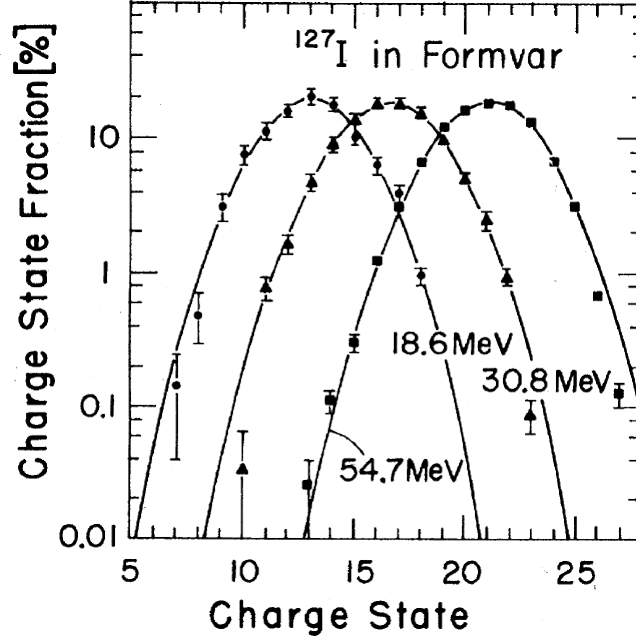


Figure A.1: Equilibrium charge state distributions for iodine ($Z=53$, $m=127$ amu) ions stripped in polymer foils (“formvar”). Ion energies are indicated in the plot and correspond to velocities of 2.4, 3.1 and 4.2 a.u.

the target nuclear charge Z_{target} . For around 850 experimental data points taken from various sources, they find a difference of ± 0.2 between results from different labs, which is a lower bound to the final error. Projectiles from $Z = 1-92$ and targets in the range $Z_{target} = 4-83$ were considered, with about 40% of the experiments using carbon targets. The fit is applied to projectiles with velocities $v \geq 2.8$ only. The result is

$$q_{mean} = Z \frac{12x + x^4}{0.07/x + 6 + 0.3\sqrt{x} + 10.37x + x^4} \quad (A.1)$$

$$x = \left(v Z^{-0.52} Z_{target}^{-0.019Z-0.52v_p} / 1.68 \right)^{1+1.8/Z} \quad (A.2)$$

with uncertainties $\Delta q_{mean} = 0.54$ and relative uncertainty $\Delta q_{mean}/Z = 2.3\%$. Fig. A.2 shows a plot of $[q_{mean}/Z](x)$.

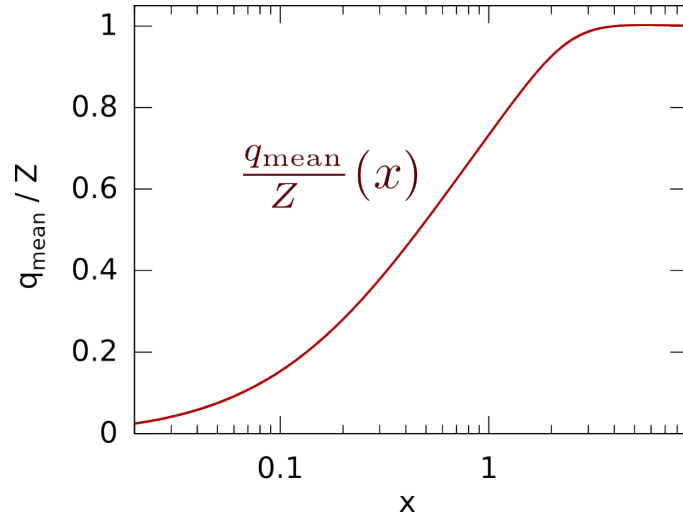


Figure A.2: Plot of q_{mean}/Z as a function of the scaling parameter x (see eq. A.1).

A.2 Application to Xe in CaF₂

The following values have to be inserted in eq. A.1 to model a Xe projectile in CaF₂:

- For a Xe ion ($m_{\text{Xe}} = 131.293 \text{ amu} = 239332.5 \text{ a.u.}$), the velocity v for a projectile energy E_p (in eV) is given by:

$$v = \sqrt{2 E_p / (27.211383 \cdot 239332.5)}$$

- The nuclear charge of Xenon, $Z = 54$.
- The “average target core charge” of CaF₂, $Z_{\text{target}} = 12.6$.

Fig. A.3 shows the part of the stopping power graph above the threshold for track formation and some equilibrium charges as well as other important parameters.

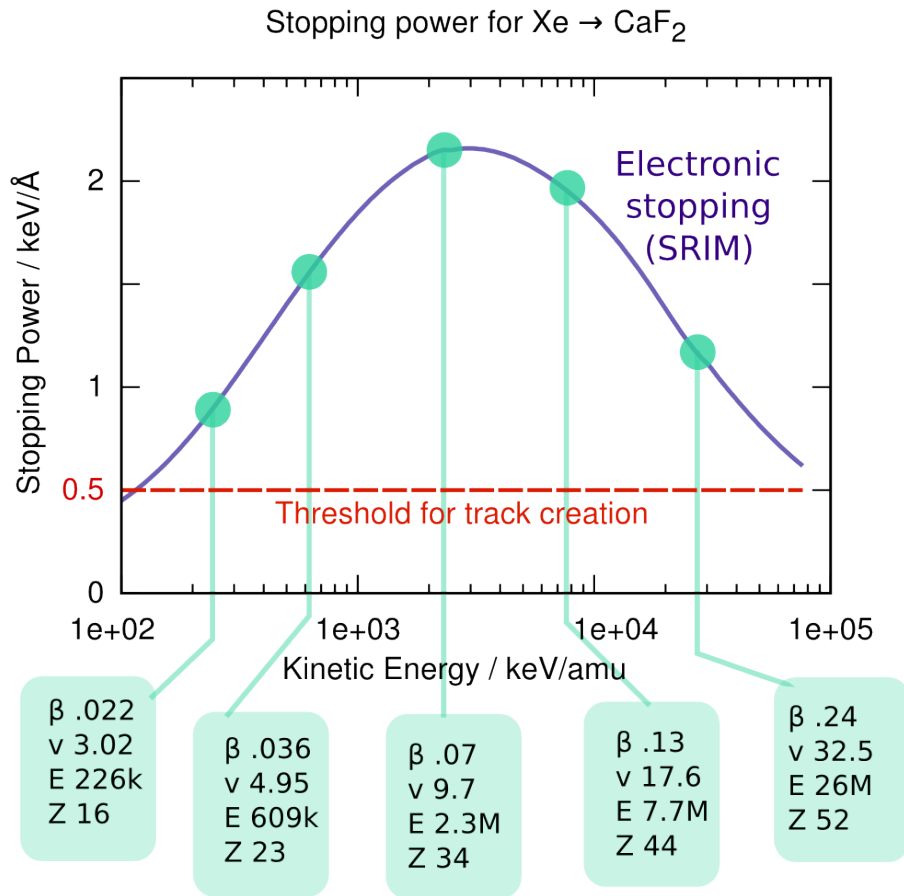


Figure A.3: Electronic stopping power versus projectile energy per atomic mass unit as calculated by SRIM [31] for projectile energies with stopping powers above the threshold for track formation (red line). Below the plot, other quantities derived from the projectile energy are shown: β ($\frac{v}{c}$, $c \dots$ speed of light ≈ 137 a.u.), v (projectile velocity, a.u.), E (projectile energy per mass unit, eV/amu), Z (equilibrium charge).

B Calculation of the wake potential

This appendix is a write-up of the relevant formulae for the calculation of the wake potential (fig. 2.2). As in section 2.3.2.2, we assume that the response of an isotropic dielectric medium is given by its frequency and momentum dependent dielectric function $\varepsilon(q, \omega)$. The (Fourier components of the) total potential $\Phi(q, \omega)$ in response to an external potential $\Phi_0(q, \omega)$ is given by (eq. 2.18)

$$\Phi(q, \omega) = \frac{\Phi_0(q, \omega)}{\varepsilon(q, \omega)} \quad . \quad (\text{B.1})$$

The charge density of the moving projectile (charge Z_p , velocity v_p) is $\rho_0(\vec{r}, t) = Z_p \delta(\vec{r} - \vec{v}_p t)$. We chose cylindrical coordinates in the rest frame of the projectile, $\bar{z} = z - v_p t$, $\rho = \sqrt{x^2 + y^2}$, $R = \sqrt{x^2 + y^2 + \bar{z}^2} = \sqrt{\rho^2 + \bar{z}^2}$. Upon insertion of the Fourier transform of the charge density in the Poisson equation and transforming back to real space, one finds (for particles with mass $\gg 1$) for the total scalar electric potential ϕ in the target [114–116]

$$\begin{aligned} \phi(\rho, \bar{z}) &= \frac{Z_p}{\pi v_p} \int_0^\infty d\kappa \, \kappa J_0(\kappa \rho) \\ &\times \int_{-\infty}^\infty d\omega \, e^{i\omega \bar{z}/v_p} k^{-2} \frac{1}{\varepsilon(k, \omega)} \end{aligned} \quad (\text{B.2})$$

where the wave number is related to the integration variable as $k^2 = \kappa^2 + \frac{\omega^2}{v_p^2}$.

For $\varepsilon(q, \omega)$, we chose the same free electron gas extrapolation as described in eq. 2.21.

The total potential ϕ can be viewed as a superposition of the potentials of the projectile and the wake,

$$\phi(\rho, \bar{z}) = \frac{Z_p}{R} + \phi_{wake} \quad (\text{B.3})$$

and the so-called reduced wake potential is given by $\phi_{wake,red} = \phi_{wake}/Z_p$.

C Time-dependent perturbation theory

In this appendix, we state the main lines of thought which lead to a physical picture of the ionization process in quantum mechanics for a point charge Z_p impinging on an atom with one active electron. For a more detailed calculation, the reader is referred to textbooks of quantum mechanics like [117].

We start by defining the Hamiltonian of the system, neglecting the interaction between the two cores:

$$H(t) = T + V_{target} + V_{projectile} = H_0 + V(t) \quad (\text{C.1})$$

where T is the usual kinetic energy operator, V_{target} the potential of the target, and $V_{projectile}$ the potential of the projectile exerted on the electron. We split the Hamiltonian into a time-independent part H_0 , which is considered to be solved,

$$H_0|\phi\rangle = E_i|\phi\rangle \quad (\text{C.2})$$

with E_i the binding energy (ionization potential) and $|\phi\rangle$ the stationary electronic wave function in the absence of the perturbation caused by the projectile, $V(t)$.

The perturbation should be small in magnitude compared to the interaction in the unperturbed system and/or be of short duration. Intuitively, one could chose the Coulomb potential of the projectile as the perturbation. This choice turns out to be problematic because the criteria for a “perturbation” as stated above are not met in our case. In the results of section 2.2, a part of the *kinetic* energy of the projectile has been chosen as the perturbation, enabling the construction of “unperturbed” states $|\phi\rangle$ that are eigenstates of the combined potentials of target and projectile. To illustrate further the freedom of choice one has, we mention the “distorted wave strong potential Born” approximation, see e.g. [48, 118], in which the potential of the *projectile* is chosen as H_0 and the *target* core as a perturbation. For now, we consider the general case instead of these special ones.

The time evolution operator U of the system is defined by Schrödinger’s equation as

$$i\frac{\partial U(t, t_0)}{\partial t} = H(t)U(t) \ ; \ U(t_0, t_0) = 1 \quad (\text{C.3})$$

and it can be shown that it is possible to expand U into a power series in the perturbation $V(t)$,

$$U(t, t_0) = U_0(t, t_0) + \sum_{n=1}^{+\infty} U_n(t, t_0) \quad (\text{C.4})$$

where U_0 is the evolution of the unperturbed system and U_n is given in terms of the perturbation,

$$\begin{aligned} U_n(t, t_0) &= \frac{(-i)^n}{n!} \int_{t > t_n > \dots > t_0} dt_n dt_{n-1} \dots dt_1 \\ &\times U_0^\dagger(t_n, t_0) V(t_n) U_0(t_n, t_0) \dots U_0^\dagger(t_1, t_0) V(t_1) U_0(t_1, t_0) \ . \end{aligned} \quad (\text{C.5})$$

Rewriting in terms of the overlap between an initial wave function $|\psi_i; t_0\rangle$ and a final wave function $|\psi_f; t\rangle$ at times t_0 and t leads to

$$\begin{aligned} \langle \psi_f; t | \psi_i; t_0 \rangle &= \sum_{n=0}^{\infty} (-i)^n \int_{t \geq t_n \geq \dots \geq t_1 \geq t_0} dt_n \dots dt_1 \\ &\times \langle \psi_f; t | e^{iH_0(t-t_n)} V(t_n) e^{-iH_0(t_n-t_{n-1})} \dots \\ &\dots e^{iH_0(t_2-t_1)} V(t_1) e^{-iH_0(t_1-t_0)} | \psi_i; t_0 \rangle. \end{aligned} \quad (\text{C.6})$$

In a physical picture, this means that in n -th order in perturbation theory the final wave function is reached via n intermediate (virtual) states, where each transition to a virtual state is induced by the perturbation. If we consider orthogonal initial and final stationary states of H_0 , the transition amplitude

$$a_{if} = \langle \psi_f; t | \psi_i; t_0 \rangle = \langle \psi_f | U(t, t_0) | \psi_i \rangle \quad (\text{C.7})$$

will be zero in zeroth order, when the perturbation acts zero times on the wave function. In first order, the initial wave function will be propagated unperturbed from t_0 to t_1 , at which time it “feels” the potential $V(t_1)$. The result will again be propagated from t_1 to t . Projection on $|\psi_f\rangle$ determines the overlap corresponding to the probability amplitude of finding $|\psi_f\rangle$ in a measurement. The sum over all possible times t_1 between t_0 and t gives the total probability amplitude of the process. In second order perturbation theory, we would sum over two points in time t_1 and t_2 at which $V(t)$ acts on the wave function to the right. It is obvious that for short interaction times (high projectile velocities) the major contribution to the total probability should be accessible in first order. However, we cannot expect to model two-step processes in first order, e.g. first electron excitation followed by

emission at a later point in time.

The transition amplitude for a given impact parameter $a_{if}(\vec{b})$ is related to the total transition amplitude a_{if} by

$$a_{if} = \lim_{b_{min} \rightarrow 0, b_{max} \rightarrow \infty} \int_{b_{min}}^{b_{max}} \int_0^{2\pi} b a_{if}(b, \phi) d\phi db \quad , \quad (C.8)$$

giving the total probability for transition from the initial to the final state

$$P_{if} = |a_{if}|^2. \quad (C.9)$$

For the final result, integration limits $t_0 \rightarrow -\infty$ and $t \rightarrow \infty$ are implied, and the final state $|f\rangle$ corresponds to an electron of energy E moving in direction θ from the projectile path (doubly differential cross section). The initial state $|i\rangle$ is the stationary wave function of the bound electron in absence of the perturbation.

Scaling behavior We now show that the probability amplitude scales approximately with Z_p^2 . To do this, we make the following (oversimplified) approximations:

Only terms of order 1 in above series are considered, and the Coulomb potential of the moving ion serves as the perturbation $V(t)$. We take the initial wave function $\phi_i(\vec{r})$ as a hydrogenic wave function. As final state $\phi_f(\vec{r})$, a continuum state of the unperturbed system is chosen, a plane wave of momentum k (energy $E = \frac{k^2}{2}$) in direction θ with respect to the direction of \vec{v}_p . Inserting the explicit form of the straight line of the ion path, and writing the matrix element of V in position space,

we arrive at

$$a_{if}(\vec{b}) = -i \int_{t_0}^t dt' \int d\vec{r} \exp(-i\Delta E t') \phi_f^*(\vec{r}) \frac{Z_p}{|\vec{b} + \vec{v}_p t' - \vec{r}|} \phi_i(\vec{r}) \quad (\text{C.10})$$

with $\Delta E = E + E_i$ the difference between the energies of the initial and final states (binding energy $E_i > 0$). Therefore the transition probability from a bound state to a continuum state, i.e. the doubly differential ionization cross section, scales with Z_p^2 , as does the stopping power. Despite the crudeness of the model, the scaling is verified approximately in experiment [119]. Therefore, a good choice of Z_p is crucial in determining cross sections.

D The fluorite lattice structure

CaF_2 is an ionic crystal with three atoms per primitive face-centered-cubic unit cell in the reduced positions $(0,0,0)$ for Ca and $\pm(\frac{1}{4}, \frac{1}{4}, \frac{1}{4})$ for F. Later, we will assign charges (F^- , Ca^{2+}) to the atoms.

A cubic unit cell which consists of 4 Ca and 8 F atoms is depicted in fig. D.1. It can be seen as a face centered cubic lattice with lattice constant c of Ca atoms and a cubic primitive lattice with lattice constant $\frac{c}{2}$ of F atoms, where the latter is displaced by $\frac{1}{4}$ of the body diagonal in the direction of the body diagonal. The experimental lattice constant is $c = 5.46 \text{ \AA}$ (side length of the cube in D.1). The atomic number densities of Ca, F, and the total atomic number density are therefore (in units \AA^{-3})

$$\begin{aligned} n_{Ca} &= 0.0245744 , \\ n_F &= 0.0491487 , \\ n_{CaF_2} &= 0.0737231 . \end{aligned} \tag{D.1}$$

The experimentally stable face of CaF_2 is the (111) surface. It is terminated by a charge neutral triple layer of F-Ca-F (see below). This means that the structure

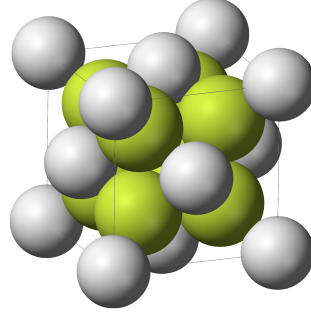


Figure D.1: Cubic unit cell of CaF_2 . Each Ca (white) is coordinated to eight F (yellow-green) while each F is coordinated to four Ca ions. Experimentally, only the (111) surface is stable. The surface normal of the (111) surface corresponds to the body diagonal of the cube in the picture. Picture by Ben Mills.

consists of shifted layers of equilateral triangles of side length $a = \frac{c}{\sqrt{2}}$, half of the face diagonal. The layer distance in the direction perpendicular to the surface (z direction) is $c_z = \frac{c}{4\sqrt{3}}$ as can be seen from the crystal structure: along the space diagonal, there are 3 individual layers of Ca in the cubic unit cell in fig. D.1. The distance between them is one third of the body diagonal, $\frac{c}{\sqrt{3}}$. They are sandwiched by layers of F in a distance of c_z . These triple layers are separated by $4c_z = \frac{c}{\sqrt{3}}$ (see side view of crystal in fig. D.2).

We choose the x axis aligned to the basis of the equilateral triangle, the y axis normal to the x axis in the surface plane and thus aligned to the altitude of the equilateral triangle and the z axis perpendicular to the surface. The individual layers differ only in their starting points in y direction. They are shifted by units $b = \frac{1}{3} \frac{\sqrt{3}a}{2}$ in y direction, i.e. one third of the altitude of the equilateral triangles. Starting from an F atom, the shifts in starting positions when moving through the layers are $+b, +b, -b, +b, +b, -b, \dots$, cf. fig. D.2. The structure repeats exactly after three triple layers, which has been considered in choosing the computational box for the molecular dynamic simulation.

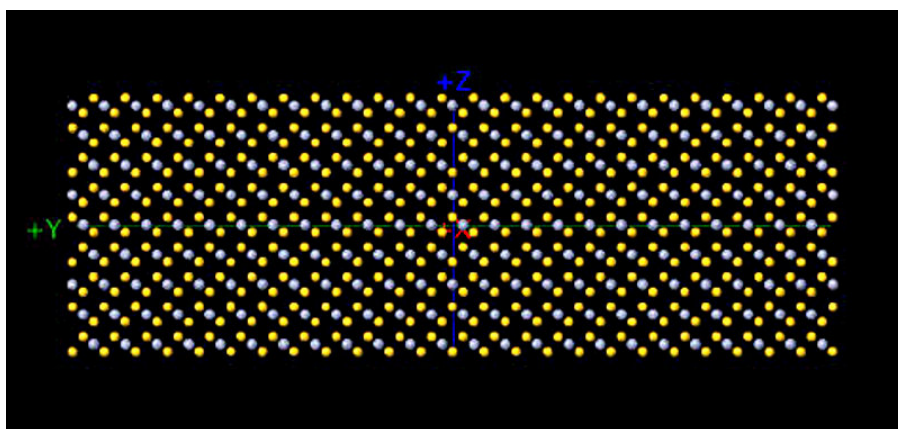


Figure D.2: Side view of a CaF_2 crystal as used in the MD calculations (F yellow, Ca grey, projection along x direction). 22 layers in x , 24 in y , 27 in z direction, giving a system size of about $88 \times 83 \times 28 \text{ \AA}^3$. Note the triple layer structure. This picture was taken from the MD simulation shortly after starting, therefore some atoms whose coordinates coincide with the simulation box borders have already been replaced by their periodic images. Compare text for details.

E Calculation of the pair correlation function

The pair correlation function (or radial distribution function) $g(r)$ [103] is often used as a measure for order in a system. It is directly linked to the structure factor accessible in neutron beam or X-ray scattering experiments. It is given by [120]

$$g(|\vec{r}|) = n_{CaF_2}^{-2} \left\langle \sum_i \sum_{j \neq i} \delta(\vec{r}_i) \delta(\vec{r}_j - \vec{r}) \right\rangle \quad (\text{E.1})$$

with n_{CaF_2} the particle number density and point particles located at r_i . Therefore, it is the conditional probability density to find a particle j in distance $r = |\vec{r}_i - \vec{r}_j|$ from particle i , given that there is a particle at \vec{r}_i . The average is taken over many particles i . For an ideal gas, we would expect $g(r) = \text{const}$ (disorder), while in a crystal, we would expect peaks at all possible linear combinations of the lattice basis vectors.

In this work, the pair correlation function is calculated as follows. A volume within the crystal is selected which is sufficiently far away from the edges. The average is taken over all atoms i within this volume. For each atom i , the number of atoms $j (\neq i)$ within a spherical shell of radius R and thickness ΔR is counted. To obtain a density, this number is divided by the volume of the spherical shell

which is approximately $4\pi R^2 \Delta R$. The pair correlation function $g(r)$ is then given through normalization by the particle number density n .

F Estimate of thermal diffusivity

The thermal diffusivity is a key parameter in the simulation, as it decides how quickly the thermal energy is transported away from the track. The molecular dynamics (MD) simulation contains the information about the thermal diffusivity through the pair potentials. In this appendix, we will briefly discuss how one can estimate its magnitude, and show that our simulation gives realistic results for the thermal diffusivity.

In MD simulations, one often deduces transport coefficients via the Green-Kubo-formalism from equilibrium fluctuations, e.g. [89]. In our case, we proceed differently due to the dynamical nature of the track formation process, where strong non-equilibrium conditions are found. Furthermore, our Berendsen thermostat is not expected to yield reliable values for fluctuations. We therefore solve the heat equation in cylindrical coordinates for initial conditions taken from the MD simulation and an experimental thermal diffusivity and show that our MD simulation yields similar results.

The heat equation in cylindrical coordinates, assuming symmetry in ϕ and z directions ($T(r, \phi, z, t) \rightarrow T(r, t)$), reads

$$\partial_r^2 T(r, t) + \frac{1}{r} \partial_r T(r, t) = k \partial_t T(r, t) \quad (\text{F.1})$$

where $T(r, t)$ is the temperature in distance r from the track axis at the time t after the start of the simulation (or, in the MD calculation, the end of the heating phase). k is the inverse thermal diffusivity which is commonly expressed as $k = \frac{\rho c_p}{\lambda}$ with ρ the mass density, c_p the specific heat capacity, and λ the thermal conductivity of the material. For CaF_2 at room temperature, $\rho \approx 3.18 \text{ g/cm}^3$, $c_p \approx 0.86 \text{ kJ kg}^{-1}\text{K}^{-1}$ and $\lambda \approx 10 \text{ W m}^{-1}\text{K}^{-1}$ [121]. The values are temperature dependent, but for our proof-of-principle estimate, we assume them as constant and note that k should be within a factor of 2 of its true value for $200 \text{ K} \lesssim T \lesssim 1000 \text{ K}$ [121]. The above values give $k = k_0 \approx 2.7 \text{ fs/\AA}^2$.

We integrate the heat equation eq. F.1 using the finite difference method for three different values of k , namely $0.5k_0$, k_0 , and $2k_0$. The initial conditions were taken from the MD simulation after the end of the heating phase, see left panel of figure F.1, for simulation parameters $R_{hot} = 16 \text{ \AA}$ and $T_{hot} = 2000$ (there are no data available for the thermal diffusivity of CaF_2 at very high temperatures). We chose “heat bath” boundary conditions at the maximum r , which in turn was chosen according to the MD simulation box to $r_{max} = 43 \text{ \AA}$. The right panel of fig. F.1 shows a contour plot of the simulation for $k = k_0$. As in our MD simulation, the core of the track cools within some ps.

We chose the temperature of the crystal for $r < R_{hot}$ as a time-dependent parameter which is conveniently extracted from the MD calculation. Fig. F.2 shows the time dependent temperature of the hot zone as calculated in the MD simulation compared to the same quantity resulting from integration of the heat equation eq. F.1 with $k = 0.5k_0$, k_0 , and $2k_0$ respectively. While the functional dependence is not exactly reproduced by the heat equation, the decaying time constant of $T(t)$ is well reproduced by k_0 , and certainly lies within the lower and upper bounds

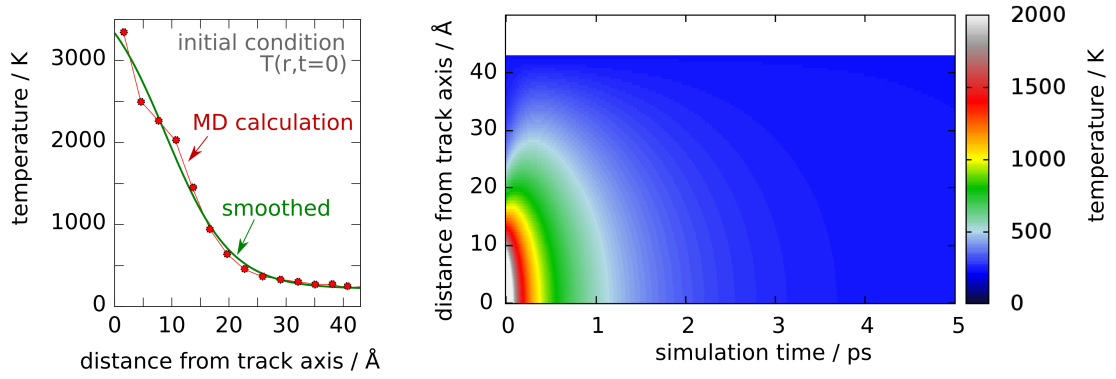


Figure F.1: Left panel: Initial conditions for the heat transport simulation. Red dots: calculated from MD (at the end of the heating phase, $R_{hot} = 16 \text{ \AA}$, $T_{hot} = 2000 \text{ K}$), green line: smoothed fit function used as initial condition for heat transport simulation. Right panel: solution $T(r, t)$ of the heat transport equation eq. F.1 for initial condition from left panel and inverse thermal diffusivity $k = k_0 \approx 2.7 \text{ fs/\AA}^2$.

given by $0.5k_0$ and $2k_0$. We conclude that the order of magnitude of the thermal diffusivity is well reproduced by our MD simulation.

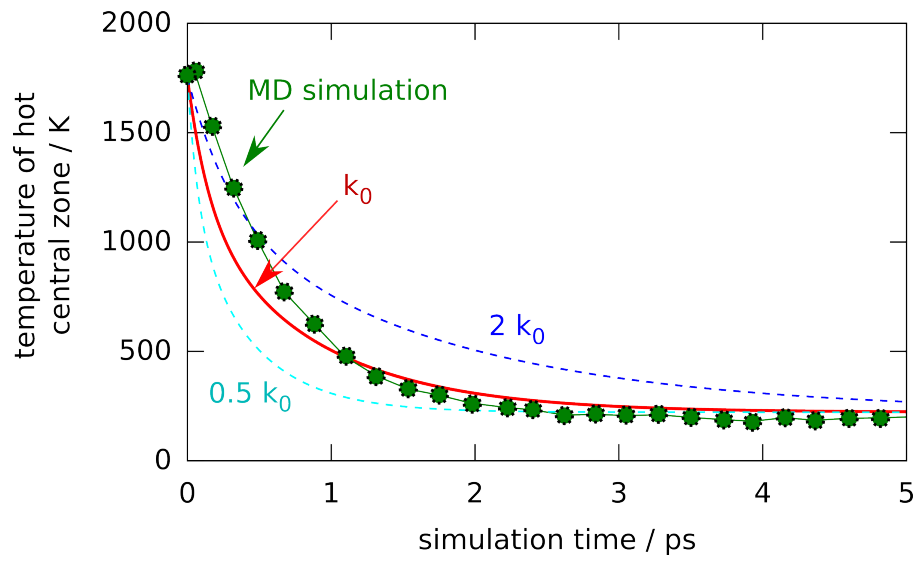


Figure F.2: Time dependent average temperature $T(t)$ of “hot” zone (i.e. $r < R_{hot} = 16 \text{ \AA}$). Green dots: MD calculation, lines: solutions of heat equation for initial condition as in left panel of fig. F.1 with $k = k_0$ (solid red line), $0.5k_0$ (turquoise dashed line) and $2k_0$ (blue dashed line); k_0 is the inverse thermal diffusivity of CaF_2 at room temperature.

Bibliography

- [1] C. Lemell, A. S. El-Said, W. Meissl, I. C. Gebeshuber, C. Trautmann, M. Toulemonde, J. Burgdörfer, and F. Aumayr. *On the nano-hillock formation induced by slow highly charged ions on insulator surfaces*. Solid-State Electronics **51**, 1398 (2007).
- [2] R. L. Fleisher, P. B. Price, and R. M. Walker. *Nuclear tracks in solids: Principles and applications*. Berkeley, Calif., University of California Press, 1975. 626 p. (1975).
- [3] T. Berger, G. Reitz, M. Hajek, and N. Vana. *Comparison of various techniques for the exact determination of absorbed dose in heavy ion fields using passive detectors*. Advances in Space Research **37**, 1716 (2006).
- [4] M. Köhler. *Nanotechnologie*. Wiley-VCH, 2001 (2001).
- [5] L. Hanley and S. B. Sinnott. *The growth and modification of materials via ion-surface processing*. Surface Science **500**, 500 (2002).
- [6] F. Watt, A. A. Bettiol, J. A. V. Kan, E. J. Teo, and M. B. H. Breese. *Ion beam lithography and nanofabrication: a review*. International Journal of Nanoscience **4**, 269 (2005).

-
- [7] N. Stolterfoht, J. H. Bremer, V. Hoffmann, R. Hellhammer, D. Fink, A. Petrov, and B. Sulik. *Transmission of 3 keV Ne^{7+} Ions through Nanocapillaries Etched in Polymer Foils: Evidence for Capillary Guiding*. Physical Review Letters **88**, 133201+ (2002).
- [8] L. Civale, A. D. Marwick, T. K. Worthington, M. A. Kirk, J. R. Thompson, L. K. Elbaum, Y. Sun, J. R. Clem, and F. Holtzberg. *Vortex confinement by columnar defects in $YBa_2Cu_4O_7$ crystals: Enhanced pinning at high fields and temperatures*. Physical Review Letters **67**, 648 (1991).
- [9] Y. Nakajima, Y. Tsuchiya, T. Taen, T. Tamegai, S. Okayasu, and M. Sasase. *Enhancement of critical current density in Co-doped $BaFe_2As_2$ with columnar defects introduced by heavy-ion irradiation*. Physical Review B (Condensed Matter and Materials Physics) **80**, 012510+ (2009).
- [10] P. Sigmund. *Kinetic theory of particle stopping in a medium with internal motion*. Physical Review A **26**, 2497+ (1982).
- [11] E. Dartyge and P. Sigmund. *Tracks of heavy ions in muscovite mica: Analysis of the rate of production of radiation defects*. Physical Review B **32**, 5429+ (1985).
- [12] A. Meftah, F. Brisard, J. M. Costantini, M. Hage-Ali, J. P. Stoquert, F. Studer, and M. Toulemonde. *Swift heavy ions in magnetic insulators: A damage-cross-section velocity effect*. Physical Review B **48**, 920+ (1993).
- [13] A. Meftah, F. Brisard, J. M. Costantini, E. Dooryhee, M. Hage-Ali, M. Hervieu, J. P. Stoquert, F. Studer, and M. Toulemonde. *Track forma-*

- tion in SiO₂ quartz and the thermal-spike mechanism.* Physical Review B **49**, 12457+ (1994).
- [14] H. Dammak, A. Dunlop, D. Lesueur, A. Brunelle, S. Della Negra, and Y. Le Beyec. *Tracks in Metals by MeV Fullerenes.* Physical Review Letters **74**, 1135 (1995).
- [15] L. Chadderton. *Nuclear tracks in solids: registration physics and the compound spike.* Radiation Measurements **36**, 13 (2003).
- [16] I. M. Lifshits, M. I. Kaganov, and L. V. Tanatarov. *On the theory of the changes produced in metals by radiation.* Atomic Energy **6**, 261 (1960).
- [17] I. Lifshits. *On the theory of radiation-induced changes in metals,*. Journal of Nuclear Energy. Part A. Reactor Science **12**, 69 (1960).
- [18] C. Dufour, A. Audouard, F. Beuneu, J. Dural, J. P. Girard, A. Hairie, M. Levalois, E. Paumier, and M. Toulemonde. *A high-resistivity phase induced by swift heavy-ion irradiation of Bi: a probe for thermal spike damage?* Journal of Physics: Condensed Matter **5**, 4573 (1993).
- [19] M. Toulemonde, J. M. Costantini, C. Dufour, A. Meftah, E. Paumier, and F. Studer. *Track creation in SiO₂ and BaFe₁₂O₁₉ by swift heavy ions: a thermal spike description.* Nuclear Instruments and Methods in Physics Research Section B: Beam Interactions with Materials and Atoms **116**, 37 (1996).
- [20] M. Toulemonde. *Transient thermal processes in heavy ion irradiation of crystalline inorganic insulators.* Nuclear Instruments and Methods in Physics Research Section B: Beam Interactions with Materials and Atoms **166-167**, 903 (2000).

-
- [21] Z. G. Wang, C. Dufour, E. Paumier, and M. Toulemonde. *The S_e sensitivity of metals under swift-heavy-ion irradiation: a transient thermal process*. Journal of Physics: Condensed Matter **6**, 6733 (1994).
- [22] C. Dufour, Z. G. Wang, E. Paumier, and M. Toulemonde. *Transient thermal process induced by swift heavy ions: defect annealing and defect creation in Fe and Ni*. Bulletin of Materials Science **22**, 671+ (1999).
- [23] W. Assmann, M. Toulemonde, and C. Trautmann. *Electronic Sputtering with Swift Heavy Ions*. pp. 401–450 (2007).
- [24] H. Walter, W. Prusseit, R. Semerad, H. Kinder, W. Assmann, H. Huber, H. Burkhardt, D. Rainer, and J. A. Sauls. *Low-Temperature Anomaly in the Penetration Depth of $YBa_2Cu_3O_7$ Films: Evidence for Andreev Bound States at Surfaces*. Physical Review Letters **80**, 3598 (1998).
- [25] J. Wiesner. *In-situ-Messungen der Auswirkung kolumnarer Defekte auf die Transportstromeigenschaften von supraleitenden $Bi_2Sr_2CaCu_2O_{8+x}$ -Dünnschichten*. Ph.D. thesis, TH Darmstadt (1994).
- [26] A. S. El-Said, W. Meissl, M. C. Simon, J. R. Crespo lópez Urrutia, C. Lemell, J. Burgdörfer, I. C. Gebeshuber, H. Winter, J. Ullrich, C. Trautmann, M. Toulemonde, and F. Aumayr. *Potential energy threshold for nano-hillock formation by impact of slow highly charged ions on a CaF_2 (1 1 1) surface*. Nuclear Instruments and Methods in Physics Research Section B: Beam Interactions with Materials and Atoms **258**, 167 (2007).
- [27] M. Castro, R. Cuerno, L. Vázquez, and R. Gago. *Self-Organized Ordering of*

- Nanostructures Produced by Ion-Beam Sputtering*. Physical Review Letters **94**, 016102+ (2005).
- [28] S. Facsko, T. Dekorsy, C. Koerdt, C. Trappe, H. Kurz, A. Vogt, and H. L. Hartnagel. *Formation of Ordered Nanoscale Semiconductor Dots by Ion Sputtering*. Science **285**, 1551 (1999).
- [29] A. Arnau. *Interaction of slow multicharged ions with solid surfaces*. Surface Science Reports **27**, 113 (1997).
- [30] C. J. Carlile and B. T. M. Willis. *The pulsed-neutron diffraction method of studying acoustic phonons in barium fluoride and calcium fluoride*. Acta Crystallographica Section A **45**, 708 (1989).
- [31] J. F. Ziegler. *SRIM-2008 software package*. www.srim.org.
- [32] F. C. Fischer, T. Brage, and P. Jönsson. *Computational atomic structure: An MCHF approach*. Taylor & Francis (1997).
- [33] R. D. Cowan. *The Theory of Atomic Structure and Spectra (Los Alamos Series in Basic and Applied Sciences, 3)*. University of California Press (1981).
- [34] G. Schiwietz and P. L. Grande. *Improved charge-state formulas*. Nuclear Instruments and Methods in Physics Research Section B: Beam Interactions with Materials and Atoms **175-177**, 125 (2001).
- [35] J. H. McGuire and L. Weaver. *Independent electron approximation for atomic scattering by heavy particles*. Physical Review A **16**, 41 (1977).
- [36] R. L. Kauffman, J. H. McGuire, P. Richard, and C. F. Moore. *Projectile and*

- Target Dependence of the K-alpha Satellite Structure*. Physical Review A **8**, 1233 (1973).
- [37] M. Horbatsch. *Calculation of transfer ionisation processes in ion-atom collisions*. Journal of Physics B: Atomic and Molecular Physics **19**, L193 (1986).
- [38] M. Horbatsch. *Independent particle model description of multiple ionization dynamics in fast ion-atom collisions*. Journal of Physics B: Atomic, Molecular and Optical Physics **25**, 3797 (1992).
- [39] A. Müller, B. Schuch, W. Groh, E. Salzborn, H. F. Beyer, P. H. Mokler, and R. E. Olson. *Multiple-electron capture and ionization in collisions of highly stripped ions with Ar atoms*. Physical Review A **33**, 3010 (1986).
- [40] B. Gervais. *Etude du dépôt d'énergie des ions lourds rapides dans les solides par simulation Monte-Carlo*. Ph.D. thesis, Université de Caen (1993).
- [41] A. S. Schlachter, K. H. Berkner, W. G. Graham, R. V. Pyle, P. J. Schneider, K. R. Stalder, J. W. Stearns, J. A. Tanis, and R. E. Olson. *Ionization of rare-gas targets by collisions of fast highly charged projectiles*. Physical Review A **23**, 2331 (1981).
- [42] P. D. Fainstein, L. Gulyas, and A. Salin. *Impact-parameter dependence of the ionization probability in the CDW-EIS approximation*. Journal of Physics B: Atomic, Molecular and Optical Physics **29**, 1225 (1996).
- [43] M. Verstraete and X. Gonze. *First-principles calculation of the electronic, dielectric, and dynamical properties of CaF₂*. Physical Review B **68**, 195123+ (2003).

-
- [44] R. A. Heaton and C. C. Lin. *Electronic energy-band structure of the calcium fluoride crystal*. Physical Review B **22**, 3629+ (1980).
- [45] R. T. Poole, J. Szajman, R. C. G. Leckey, J. G. Jenkin, and J. Liesegang. *Electronic structure of the alkaline-earth fluorides studied by photoelectron spectroscopy*. Physical Review B **12**, 5872+ (1975).
- [46] M. R. C. McDowell and J. P. Coleman. *Introduction to the Theory of Ion-Atom Collisions*. Elsevier Science Publishing Co Inc., U.S. (1970).
- [47] P. D. Fainstein. *Longitudinal electron momentum distributions in single ionization of helium by light projectiles*. Journal of Physics B: Atomic, Molecular and Optical Physics **29**, L763 (1996).
- [48] D. R. Schultz and C. O. Reinhold. *Theoretical description of the ejected-electron spectrum in collisions of 1.5-MeV/u F^{9+} with helium*. Physical Review A **50**, 2390 (1994).
- [49] D. Belkic. *A quantum theory of ionisation in fast collisions between ions and atomic systems*. Journal of Physics B: Atomic and Molecular Physics **11**, 3529 (1978).
- [50] I. M. Cheshire. *Continuum distorted wave approximation; resonant charge transfer by fast protons in atomic hydrogen*. Proceedings of the Physical Society **84**, 89 (1964).
- [51] D. S. F. Crothers and J. F. Mccann. *Ionisation of atoms by ion impact*. Journal of Physics B: Atomic and Molecular Physics **16**, 3229 (1983).
- [52] P. D. Fainstein, V. H. Ponce, and R. D. Rivarola. *Two-centre effects in*

- ionization by ion impact*. Journal of Physics B: Atomic, Molecular and Optical Physics **24**, 3091 (1991).
- [53] N. Stolterfoht, D. Schneider, J. Tanis, H. Altevogt, A. Salin, P. D. Fainstein, R. Rivarola, J. P. Grandin, J. N. Scheurer, S. Andriamonje, D. Bertault, and J. F. Chemin. *Evidence for Two-Centre Effects in the Electron Emission from 25 MeV/u Mo^{40+} + He Collisions: Theory and Experiment*. EPL (Europhysics Letters) **4**, 899 (1987).
- [54] D. S. F. Crothers. *Refined orthogonal variational treatment of continuum distorted waves*. Journal of Physics B: Atomic and Molecular Physics **15**, 2061 (1982).
- [55] E. Clementi and C. Roetti. *Roothaan-Hartree-Fock atomic wavefunctions Basis functions and their coefficients for ground and certain excited states of neutral and ionized atoms, Z lower or equal 54*. Atomic Data and Nuclear Data Tables **14**, 177 (1974).
- [56] C. Bunge. *Roothaan-Hartree-Fock Ground-State Atomic Wave Functions: Slater-Type Orbital Expansions and Expectation Values for $Z = 2-54$* . Atomic Data and Nuclear Data Tables **53**, 113 (1993).
- [57] C. F. Bunge, J. A. Barrientos, A. V. Bunge, and J. A. Cogordan. *Hartree-Fock and Roothaan-Hartree-Fock energies for the ground states of He through Xe*. Physical Review A **46**, 3691+ (1992).
- [58] T. Koga, H. Tatewaki, and A. J. Thakkar. *Roothaan-Hartree-Fock wave functions for atoms with Z 1-54*. Physical Review A **47**, 4510+ (1993).

-
- [59] T. Koga, S. Watanabe, K. Kanayama, R. Yasuda, and A. J. Thakkar. *Improved Roothaan–Hartree–Fock wave functions for atoms and ions with $N \leq 54$* . The Journal of Chemical Physics **103**, 3000 (1995).
- [60] D. Mcsherry. *Ion-Atom/Argon-Calculation of ionization cross sections by fast ion impact for neutral target atoms ranging from hydrogen to argon*. Computer Physics Communications **155**, 144 (2003).
- [61] I. D. Kaganovich, E. Startsev, and R. C. Davidson. *Scaling and formulary of cross-sections for ion-atom impact ionization*. New Journal of Physics **8**, 278 (2006).
- [62] D. Pines, P. Nozieres, and P. Nozieres. *Theory of Quantum Liquids (Advanced Book Classics)*. Westview Press (1999).
- [63] K. Schiessl, K. Tőkési, B. Solleder, C. Lemell, and J. Burgdörfer. *Electron Guiding through Insulating Nanocapillaries*. Physical Review Letters **102**, 163201+ (2009).
- [64] M. M. Elcombe and A. W. Pryor. *The lattice dynamics of calcium fluoride*. Journal of Physics C: Solid State Physics **3**, 492 (1970).
- [65] E. D. Palik. *Handbook of optical constants of solids II*. Academic Press (1991).
- [66] Z.-J. Ding. *Fundamental Studies on the Interactions of kV Electrons with Solids for Applications to Electron Spectroscopies*. Ph.D. thesis, Department of Applied Physics, Osaka University, Japan (1990).
- [67] B. Solleder, C. Lemell, K. Tőkési, N. Hatcher, and J. Burgdörfer. *Spin-dependent low-energy electron transport in metals*. Physical Review B (Condensed Matter and Materials Physics) **76**, 075115+ (2007).

-
- [68] F. Salvat, A. Jablonski, and C. J. Powell. *ELSEPA—Dirac partial-wave calculation of elastic scattering of electrons and positrons by atoms, positive ions and molecules*. Computer Physics Communications **165**, 157 (2005).
- [69] G. G. Fuentes, E. B. Palen, T. Pichler, X. Liu, A. Graff, G. Behr, R. J. Kalenczuk, M. Knupfer, and J. Fink. *Electronic structure of multiwall boron nitride nanotubes*. Physical Review B **67**, 035429+ (2003).
- [70] M. Knupfer, T. Pichler, M. S. Golden, J. Fink, M. Murgia, R. H. Michel, R. Zamboni, and C. Taliani. *Size of Electron-Hole Pairs in Pi-Conjugated Systems*. Physical Review Letters **83**, 1443 (1999).
- [71] K. Yang, L. P. Chen, Y. Q. Cai, N. Hiraoka, S. Li, J. F. Zhao, D. W. Shen, H. F. Song, H. Tian, L. H. Bai, Z. H. Chen, Z. G. Shuai, and D. L. Feng. *Inelastic X-Ray Scattering Study of Exciton Properties in an Organic Molecular Crystal*. Physical Review Letters **98**, 036404+ (2007).
- [72] V. Olevano, L. Reining, and F. Sottile. *DP - a Linear Response TDDFT code, in Frequency-Reciprocal and Frequency-Real space, on a Plane Waves basis set*. dp-code.org (1997-present).
- [73] A. G. Marinopoulos, L. Reining, A. Rubio, and V. Olevano. *Ab initio study of the optical absorption and wave-vector-dependent dielectric response of graphite*. Physical Review B **69**, 245419+ (2004).
- [74] B. Henke. *X-Ray Interactions: Photoabsorption, Scattering, Transmission, and Reflection at $E = 50\text{-}30,000$ eV, $Z = 1\text{-}92$* . Atomic Data and Nuclear Data Tables **54**, 181 (1993).

-
- [75] K. Tkesi, X. Tong, C. Lemell, and J. Burgdorfer. *Friction Force for Charged Particles at Large Distances from Metal Surfaces*, volume 46 of *Advances in Quantum Chemistry*, pp. 29–64 (2004).
- [76] K. Tokési, X. M. Tong, C. Lemell, and J. Burgdörfer. *Energy loss of charged particles at large distances from metal surfaces*. *Phys. Rev. A* **72**, 022901+ (2005).
- [77] J. Barth, R. L. Johnson, M. Cardona, D. Fuchs, and A. M. Bradshaw. *Dielectric function of CaF_2 between 10 and 35 eV*. *Physical Review B* **41**, 3291+ (1990).
- [78] H. Seiler. *Secondary electron emission in the scanning electron microscope*. *Journal of Applied Physics* **54**, R1 (1983).
- [79] G. Grochtmann, R. J. Meyer, F. Peters, and L. Gmelin. *Gmelins Handbuch der anorganischen Chemie*. Verlag Chemie, Berlin (1970).
- [80] P. S. Krstic, C. O. Reinhold, and S. J. Stuart. *Chemical sputtering from amorphous carbon under bombardment by deuterium atoms and molecules*. *New Journal of Physics* **9**, 209 (2007).
- [81] C. Reinhold, P. Krstic, and S. Stuart. *Time scales of chemical sputtering of carbon*. *Nuclear Instruments and Methods in Physics Research Section B: Beam Interactions with Materials and Atoms* **258**, 274 (2007).
- [82] R. Smith, D. E. Harrison, and B. J. Garrison. *keV particle bombardment of semiconductors: A molecular-dynamics simulation*. *Physical Review B* **40**, 93+ (1989).

-
- [83] Z. Postawa, B. Czerwinski, M. Szewczyk, E. J. Smiley, N. Winograd, and B. J. Garrison. *Enhancement of Sputtering Yields Due to C_{60} versus Ga Bombardment of Ag111 As Explored by Molecular Dynamics Simulations*. Analytical Chemistry **75**, 4402 (2003).
- [84] G. Betz and W. Husinsky. *Molecular dynamics studies of cluster emission in sputtering*. Nuclear Instruments and Methods in Physics Research Section B: Beam Interactions with Materials and Atoms **102**, 281+ (1995).
- [85] G. Betz and W. Husinsky. *Cluster bombardment of solids: A molecular dynamics study*. Nuclear Instruments and Methods in Physics Research Section B: Beam Interactions with Materials and Atoms **122**, 311+ (1997).
- [86] P. Lorazo, L. J. Lewis, and M. Meunier. *Short-Pulse Laser Ablation of Solids: From Phase Explosion to Fragmentation*. Physical Review Letters **91**, 225502+ (2003).
- [87] P. J. D. Lindan and M. J. Gillan. *Shell-model molecular dynamics simulation of superionic conduction in CaF_2* . Journal of Physics: Condensed Matter **5**, 1019 (1993).
- [88] X. Sun, Y. Chu, Z. Liu, Q. Chen, Q. Song, and T. Song. *Simulated equation of state of CaF_2 with fluorite-type structure at high temperature and high pressure*. Physica B: Condensed Matter **404**, 158 (2009).
- [89] P. J. D. Lindan and M. J. Gillan. *A molecular dynamics study of the thermal conductivity of CaF_2 and UO_2* . Journal of Physics: Condensed Matter **3**, 3929 (1991).

-
- [90] D. Bingham, A. N. Cormack, and C. R. A. Catlow. *Rigid-ion potentials for SrF_2 , CaF_2 and GdF_3* . Journal of Physics: Condensed Matter **1**, 1205 (1989).
- [91] E. Flenner, J. Das, M. C. Rheinstädter, and I. Kosztin. *Subdiffusion and lateral diffusion coefficient of lipid atoms and molecules in phospholipid bilayers*. Physical Review E (Statistical, Nonlinear, and Soft Matter Physics) **79**, 011907+ (2009).
- [92] X. Yu, Q. Wang, J.-C. Yang, I. Buch, C.-J. Tsai, B. Ma, S. Z. D. Cheng, R. Nussinov, and J. Zheng. *Mutational Analysis and Allosteric Effects in the HIV-1 Capsid Protein Carboxyl-Terminal Dimerization Domain*. Biomacromolecules **10**, 390 (2009).
- [93] O.-S. Lee and G. C. Schatz. *Molecular Dynamics Simulation of DNA-Functionalized Gold Nanoparticles*. The Journal of Physical Chemistry C **113**, 2316 (2009).
- [94] D. T. Jones, W. R. Taylor, and J. M. Thornton. *A new approach to protein fold recognition*. Nature **358**, 86 (1992).
- [95] D. W. Brenner, O. A. Shenderova, J. A. Harrison, S. J. Stuart, B. Ni, and S. B. Sinnott. *A second-generation reactive empirical bond order (REBO) potential energy expression for hydrocarbons*. Journal of Physics: Condensed Matter **14**, 783 (2002).
- [96] B. Zagrovic, C. D. Snow, M. R. Shirts, and V. S. Pande. *Simulation of Folding of a Small Alpha-helical Protein in Atomistic Detail using Worldwide-distributed Computing*. Journal of Molecular Biology **323**, 927 (2002).

-
- [97] J. A. Anderson, C. D. Lorenz, and A. Travesset. *HOOMD (Highly Optimized Object-oriented Molecular Dynamics)*. <http://www.ameslab.gov/hoomd/about.html>.
- [98] J. Anderson, C. Lorenz, and A. Travesset. *General purpose molecular dynamics simulations fully implemented on graphics processing units*. Journal of Computational Physics **227**, 5342 (2008).
- [99] Nvidia. *Nvidia CUDA collection*. http://www.nvidia.com/object/cuda_home.html.
- [100] L. Verlet. *Computer "Experiments" on Classical Fluids. I. Thermodynamical Properties of Lennard-Jones Molecules*. Physical Review Online Archive (Prola) **159**, 98+ (1967).
- [101] R. Smith and D. E. Harrison. *Algorithms for molecular dynamics simulations of keV particle bombardment*. Computers in Physics **3**, 68 (1989).
- [102] P. J. Mitchell and D. Fincham. *Shell model simulations by adiabatic dynamics*. Journal of Physics: Condensed Matter **5**, 1031 (1993).
- [103] M. Griebel, S. Knapek, and G. Zumbusch. *Numerical Simulation in Molecular Dynamics: Numerics, Algorithms, Parallelization, Applications (Texts in Computational Science and Engineering)*. Springer (2007).
- [104] H. J. C. Berendsen, J. P. M. Postma, W. F. van Gunsteren, A. Dinola, and J. R. Haak. *Molecular dynamics with coupling to an external bath*. The Journal of Chemical Physics **81**, 3684 (1984).
- [105] J. Jensen, A. Dunlop, and S. Dellanegra. *Tracks induced in CaF₂ by MeV*

- cluster irradiation*. Nuclear Instruments and Methods in Physics Research Section B: Beam Interactions with Materials and Atoms **141**, 753 (1998).
- [106] J. Jensen. *Microscopic observations of metallic inclusions generated along the path of MeV clusters in CaF_2* . Nuclear Instruments and Methods in Physics Research Section B: Beam Interactions with Materials and Atoms **146**, 399 (1998).
- [107] B. R. Schroeder, S. Meng, A. Bostwick, M. A. Olmstead, and E. Rotenberg. *Epitaxial growth of laminar crystalline silicon on CaF_2* . Applied Physics Letters **77**, 1289 (2000).
- [108] A. S. E. Said, R. Heller, W. Meissl, R. Ritter, S. Facsko, C. Lemell, B. Solleder, I. C. Gebeshuber, G. Betz, M. Toulemonde, W. Möller, J. Burgdörfer, and F. Aumayr. *Creation of Nanohillocks on CaF_2 Surfaces by Single Slow Highly Charged Ions*. Physical Review Letters **100**, 237601+ (2008).
- [109] N. Khalfaoui, M. Gorlich, C. Muller, M. Schleberger, and H. Lebius. *Latent tracks in CaF_2 studied with atomic force microscopy in air and in vacuum*. Nuclear Instruments and Methods in Physics Research Section B: Beam Interactions with Materials and Atoms **245**, 246 (2006).
- [110] J. Burgdörfer, P. Lerner, and F. W. Meyer. *Above-surface neutralization of highly charged ions: The classical over-the-barrier model*. Physical Review A **44**, 5674 (1991).
- [111] J. Burgdorfer, C. Reinhold, and F. Meyer. *Fast neutralization of highly charged ions in grazing incidence collisions with surfaces*. Nuclear Instru-

- ments and Methods in Physics Research Section B: Beam Interactions with Materials and Atoms **98**, 415 (1995).
- [112] L. Wirtz, C. O. Reinhold, C. Lemell, and J. Burgdörfer. *Liouville master equation for multielectron dynamics: Neutralization of highly charged ions near a LiF surface*. Physical Review A **67**, 012903+ (2003).
- [113] H. D. Betz. *Charge States and Charge-Changing Cross Sections of Fast Heavy Ions Penetrating Through Gaseous and Solid Media*. Reviews of Modern Physics **44**, 465 (1972).
- [114] P. M. Echenique, R. H. Ritchie, and W. Brandt. *Spatial excitation patterns induced by swift ions in condensed matter*. Physical Review B **20**, 2567+ (1979).
- [115] R. H. Ritchie, W. Brandt, and P. M. Echenique. *Wake potential of swift ions in solids*. Physical Review B **14**, 4808+ (1976).
- [116] J. Neufeld and R. H. Ritchie. *Passage of Charged Particles through Plasma*. Physical Review **98**, 1632+ (1955).
- [117] A. Messiah. *Quantum Mechanics*. Dover Publications (1999).
- [118] M. Brauner and J. H. Macek. *Ion-impact ionization of He targets*. Physical Review A **46**, 2519 (1992).
- [119] P. D. Fainstein, V. H. Ponce, and R. D. Rivarola. *Z_P^3 effects in the ionization of helium by ion impact*. Physical Review A **36**, 3639 (1987).

-
- [120] B.-J. Lin and L.-J. Chen. *Phase transitions in two-dimensional colloidal particle system observed in Langmuir trough*. Colloids and Surfaces A: Physico-chemical and Engineering Aspects **284-285**, 239 (2006).
- [121] S. Andersson and G. Backstrom. *Thermal conductivity and heat capacity of single-crystal LiF and CaF₂ under hydrostatic pressure*. Journal of Physics C: Solid State Physics **20**, 5951 (1987).

Acknowledgements

The author would like to express his gratitude to the people involved in the production of this work.

C. Lemell for advising the author and his inspiring suggestions.

J. Burgdörfer for illuminating discussions throughout the development of this work.

G. Betz for introducing the author to his molecular dynamics code.

K. Schiessl for introducing the author to the electron transport code.

K. Tórkési for fruitful discussions on CTMC and CDW-EIS and for the invitation to ATOMKI, Debrecen, where good progress was made in setting up the model for track formation.

F. Aumayr, in whose group the experiments on nano-hillock formation are done, for enlightenment on the experimental side of hillock formation.

Furthermore, he is to thank for organizing the author's trip to the 4th ITS LEIF Annual Meeting and 2nd Symposium on Ion-Insulator Interactions in Girona. Funding by the ITS LEIF network can thus be acknowledged. The

conference provided insights into current developments and experimental techniques which were important for this work.

J. Feist *et al.* for providing the author with the L^AT_EX skeleton this work uses.

F. Libisch for setting up and maintaining the Subversion repository.

P. Tiwald for general problem solving and lossless oscillation of knowledge.

The members of the work group at ITP for inspiration and chocolate.

Family and friends for their support.